REPORT DOCUMENTATION PAGE

AFRL-SR-AR-TR-03-

0426

1. AGENCY USE ONLY (Leave blank)	2. REPORT DATE	3. REPORT TYPE AND DATES COVERED
	10/30/03	Final, 05/01/00 - 06/30/03

4. TITLE AND SUBTITLE
MULTI-FUNCTIONAL MATERIALS FOR THERMAL CONTROL OF SENSORS AND ELECTRONICS

5. FUNDING NUMBERS
F49620 00 1 0305

6. AUTHOR(S)
R.A. Wirtz
Y. Jiang
A. Fuchs

7. PERFORMING ORGANIZATION NAME(S) AND ADDRESS(ES)
University of Nevada, Reno
Ross Hall, Rm204/MS325
Reno, NV 89557

8. PERFORMING ORGANIZATION REPORT NUMBER
1330-117-30At

9. SPONSORING / MONITORING AGENCY NAME(S) AND ADDRESS(ES)
Dr. Thomas Beutner
AFOSR/NA
4015 Wilson Blvd, Rm 713
Arlington, VA 22203-1954

10. SPONSORING / MONITORING AGENCY REPORT NUMBER

11. SUPPLEMENTARY NOTES

12a. DISTRIBUTION / AVAILABILITY STATEMENT

12b. DISTRIBUTION CODE

13. ABSTRACT *(Maximum 200 Words)*

Research focuses on development of Thermal Energy Storage (TES) sandwich-structures that combine the heat storage function with structural functionality. Heat storage is via the latent heat of a component of the composite structure. The principal application is thermal control of variable-power avionics systems such as intermittently operated radar. The primary advantage of this approach is that such multi-functionality results in a smaller, less massive thermal control/structural system. In addition, the TES component of the system can be designed so that its thermal performance is g-load/orientation insensitive.

DISTRIBUTION STATEMENT A
Approved for Public Release
Distribution Unlimited

14. SUBJECT TERMS

15. NUMBER OF PAGES
106

16. PRICE CODE

17. SECURITY CLASSIFICATION OF REPORT	18. SECURITY CLASSIFICATION OF THIS PAGE	19. SECURITY CLASSIFICATION OF ABSTRACT	20. LIMITATION OF ABSTRACT
Unclassified	Unclassified	Unclassified	

MULTI-FUNCTIONAL MATERIALS FOR THERMAL CONTROL OF SENSORS AND ELECTRONICS

F49620-00-1-305

Richard Wirtz, Alan Fuchs and Yanyao Jiang

University of Nevada, Reno

Reno, NV 89557

(775) 784-6714

September 12, 2003

Executive Summary

A Thermal Energy Storage (TES) capability incorporated into the temperature control system of an electronics module having a variable heat dissipation rate will improve system reliability and allow for a smaller, less-power-consuming module cooler that is sized for some intermediate heat load. However, space limitations often preclude the incorporation of this technology into electronics thermal control systems so that TES-systems must be such that they add no mass (or volume) to existing systems. Research focuses on development of multi-functional TES plate-like structures that combine the heat storage function with structural functionality. Heat storage is via the latent heat of a component of the composite structure. Light-weight system configurations ranging from simple plate-laminations to sandwiches containing structurally complex box and lattice sub-structures are considered. Designs whose thermal performance are g-load/orientation insensitive are focused on.

Two material formulations are considered:

A. Metal/PCM Composites: Structural/thermally conductive elements are typically an aluminum micro-extrusion. The TES-volume is a PCM, which may include a thermal conductivity enhancer or other property modifier.

B. Graphite/PCM Composites: Structural elements are a graphite fabric/epoxy matrix composite. The TES-volume is PCM impregnated porous graphite open-cell foam having a typical cell size of 500 μm.

TES-System Thermal Response Simple semi-empirical models that predict the thermal response of plate-like TES-structures have been developed. The models include the three essential features of such devices: 1) the thermal interface to the heat source/sink of the electronics (TI); 2) a heat spreading component such as a conductive plate or foam, that addresses the generally poor thermal conductivity of most phase change materials; and, 3) the thermal storage volume, which includes the PCM plus ancillary materials such as a conductivity enhancer or liquid immobilizer. In addition to the latent heat component of such a system, the models capture specific design attributes such as detail component dimensions, component masses and inter-component interfacial thermal resistances. The models do not require recourse to FE/FD application packages.

A variety of TES-system configurations have been considered, ranging from simple laminations to fairly complex systems that include additional elements for improved structural performance (2D box and Lattice sub-structures). Two design philosophies have been addressed: 1) mm-scale

metallic structures that encapsulate the PCM and ancillaries, and 2) carbon composite structures that encapsulate PCM impregnated graphite foam, which serves to promote heat transfer and immobilize liquid-phase PCM. In addition, two approaches to thermal interfacing the TES-system to the electronics have been considered: a) a matrix of point inputs that results in radial heat flow to/from the TES-volume, and b) line inputs that result in rectilinear heat flow.

Experiments with graphite-epoxy/paraffin impregnated graphite foam prototypes are used to assess the thermal performance models and effectiveness of the various design approaches. The models are found to capture essential characteristics of the transient response of the systems considered. One finding of particular significance is that the effective specific surface area of the graphite foam used in the benchmark experiments is approximately 3-fold smaller than originally anticipated. This leads to an approximate 3-fold increase in the ultimate temperature excursion of the system TI, so the effective specific surface area of the foam component, together with the associated foam-to-paraffin-particle contact conductance are important design attributes for effective thermal control with these non-metallic systems. Furthermore, the thin high-conductivity graphite-epoxy encapsulation does not effectively participate in the heat storage process, so more conventional non-metallic structural elements could be considered without any significant degradation in thermal performance.

A design study of alternative micro-channel aluminum plate/paraffin TES-structures finds that from a thermal perspective; simple laminations, and more complex 2D Box and Lattice substructures give essentially equivalent thermal performance. Furthermore, aluminum based systems appear to give thermal response performance that is a least equivalent to the more complex graphite foam systems.

TES-System Structural Response Mechanical performance of the TES-systems was investigated experimentally and characterized with theoretical models. Experiments were conducted with graphitic TES composites, aluminum channel structures, screen laminate composites, as well as the materials used in the structures. Basic material properties were obtained by testing the materials under tension and compression loading. The structures were tested under bending. Fatigue experiments were conducted for graphitic TES composites at both room and high temperature. The graphite/epoxy skin displays elastic deformation before fracture. Failure occurs in the interface of the graphitic skins and the porous graphitic core. The porous graphitic core and the PCM fill have an insignificant influence on the strength and stiffness of the graphitic TES composites. Temperature greatly affects the fatigue strength of the graphitic TES composites. The copper screen material was found to display tension-compression asymmetry.

The strength of the copper screen laminate composites is dependent on the orientation of the laminates. Failure is due to excessive plastic deformation of the material. The aluminum structures were found to possess excellent strength and stiffness. Failure of the aluminum structures is due to plastic deformation of the material.

An energy method was developed to predict the mechanical behavior of a structure under bending. The method was based on the energy conservation law and can be applied to structures as simple as screen laminates and to structures as complicated as 2D box structures. In addition, finite element models were developed to simulate the deformation and failure of the carbon/graphite TES composites and the screen laminate composites. Both the energy method and the finite element models can provide accurate deformation and failure predictions for the structures under investigation. The method is simple and practical for structures under bending loading. The finite element models are suitable for complex structures under the general loading conditions.

A multiscale methodology was developed for the modeling for the screen laminates. With the model of single layer copper screen, basic mechanical properties of copper screen can be predicted, and the predicted properties can be used as the input to the screen laminate model to simulate the performance of the screen laminates. With the multiscale methodology the sophisticate geometry of copper screen can be studied and the experimental work to obtain the mechanical properties of a single layer copper screen can be saved.

In addition, key aspects of PCM performance are addressed

1. **Distributed Bellows Mechanism** The feasibility of incorporating polymer micro-balloons in paraffin as a distributed bellows mechanism to address the volume expansion that accompanies phase transition is studied. Balloons are found to be adequately durable when exposed to cyclic pressure loading (200 cycles) that simulates expansion and contraction of a contained paraffin mass. Furthermore, pressure loading of approximately 17 atm is sufficient to accommodate phase transition associated expansion of paraffin. From a structural perspective, this is relatively minor loading condition. However, polymer micro-balloons have a specific gravity of approximately 0.2, which makes them quite buoyant in liquid paraffin in a 1g environment. Lacking a suitable balloon immobilization mechanism, this would restrict this approach to zero-g environments.

2. **Paraffin Immobilization** Immobilization of the liquid phase of solid-liquid PCM may be necessary so that TES-system thermal performance is g-load/orientation insensitive. Imbedding the PCM in a foam that has a small cell size (< 500 μm) will lead to short-time immobilization of the liquid because the natural convection Rayleigh number is so small. In situations where the paraffin is contained in a meso-scale encapsulation, embedding paraffin in a suitable thermoplastic matrix could be a desirable design alternative. Gravimetric testing at elevated temperatures, coupled with thermal cyclic testing of a series of co-polymers shows that the co-polymer SEEPS is the most effective immobilizer.

3. **Polyalcohol Solid Solution Formulation** The polyalcohol combination Pentaglycerine/ Neopentaglycol (PG/NPG) is an attractive PCM for electronics thermal control because: 1) It can be formulated to undergo solid-state phase transition over the 24°C - 85°C temperature interval, and 2) the latent heat is competitive with other popular PCM's. However, formulation of solid solutions has been a cumbersome operation. DSC measurements confirm that forming an aqueous solution of the desired mole-fraction followed by drying results in acceptable solid solutions.

Contents

1. Introduction

A Thermal Energy Storage (TES) capability incorporated into the temperature control system of an electronics module having a variable heat dissipation rate will improve system reliability and allow for a smaller, less-power-consuming module cooler that is sized for some intermediate heat load. Then, heat is stored in the TES-system during periods of high power operation, and it is subsequently released from the system during periods of reduced power operation. Materials formulated to undergo phase transition at key temperatures (Phase Change Materials, PCM's) can provide this load-leveling capability via the latent heat effect.

Space limitations often preclude the incorporation of this technology into electronics thermal control systems so that TES-systems must be such that they add no mass (or volume) to existing systems. TES-systems having *multiple functionality* can satisfy this constraint. For example, TES-composites that combine the heat storage function with a structural function can be configured into a system as structural elements while at the same time they are part of the temperature control system. A system that possesses dual functionality, such as thermal storage together with structural functionality, will save weight and space in an avionics system.

The principal application is thermal control of variable-power electronics systems such as intermittently operated radar. The primary advantage of this approach is that such multi-functionality results in a smaller, less massive thermal control/structural system. In addition, the TES component of the system is passive, having essentially no moving parts. Furthermore, the TES-system can be designed so that its thermal performance is g-load/orientation insensitive.

1.1. Project Scope and Objectives

Research focuses on development of TES sandwich-structures that combine the heat storage function with structural functionality. Heat storage is via the latent heat of a component of the composite structure. Light-weight system configurations whose performance is g-load/orientation insensitive are focused on. Three configurations have been considered:

1. One-dimensional Sandwich Structures: Plate-like laminates consisting of a thermally conductive/structural layer and a PCM impregnated TES-volume. Multiple laminates build up the lamination sandwich structure. The TES-volume may contain an additional thermal conductivity enhancer.
2. Two-Dimensional Box Structures: The PCM impregnated TES-volume contains additional transverse structural ribs for improved strength and rigidity. This results in a

slight reduction in heat storage capacity. The added ribbed-structure also limits options on the flow path of heat into/out from the TES-volume.

3. Three-Dimensional Lattice Structures: The TES-volume contains a grid of structural/conductive elements so that strength is isotropic in the plane of the sandwich structure.

Two material formulations are considered:

C. Metal/PCM Composites: Structural/thermally conductive elements are a metal (typically an aluminum micro-extrusion). The TES-volume is a PCM, which may include a thermal conductivity enhancer or other property modifier.

D. Graphite/PCM Composites: Structural elements are a graphite fabric/epoxy matrix composite. The TES-volume is PCM impregnated porous graphite open-cell foam[1] having a typical cell size of 500 μm.

In addition, key aspects of PCM performance are addressed

I. Volume Change at Phase Transition: A specific volume change generally accompanies phase transiton, so either a mechanical bellows mechanism or void volumes must be incorporated in TES-system design. A ***distributed bellows mechanism*** is developed, where polymeric micro-balloons are dispersed in the TES-volume. At phase transition, the micro-balloons reversibly callapse/expand absorbing this specific volume change.

II. Liquid-PCM Immobilization: Buoyancy-driven motion of liquid-PCM in meso-scale TES-volumes could make the heat storage function g-load or orientation sensitive. A polymeric co-polymer that immobilizes liquid paraffin is characterized.

III. Solid-Solid Phase Change Materials: Materials that undergo a solid state phase transition at appropriate temperatures with competitive latent heats offer certain packaging advantages relative to solid-liquid PCM. One such material is the Pentaglycerine-Neopentaglycol (PG/NPG) system. A new method to formulate PG/NPG solid solutions is proposed.

---

[1] POCO Foam, POCO Graphite Inc, 300 Old Greenwood RdDecatur, Texas 76234, USA.

1.2. Literature Review

1.2.1. Solid-Liquid PCM's

Solid-liquid PCMs for electronics temperature control include: salt hydrates, paraffin, certain hydrocarbons and metal alloys [Hale,1971]. Systems utilizing PCMs that undergo solid-liquid transition present material expansion and containment problems. In addition, their performance when the PCM is in the liquid phase could be sensitive to system orientation or g-loading. Hundreds of solid-liquid PCMs have been investigated by the research community. Based on these investigations the materials may be divided into two groups, organic and inorganic compounds. Two sub-groupings of the organic class PCMs are the paraffin's and the non-paraffin's. Compounds may be combined to give organic and inorganic eutectics (mixtures). Several materials from the above groups have melting points between 40°C and 120°C and their general characteristics are provided in Table 1.1.

Table 1.1 Summary of pcm types.

Property	Organic Paraffin	Organic Non-Paraffin	Inorganic Salt Hydrate	Inorganic Metal Eutectic
h_f (kJ/kg)	230-290	120-240	170-340	30-90
ρ (kg/m^3)	600-850	900-1800	900-2200	300-800
k (watt/m°C)	≈0.25	≈0.2	0.6-1.2	≈20
Thermal Expansion	High	Moderate	Low	Low
Corrosion	Low	Some are	Highly	Some are
Toxicity	No	Some are	Highly	Some are

Organic paraffin's exhibit a high heat of fusion, melt congruently and do not supercool. The drawbacks include poor thermal conductivity, low density and significant expansion upon the solid-to-liquid phase transition.

Non-paraffin organic materials are toxic, flammable and more expensive than the paraffin's. Inorganic salt hydrates and metallic eutectics are generally toxic and corrosive.

1.2.2. Polymer Additives For Liquid Immobilization

A new type of PCM known as shape stablilized PCM has been developed. Shape stabilization indicates that these composites inhibit motion of the liquid phase of solid-liquid PCM. One

approach for a shape-stabilized PCM is to imbed the solid-liquid PCM in a polymer matrix and the composite remains immobilized even at high temperatures.

Sayler claimed composites with high thermal conductivity and high thermal energy storage can form in a gel state. The matrices of the composite are: silica, polyolefin resin, polyethylene copolymer and polyethylene silica, fatty acid, fatty acid ester, primary alcohol or hydrocarbon, and water/urea or water as PCM [Sayler et al, 1992, Sayler et al, 1996, Sayler et al, 2000].

Inaba and Tu [1997] developed "shape-stabilized" paraffin (pentacosane) with HDPE as the polymer matrix. The density, specific heat, latent heat and effective thermal conductivity of the "shape-stabilized" paraffin were investigated.

Momose et al. [1998] characterized heat storage composites. These composites contain a thermoplastic elastomer and synthetic or natural rubber as the matrix and paraffin or high molecular weight monohydroxy alcohol as the TES components. The polymers ethylene-propylene-diene (EPDM) terpolymer and ethylene-vinyl acetate (EVA) and styrene-isoprene-styrene (SIS) are decribed in this work.

Hong and Xin-shi [2000] investigated the thermal storage performance of a "form-stable" composite based on paraffin and HDPE. The structure of the prepared composite was analyzed by scanning electronic microscopy (SEM) and the latent heat was investigated by DSC. Several kinds of HDPEs were evaluated as potential materials.

A heating device containing a rechargeable PCM was developed by Frohlich et al [2000]. The PCM may be provided in a variety of forms, including crystalline linear alkyl hydrocarbons, alkyl hydrocarbon waxes, crystalline fatty acids, linear crystalline primary alcohols, ethylene copolymers, polyethylene, polyethylene glycol, polyethylene oxide, and acetamide mixed with HDPE, EVA copolymer and silica.

Xiao and Gong described another phase-stabilized PCM: styrene-butadiene-styrene (SBS) triblock copolymer / paraffin. They claimed that no leakage occurred when the paraffin is in liquid state. By introducing expanded graphite, the thermal conductivity of the composite increased [Xiao et al, 2001, Xiao et al, 2002]. This high thermal conductivity composite exhibited nearly 80% of the latent heat of fusion per unit mass of the paraffin.

Buckley investigated the triblock co-polymers acrylonitrile butadiene styrene (ABS), styrene acrylonitrile (SAN) copolymer and thermoplastic elastomers that are matrix materials for a flexible composite with paraffin. It was claimed that this method of encapsulating the paraffin in the composite prevents the liquid PCM from migrating within the composite [Buckley, 2001].

Yamaguchi claimed that block copolymer, such as styrene-ethylene-butylene-styrene (SEBS), SIS, and styrene-propylene-styrene (SEPS) can also be used to make "shape-stabilized" PCM. Other candidates for the polymer matrix were selected from the olefin family such as: EVA copolymer, ethylene-acrylic ester (EAE) copolymer, ethylene-alpha-olefin copolymer, an amorphous polypropylene (PP), ethylene random copolymer, polyesters, polyamides and an epoxy resin [Yamaguchi, 2001].

The mechanical and thermal properties of frozen gels are investigated from ultra high molecular weight polyethylene (UHWPE) and paraffin waxes. The paraffin crystallizes without destroying the UHWPE gel network in the composite. The composite can store and release latent heat up to 200 J/g at the melting temperature of paraffin. A PCM laminate consisting of a polymer top and bottom was proposed to encapsulate the UHWPE/paraffin gel [Beginn et al, 2003].

Wirtz et al [2003b] investigated the thermophysical properties of paraffin/SEBS composites. The hermeticity and the stability of the composite were studied by thermal cycling tests. A mechanism proposed reveals that paraffin will partition to the hydrophobic block of the copolymer with the surrounding hydrophilic block providing encapsulation.

1.2.3. Solid-Solid PCM's

Most traditional PCMs are solid-liquid phase transition materials that have the disadvantage of large volume change during transition, possible leakage and short lifespan. Furthermore, when in the liquid phase, the material is subject to buoyancy effects, so performance of a TES-system could be sensitive to system orientation of g-loading. Solid-solid PCMs (SSPCMs) provide reliable performance. Some SSPCMs have the disadvantages of lower latent heat and higher transition temperature for thermal storage applications [Wang et al, 2000].

Many SSPCMs are polyalcohols, including pentaglycerine (PG), neopentaglycol (NPG), pentaerythritol (PE), 2-amino-2-methyl-1,3-propanediol (AMPL), and trihydroxy methyl-aminomethane (TAM), which have hydrogen-bonded lattices with either layered- or chain type structures. Using differential scanning calorimetric (DSC) and x-ray diffraction, binary phase diagrams for PG-NPG, PE-NPG, and NPG-AMPL systems have been established. These binary systems have different temperature ranges for phase transition. For example the NPG-PG binary system undergoes a solid-solid phase transition between 24°C and 86°C. [Chandra et al, 1989; 1990; 1991]The heat capacities of solid state thermal energy storage materials range from 188 to 474 J/mol K [Chandra et al, 2002]. Furthermore, the "micromechanism" of heat storage in binary systems including NPG-PE and NPE-TAM has been investigated. The "micromechanism" governs the heat storage behavior at the molecular level [Wang et al, 2000]. Trimethylolpropane

(TRMP) was investigated as a new candidate for thermal energy storage materials. In this PCM an orientationally disordered crystalline plastic phase was observed and the solid-solid phase transition temperature is 327.8 K [Chandra et al, 2002b].

Other Solid-Solid PCM "Form stable" silane graft copolymer, a polysiloxane (trade name Aqualink AT 980), was investigated as a solid-solid PCM. This material undergoes solid-solid phase transition between 125-130°C. Since its latent heat of fusion is as high as 180 kJ/kg, it can be used in thermal systems. Results indicated that this material can store energy in excess of 10^5 kJ in 0.5 m^3 [Wang et al, 2000]. Trans-1,4 polybutadiene(TPB) is a new solid-solid PCM developed by Ube Industries, Ltd. TPB has two stable crystalline structures and a transition temperature of 86°C [Iwamato et al, 2000]. Jiang and his coworker [2000a, 2002] investigated another PCM, which is the flexible polymer polyethylene glycol (PEG) with the rigid polymer cellulose diacetate (CDA) as the skeleton. Although PEG is a liquid-solid PCM it is effectively immobilized and behaves like a solid-solid PCM. The latent heat is approximately 200 J/g and the transition temperature can be controlled from 310-340 K. Two categories of patented SSPCM have been investigated – recticular SSPCMs and pectinate SSPCMs. Recticular SSPCMs have a maximum phase change enthalpy of 140 J/g, and phase change temperature of 0-55°C. Pectinate SSPCMs have a maximun phase change enthalpy of 150 J/g, and a phase change temperature of 0-60°C [Jiang et al, 2000b].

1.2.4. Thermal Conductivity enhancement - Graphite Foam

Numerical investigations show that because of its high thermal conductivity, graphite foam can enhance electronic cooling [Rachedi et al, 2001]. The use of graphite foam leads to a device temperature reduction of 50%. Appropriate parameters (Reynolds number, Darcy number and thermal conductivity) should be considered when choosing the material of foams.

Open cell metal foams are widely used in thermal encapsulation applications due to their high thermal conductivity. The study of Lu et al explored the use of open cell alumina foam for convective cooling in compact heat exchangers [Lu et al, 1998].

Carbon and graphite foams are good candidates for encapsulation of PCMs because of their high thermal conductivity, high surface area and low density. Pitch based graphitic foams have very high thermal conductivities. Graphite foams are interconnected networks of graphite ligaments,

which provide the foam with higher out-of-plane thermal conductivity than typical 1-D and 2-D carbon fiber reinforced composites [Klett et al, 2000].

A process for fabrication of two mesophase pitch-derived graphite foams (Mitsubishi ARA 24 and Conoco Dry Mesophase) was developed at Oak Ridge National Laboratories (ORNL). The graphitic foams are derived from naphthalene based synthetic pitch and mesophase pitch. These foams are carbonized at rate of 0.2 °C/min to 1000°C, and then graphitized at 10°C/min in argon to 2800°C with a 2 hr. soak at these temperatures. These pitch derived graphite foams range in density from 0.2 to 0.6 g/cm^3, and have average pore diameters from 275-350 μm for Mitsubishi ARA 24 based foam and from 60 to 90 μm for Conoco based foam [Klett et al, 1998, Klett et al, 2000].

From polarized light optical microscopy and SEM, the cell walls are highly aligned along the axis of the ligaments, resulting in a thermal conductivity of approximately 150 W/mK along the ligaments. By using the technique of xenon flash diffusivity, the out of plane thermal conductivity is measured and is relatively lower at about 50 W/mK, but still a considerable improvement over traditional carbon foams. Additionally, the bulk thermal conductivity of the graphitic foam was found to vary with density from 40-150 W/mK, which is over six times greater than the same weight of solid copper [Klett et al, 2002a, Klett et al 2002b, Klett et al, 2000].

Klett et al [2000a, 2000b, 2002c] from ORNL developed the process to produce a graphite foam heat sink. Filling the pitch based carbon foam with a PCM produces an effective heat sink device. Recently, a heat exchanger for a passenger automobile has been developed with heat transfer coefficients over two orders of magnitude greater than current metallic designs.

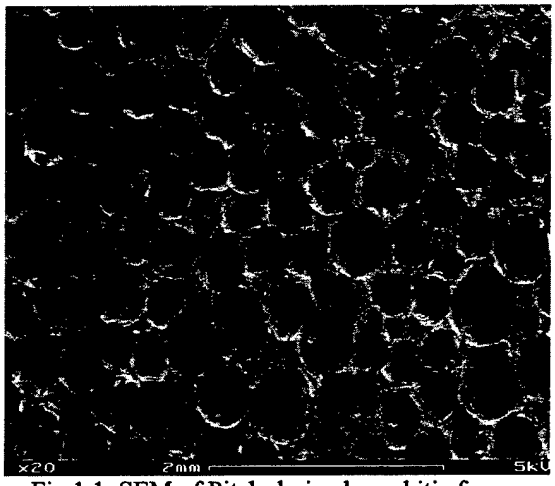

Fig.1.1 SEM of Pitch-derived graphitic foam.

Py et al developed a paraffin / porous-graphite-matrix composite as a high capacity and constant power thermal storage material. The thermal conductivity of the composite varies from 4 to 70W/mK and induced a decrease in the overall solidification time of paraffin and stabilized the thermal storage power [Py et al, 2001].

Gaies and Faber investigated the relationship between relative density and thermal conductivity and experimental results showed the higher the density of foam, the higher the thermal conductivity. Again, results showed that the heat conductivity out-of-plane (perpendicular to xy-plane) is significantly higher than in-plane (parallel to xy-plane). (Figure 1.2). Those studies offer some guidelines for future thermal management applications using graphite foam [Graies, 2001].

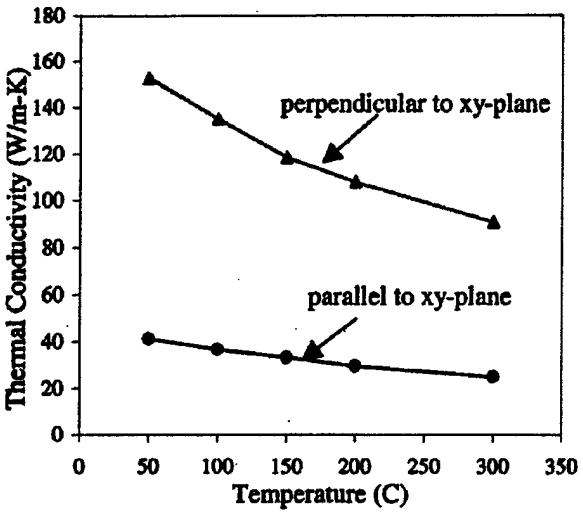

Fig. 1.2 Thermal conductivity values for graphite foam as a function of temperature.

1.2.5. Thermal Response Models and Applications

Avionics Applications In the early 1980's the feasibility of using selected PCMs was investigated for thermal management of spacecraft. Highly crystalline polymers were identified as potential PCMs for these applications [Sheffield et al, 1984].

Solid-liquid PCMs have been investigated as electric packaging materials for aerospace applications. Solid-liquid PCMs are capable of absorbing electrical waste heat. One candidate PCM is the paraffin, n-hexatricosane. The thermophysical properties (thermal conductivity, density, specific heat, latent heat of fusion, volume expansion) and phase change temperature of this paraffin were measured. The experimental results also showed that three metal matrix materials effectively enhanced the thermal transport through the PCM, aluminum foam and a lanced-offset finstock [O'Conner and Weber, 1997].

Transient thermal control of a PCM/honeycomb cell and a computational model for predicting the thermal performance of PCMs used in avionics electronic modules was developed. Two PCMs were used: paraffin (n-eicosane), and a eutectic alloy of Bi/Pb/Sn/In. The model results showed that the PCMs are effective candidates for passive cooling of electronic modules for transient periods [Pal and Joshi, 199; 1998]

A composite heat sink for aerospace applications consists of a solid porous matrix with encapsulated PCM in the pores. This design improved thermal performance (volume expansion of PCM, void formation) compared to a conventional solid-liquid PCM heat sink [Kulish and Lage, 2000].

Wirtz et al [1999] investigated the thermal response of a hybrid cooler which is charged with PG/NPG "dry" solid-solid PCM. They formulated the mathematical model that simulates the performance of the storage unit and tested the prototype heat sink that incorporates heat storage using this "dry" PCM.

Bauer and Wirtz [2000] describe a TES composite that incorporates PG as the PCM. A plate like, thermally conductive sandwich structure is used. The structure has aluminum plates as skin and an aluminum foam core impregnated with PG. The effect of the aluminum foam metal fraction on effective thermal conductivity of the sandwich structure is investigated. The composite is suitable for use in electronics packaging.

Zheng and Wirtz [2001] develop a semi-empirical thermal response model for a hybrid TES heat sink. PG, NPG and their solid solutions are used as solid-solid PCMs. The thermal response of a plate-type fin configuration is investigated. The design of a plate type TES unit is optimized to minimize the temperature difference between the base temperature and the transition temperature of the PCM. Two figures of merit for the hybrid TES unit are developed [Zheng and Wirtz , 2002]. The study shows that the volumetric figure of merit and the temperature control figure of merit are related to the performance specification of the storage unit and its physical design.

Wirtz et al [2003a] describe thermal and structural response models for graphite-epoxy/paraffin impregnated-graphite foam sandwich structures. It is shown that the graphite/epoxy shell provides structural functionality while it does not effectively participate in the heat spreading process. The thermal response model implies that the effective specific surface area of the foam is approximately 3X smaller than expected, leading to disappointing thermal control. Structural response models find that the graphite-epoxy shell of the composite effectively provides strength and rigidity.

Applications in Portable Electronics Common portable electronics include cellular phones, personal digital assistants and portable computers. Thermal management technologies using PCMs emerged for use in portable electronic devices in recent years.

The feasibility of using PCMs for accommodating transient heat loads in hand held portable electronics has been investigated. PCMs provide advantages such as size and weight reduction, and are particularly useful in accommodating peak thermal loads. Guidelines for designing transient thermal management systems were developed based on the transient convective/radiative heat transfer rate from the handset to the environment and parameters which effect the thermal management of the handset using PCMs. Advanced thermal energy storage

(TES) using PCMs coupled with a metal heat spreader or graphite loaded polymers was also developed. The effectiveness and proper material selection of the heat spreader was investigated [Hodes et al, 1999; 2000; Weinstein et al, 2001].

Research has been done on the use of passive energy storage with time varying workloads. Performance improvements were investigated using a thermal control unit (TCU) with PCMs. According to Vesligaj, "A TCU is an enclosure that contains PCM and a thermal conductivity enhancer, is located near the power source, and acts as an energy storage and heat-spreading module." Numerical simulations illustrated the effects of duty cycles and substrate thermal conductivity on the thermal performance of an electronic wearable computer system with passive energy storage. Also, the effectiveness of TCU as a thermal regulator under different operating conditions was reported [Vesligaj and Amon, 1999; Alawadhi and Amon, 2000].

The thermal reliability of PCMs used in Pentium III and Pentium III Xeon™ Processor Cartridges was investigated. The PCM melts after the electronic device starts to power up and has better thermal performance and is less expensive than thermal grease and paste. Thermal characterization results showed that the PCM can meet the Pentium III and Pentium III Xeon™ performance requirements. The PCM used as a thermal interface material was stable and reliable under extreme environmental tests [Chiu et al, 2000].

1.2.6. Structural Response Models and Applications

The development and deployment of multifunctional materials have significant impact on reducing the operating cost and the gross weight in aeronautical and space systems. For future aeronautical and space systems, materials and structures continue to be the key elements in determining reliability, performance, testability, and cost effectiveness [Noor et al, 2000; Renton, 2001].

Multifunctional materials, in addition to interacting with the surrounding electronic environment, support loads of the system. Multifunctional material represents a new manufacturing and integration technology by which communications, electronics equipment, and heat transfer elements are integrated into conformal load-bearing structures. Advances in large-scale integrated electronics packaging, lightweight composites structures, and high-conductivity materials make the technology feasible for the future applications. The integration effectively eliminates traditional boards and boxes, large connectors, bulky cables, and thermal base plates, yielding major weight, volume, and cost savings.

Textile structural composites are being widely used as multifunctional structures in aerospace, automobile, and marine industries. This is because they have favorable mechanical properties and attractive reinforcing materials with low fabrication cost and easy handling [Vandeurzen et al, 1995]. Characterization of textile composites becomes very important to the structural design. In the last 30 years, many researchers have continuously devoted their efforts to predicting mechanical properties of textile composites by making various assumptions. Earlier researches were carried out based on a large number of assumptions for simplifying the analysis procedures. The relevant approaches involved various rules of mixture approximations, composite cylinder models, and variation boundary methods [Yang et al,1986; Adams, 1989]. Kawabata et al. [1998] developed an analytical approach, a biaxial extension theory of woven fabrics. The method was capable of modeling textile composites at a micro geometry level and predicting effectively the mechanical properties and their dependence on their architecture parameters. However, the method is complicated and difficult to implement.

Finite element analysis (FEA) is a useful and versatile approach used by many researchers to predict mechanical properties of composite materials. A number of FEA models have been developed to determine the effects of various fiber architecture parameters on mechanical properties of the textile composites. The general procedure to predict the mechanical property of a textile composite using FEA consists of: (1) dividing the textile composite structure into a number of unit cells and analyzing the mechanical properties of a unit cell using FEA; and (2) reconstructing the entire reinforcement geometry by assembling the unit cells for predicting mechanical properties of the textile composites.

An early modeling of woven fabric reinforced structures was carried out by Ishikawa and Chou [1982]. They developed a "mosaic model" for analyzing elastic behavior of woven hybrid composites. In this model, a fabric composite was treated as an assemblage of pieces of asymmetrical cross-ply laminates neglecting the shear deformation in the thickness direction. The two-dimensional (2D) extent of a lamina was simplified to two one-dimensional (1D) models, the parallel model and the series model, depending on the arrangement of cross-ply laminates. This model used the lamination plate theory to calculate the mechanical stiffness and compliance of the cross-plied laminate units under the assumption of constant stress or strain.

Naik and Ganesh [1996] developed a 2D woven fabric composite strength model for predicting the failure strength of 2D plain weave fabric laminates under uniaxial static tension loading. This model was developed on the basis of the geometry defined by mathematical expressions derived by Ganesh and Naik [1996]. Using this model, the ultimate failure strength, stresses at different

stages of failure, the stress-strain history of 2D plain weave fabric laminates under uniaxial static tensile loading, and the effect of fabric geometry on the failure behavior were investigated. All these studies were carried out for the three idealized laminated configurations.

Zhang and Harding [1990] used the strain energy equivalence principle with the aid of the finite element method for the micromechanics analysis of the elastic constants of a plain weave fabric lamina. The plain weave fabric lamina was modeled by assuming the undulation in one direction only. It was suggested that this method should be extended to the case of a 2D undulation model.

Little research was conducted for plain weave metal mesh composites. Hübsch et al. [2000] presented a homogenization technique applied to the problem into the calculation of the equivalent material properties of a resin impregnated wire mesh. Wire mesh was used as orthodontic brackets for dental implants. The wire mesh (and the adhesive which has cured in its voids) has born a major influence on the stress field prevailing in the tooth/bracket system, particularly if the adhesive interface between the tooth and the bracket was considered. Using the homogenization theory, a single square of the wire mesh, together with the matching resin cast, was used as a representative volume element (r.v.e.), and a model capable of representing a material with a four-fold axis of the rotational symmetry was adopted. Because of the complicated geometry of the r.v.e., a finite element model was used instead of an analytical solution. It was found that the model differed very little from the transversally isotropic model.

2. TES-System Thermal Response

2.1. General Description Of Structure Components

Slab-Shaped TES-Volumes Figure 2.1.1 shows top and edge views of a slab shaped TES-volume sandwich structure. The TES-volume, of thickness $2t_p$, is contained between conductive heat spreader plates, each of thickness t_f. There may be additional structural elements ("structural ribs") contained in the TES-volume. The figure shows two sandwiches (four laminates) stacked together to form the composite plate.

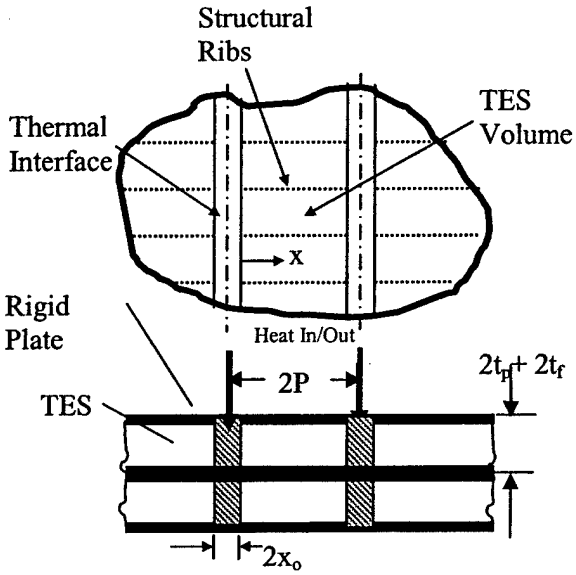

Fig.. 2.1.1 Slab TES-volume sandwich structure.

Heat input/output is via thermal interfaces (TI). The TI's are presumed to be in thermal contact with a heat source or sink, so the temperature of the source/sink will be directly related to the TI temperature. We assume the TI's make no contribution to the structural characteristics of the system. The configuration shown has a series of straight, rectangular TI's imbedded in the sandwich structure (two TI's are shown in the figure). The in-plane periodicity of the TI's is 2P. In storage mode, excess heat flows into the thermal interface, and then outward (in the x-direction) from the TI through the conductive heat spreader plates and to the TES-volume. In the heat release mode of operation, stored energy flows back to the heat spreader plates, inward toward the TI, and then to the heat

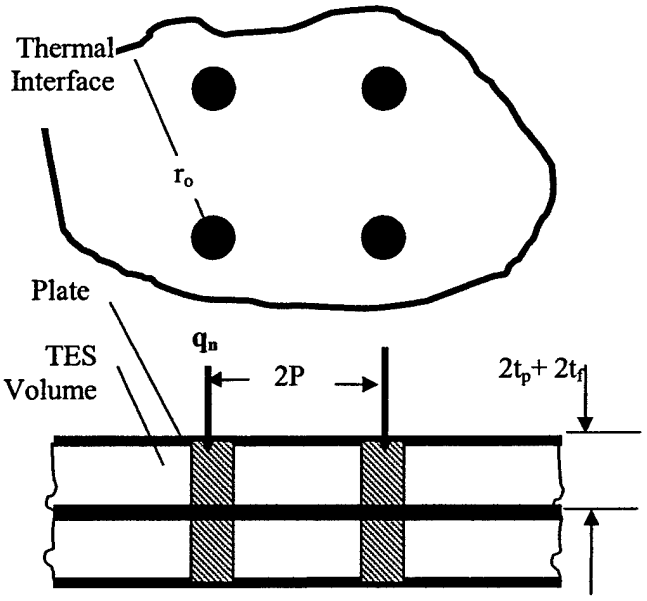

Fig. 2.1.2 Radial heat flow TES sandwich structure.

sink of the system.

Disk Shaped TES-Volumes Figure 2.1.2 shows an alternative configuration, where cylindrical-shape TI's are laid out in a grid, with periodicity 2P. In this case, heat flow to/from the TES-volume is primarily radial so that the heat flux is proportional to 1/r. Because of this, the description of the thermal response model of this configuration is treated separately from the *Slap-Shaped* configuration.

2.2. Thermal Response Models for Slab-Shaped TES-Volumes

An operable unit cell for analysis of the configuration shown in Fig. 2.1.1 is shown in Fig. 2.2.1. It consists of a rectangular slab of heat spreader/TES-volume in thermal contact with a segment of TI. The heat transfer to/from the TI segment is

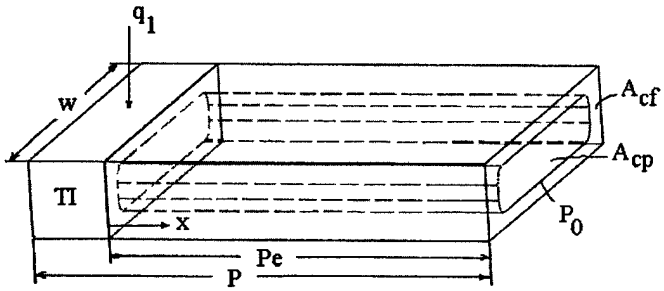

Fig. 2.2.1 Slab-shaped TES unit cell.

$$q_1(\tau) = q_{ref} F(\tau) \qquad (2.2.1)$$

where q_{ref} is a reference quantity and τ is time. The total slab length is P (TES-composite half-periodicity). The heat spreader has length Pe, cross sectional area Ac_f and thermal conductivity k_f. The interfacial contact conductance between the TI and heat spreader is h_i. The TES-volume has length Pe, cross sectional area Ac_p, thermal conductivity k_p, volumetric latent heat h_v and transition temperature T_{tr}. The TES-volume may contain a thermal conductivity enhancement such as graphitic foam or a paraffin immobilizer such as SEEPS, so k_p and h_v may be "effective" properties.

The TI is characterized by its sensible heat capacity (mc) and its temperature is *assumed to be spatially uniform*. An energy balance gives

$$mc \frac{dT_{TI}}{d\tau} = q_1(\tau) - q_{f,0} \qquad (2.2.2)$$

where T_{TI} is the TI temperature and $q_{f,o}$ is the heat transfer rate from the TI volume. *Assume* $k_p Ac_p << k_f Ac_f$.[2] Then

---

[2] Ac_f and Ac_p are of the same order of magnitude, while k_p is typically order 0.2 watt/mK while k_f could range from 50 watt/mK to 400 watt/mK.

$$q_{f,0} = h_i Ac_f \left(T_{TI} - T_{f,0}\right) \tag{2.2.3}$$

where $T_{f,o}$ is the spreader temperature at x = 0. *Assume the sensible heat capacity of the spreader (fin) and TES-volume is small compared to the latent heat capacity of the TES-volume*[3]. Then, the thermal response of the spreader and TES-volume are both quasi-steady. An energy balance on an Ac_f by dx volume of spreader gives

$$\frac{\partial^2 T_f}{\partial x^2} - \frac{q_p'}{k_f Ac_f} T_f = 0 \tag{2.2.4}$$

while a similar balance on the phase transition interface in the TES-volume (Fig. 2.2.2) gives

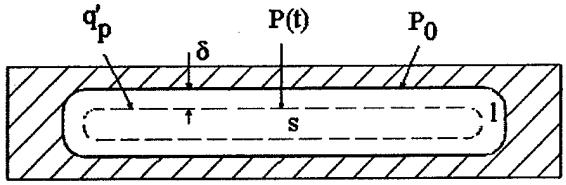

Fig. 2.2.2 Section end view of slab shaped TES structure

$$\frac{\partial \delta}{\partial \tau} = \frac{q_p'}{h_v P(\delta)} \tag{2.2.5}$$

where $\delta(x,\tau)$ is the extent of the "melt" region, and $P(x,\tau)$ is the perimeter of the liquid-solid interface. q'_p is the heat transfer rate per length (x) from the spreader volume to the TES-volume. Since the process is quasi-steady, it can be characterized in terms of shape factor, S

$$q_p' = k_p S\left(T_f - T_{tr}\right) \tag{2.2.6}$$

with

$$\overline{S} = \frac{S_o}{1 + RiS_o} \tag{2.2.7}$$

where S_o is the conduction shape factor normally associated with 2-dimensional conduction between isothermal surfaces [Mills, 1999], and

$$Ri_p = \frac{k_p}{h_{i,p} P_o} \tag{2.2.8}$$

is the dimensionless spreader-to-PCM contact resistance. If the PCM in liquid phase fully wets the spreader surface, then $Ri \approx 0$.

---

[3] The sensible heat effect of the spreader and PCM can be included into the TI-mc

Problem Scaling Define the following dimensionless variables:

$$\bar{x} = \frac{x}{Pe} \qquad \bar{\tau} = \frac{\tau}{\tau_{ref}} \qquad \bar{\delta} = \frac{\delta}{\delta_{\max}} \qquad \bar{q} = \frac{q}{q_{ref}} \qquad \bar{T} = \frac{T}{T_{ref}} \tag{2.2.9}$$

where

$$\tau_{ref} = \frac{Ac_p Peh_v}{q_{ref}} \qquad T_{ref} = \frac{q_{ref}}{k_p Pe} \tag{2.2.10}$$

The reference time, τ_{ref} is the time to "melt" the PCM in the TES-volume (if mc = 0), and T_{ref} is a convenient reference temperature. The equations (2.2.1) – (2.2.8) can be combined and summarized as follows:

$$MC\frac{d\bar{T}_{TI}}{d\bar{\tau}} = F(\bar{\tau}) - \bar{q}_{f,0} \tag{2.2.11}$$

$$R_k \bar{q}_{f,0} = Ri\left(\bar{T}_{TI} - \bar{T}_{f,o}\right) \tag{2.2.12}$$

$$\frac{\partial^2 \bar{T}_f}{\partial \bar{x}^2} - \bar{K}^2 \bar{T}_f = 0, \qquad \bar{K} = \sqrt{\frac{\bar{S}(\bar{\delta})}{R_k}} \tag{2.2.13a,b}$$

$$\frac{\partial \bar{\delta}}{\partial \bar{\tau}} = A\frac{\bar{S}(\bar{\delta})}{\bar{P}(\bar{\delta})}\bar{T}_f, \qquad \bar{P}(\bar{\delta}) = \frac{P(\delta)}{P_o} \tag{2.2.14a,b}$$

Suitable initial and boundary conditions are:

$$\bar{T}_{TI}(0) = \bar{T}_f(\bar{x},0) = \bar{\delta}(0) \tag{2.2.15}$$

$$\bar{T}(0,\bar{\tau}) = \bar{T}_{f,0}, \qquad \left.\frac{\partial \bar{T}_f}{\partial \bar{x}}\right|_{\bar{x}=1} = 0 \tag{2.2.16}$$

The coefficients in Eqs. (2.2.11 – 2.2.14) are:

$$MC = \frac{mc \cdot q_{ref}}{k_p h_v Pe^2 Ac_p} \tag{2.2.17}$$

$$R_k = \frac{k_f Ac_f}{k_p Pe^2} \tag{2.2.18}$$

$$Ri = \frac{k_f}{h_i Pe} \tag{2.2.19}$$

$$Ri_p = \frac{k_f}{h_{i,p} P_o} \tag{2.2.20}$$

$$A = \frac{Ac_p}{\delta_{\max} P_o} \tag{2.2.21}$$

The thermal response is completely described by these five dimensionless parameters and shape factors S and P/P_o.

Uniform δ solution Wirtz et al [2003b] have shown that when $k_p Ac_p << k_f Ac_f$, melting of the PCM occurs at a spatially uniform rate so that $\delta = \delta(\tau)$ only. Then $\overline{K}$ is a function of time only, so Eq. (2.1.13, 16) can be solved to give the spreader temperature distribution,

$$\overline{T}_f(\bar{x},\bar{\tau}) = \overline{T}_{f,0} \frac{\cosh\left[\overline{K}(1-\bar{x})\right]}{\cosh \overline{K}} \tag{2.2.22a}$$

and heat transfer rate at the TI-to-spreader interface,

$$\overline{q}_{f,0} = R_k \overline{K} \tanh\left[\overline{K}\right] \overline{T}_{f,0} \tag{2.2.22b}$$

Since $\delta = \delta(\tau)$ only, Eq. (2.2.14) must be written as

$$\frac{\partial \overline{\delta}}{\partial \overline{\tau}} = A \frac{S(\overline{\delta})}{P(\overline{\delta})} \overline{T}_{f,av}, \quad \overline{T}_{f,av} = \int_0^1 \overline{T}_f d\bar{x} = \frac{\tanh \overline{K}}{\overline{K}} \tag{2.2.23a,b}$$

where $\overline{T}_{f,av}$ is the average spreader plate temperature. Then Eqs. (2.2.11, 2.2.12, and 2.2.23) can be rearranged to give

$$\frac{d\overline{\delta}}{d\overline{\tau}} = A \frac{S(\overline{\delta})}{P(\overline{\delta})} \frac{\tanh \overline{K}}{\overline{K}} \frac{\overline{T}_{TI}}{1 + Ri\overline{K} \tanh \overline{K}} \tag{2.2.24}$$

$$\frac{d\overline{T}_{TI}}{d\overline{\tau}} = \frac{1}{MC} \left\{ F(\overline{\tau}) - \frac{R_k \overline{K} \tanh\left[\overline{K}\right] \overline{T}_{TI}}{1 + Ri\overline{K} \tanh \overline{K}} \right\} \tag{2.2.25}$$

These two equations may be solved using standard numerical techniques.

2.2.1. *Negligible TI Thermal Mass and Internal Thermal Resistance*

Under these conditions (MC = Ri = Ri_p = 0), $\overline{q}_{f,0} = \overline{q}_1$ and $\overline{T}_{TI} = \overline{T}_{f,0}$. Then, from Eq. (2.2.22b)

$$\overline{T}_{TI} = \frac{F(\overline{\tau})}{R_k \overline{K} \tanh[\overline{K}]} \tag{2.2.26}$$

and Eq. (2.2.24) becomes

$$\frac{d\overline{\delta}}{d\overline{\tau}} = \frac{A}{\overline{P}(\overline{\delta})} F(\overline{\tau}) \tag{2.2.27}$$

In the following sections, we look at four different slab structure configurations to Eq. 2.2.22-27.

2.2.2. *Simple 1D Sandwich Structures*

The 1D sandwich structure (Fig. 2.2.3) consists of a TI of length W, in thermal contact with two heat spreader plates, each of thickness t_f. The TES-volume, of thickness $2t_p$ is bounded above and below by the heat spreaders. Under these conditions (Fig. 2.2.4)

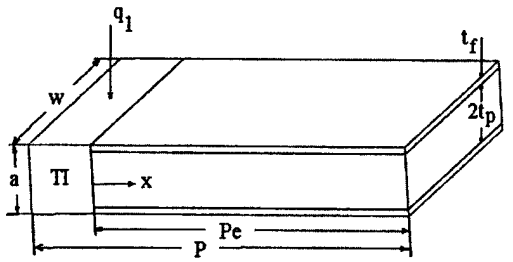

Fig. 2.2.3 Simple 1D sandwich structure unit cell.

$$P_o = 2W\,,\; Ac_p = P_o t_p\,,\; Ac_f = P_o t_f \tag{2.2.28}$$

and

$$S_0 = \frac{2W}{\delta_{\max}\overline{\delta}}\,,\; \overline{P} = 1 \text{ and } \delta_{\max} = t_p \tag{2.2.29}$$

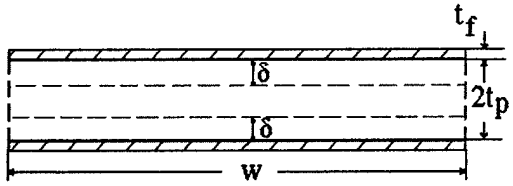

Fig. 2.2.4 Section end view of 1D sandwich structure

Furthermore, for this configuration $A = 1$ (Eq. 2.2.21), always.

<u>*Negligible TI Thermal Mass and TI-to-Spreader Thermal Resistance*</u> Under these conditions,

$$\overline{\delta} = \int_0^{\overline{\tau}} F(\overline{\tau})\, d\overline{\tau} \tag{2.2.30}$$

and

$$\overline{T}_{TI} = \frac{F(\overline{\tau})}{R_k \overline{K} \tanh \overline{K}} \tag{2.2.31}$$

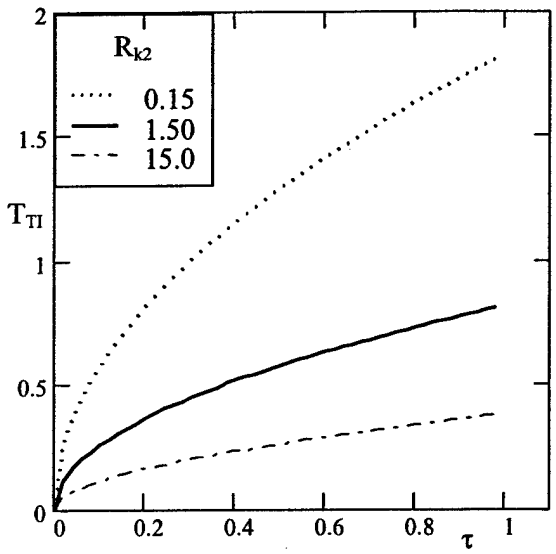

Fig. 2.2.5 Simple laminate TI time response. A = 1, MC = Ri = Ri_p = 0

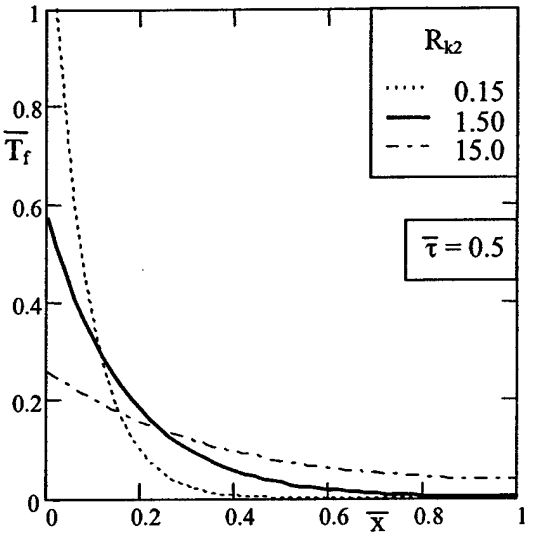

Fig. 2.2.6 Simple laminate spreader temperature distribution. A = 1, MC = Ri = Ri_p = 0

so the dimensionless parameters Rk and $\overline{K}$ completely describe the thermal response of the system. In fact, for this application in Eq. (2.2.30), $\tanh \overline{K} \approx 1$, so the solution, Eq. (2.2.29) becomes

$$\overline{T}_{TI} = \sqrt{\frac{t_p \overline{\delta}}{2WR_k}} \tag{2.2.32}$$

Consequently, only a single parameter effectively controls the solution[4], $R_{k2} = 2WRk / t_p$.

Figure 2.2.5 shows the TI thermal response due to a step input in energy ($F(\overline{\tau}) = 1$). The response for three values of Rk_2 is plotted. The figure shows that increasing Rk_2 reduces the TI's temperature excursion. Eq. (2.2.28) shows that for this case $\overline{\delta} = \overline{\tau}$, so in Fig. 2.2.5 $\overline{T}_{TI} \propto \sqrt{\overline{\tau}}$.

Figure 2.2.6 plots heat spreader temperature profiles at $\overline{\tau} = 0.8$ for the same values of Rk_2. The figure shows the temperature distribution is more uniform with increases in Rk_2. Thus, the uniform δ assumption regarding Eq. (2.2.14) becomes increasingly valid with increases in Rk_2.

[4] The thermal response is actually independent of W if the heat input is specified as q_1/W. However, our formulation assumes W and q_1 are individual design parameters.

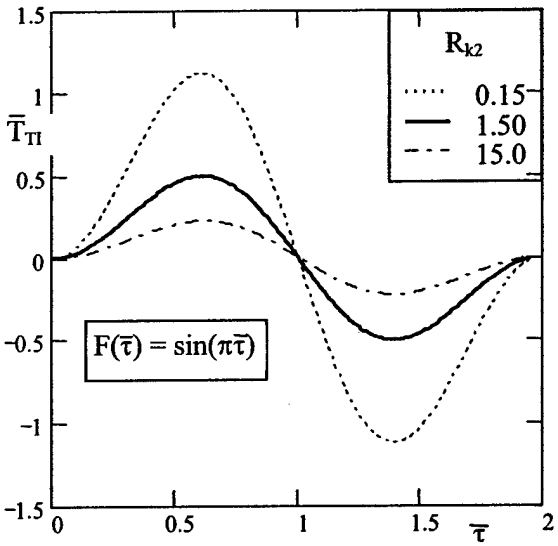

Fig. 2.2.7 Simple laminate TI time response. A = 1, MC = Ri = Ri_p = 0

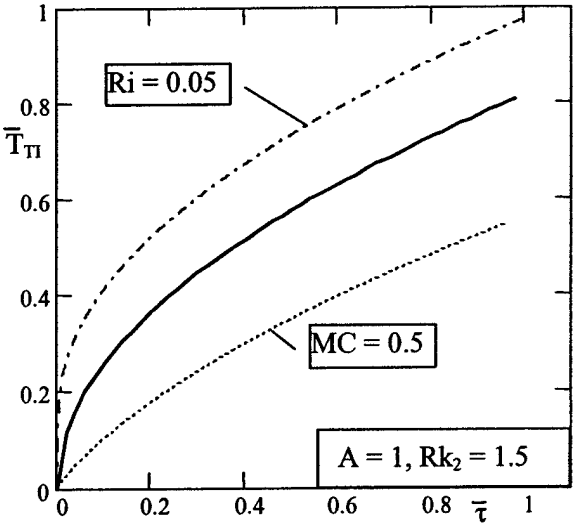

Fig. 2.2.8 Effect of TI mass and thermal resistance on simple laminate response.

Figure 2.2.7 plots the TI temperature response for the periodic heating/cooling case, $F(\bar{\tau}) = \sin \pi\bar{\tau}$, illustrating that the model can be easily applied to more general thermal storage situations.

Figure 2.2.8 considers the more general situation where MC and Ri are not zero. In this case, Eqs. (2.2.24, 2.2.25) govern the temperature response of the system. The plot compares the MC = Ri = 0 case (solid line in Fig. 2.2.8) with two cases. On the one hand MC = 0.5, Ri = 0, Ri_p = 0 (dotted line), while on the other hand MC = 0 while Ri = 0.05, Ri_p = 0. The figure shows that a massive TI decreases the temperature excursion of the system while thermal resistance at the TI – spreader plate interface increases the temperature excursion. A similar effect obtains with $Ri_p \neq 0$.

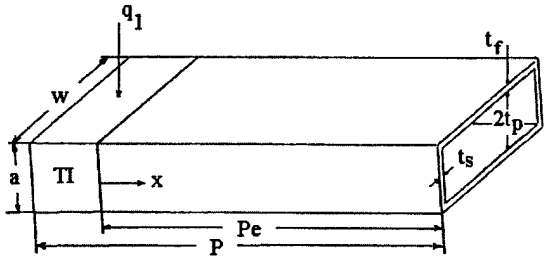

Fig. 2.2.9 2D Box unit cell.

2.2.3. Two-Dimensional Box Structures

Consider the laminated TES-structure shown in Fig. 2.2.9. The figure shows a W-wide segment of a 2-D structure, which consists of parallel rigid conductive plates

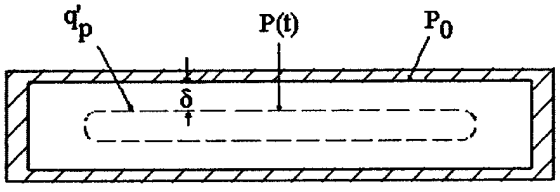

Fig. 2.2.10 Section end view of 2D Box unit cell.

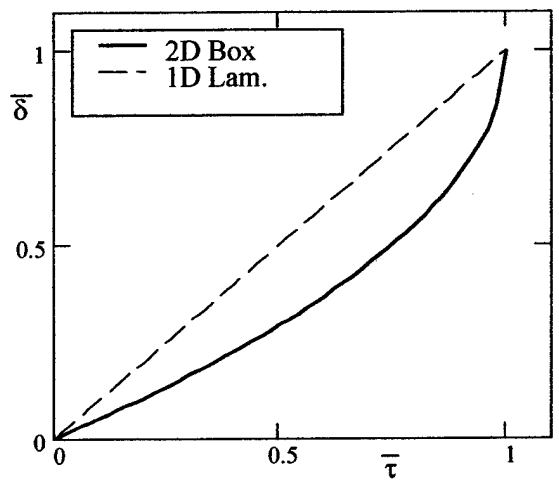

Fig. 2.2.11 Melt region growth, 1D laminate and 2D box laminate

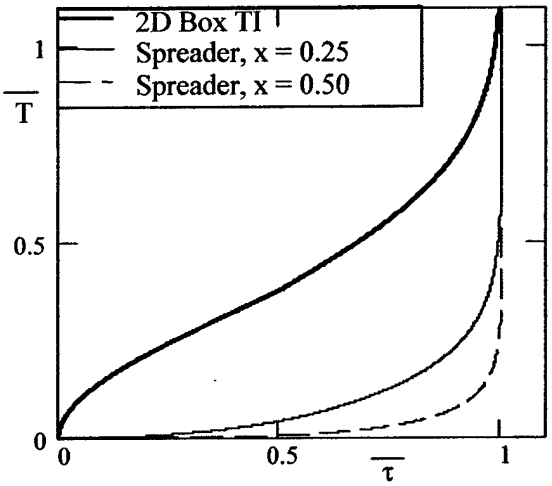

Fig. 2.2.12 2D Box thermal response. A = 0.5, R_k = 0.3, MC = Ri = Ri_p = 0.

ribs) alternately placed between segments of the TES-volume. The period of the structural ribs is W. Additional rigid conductive plates of thickness t_f enclose the TES-volumes, forming a *2-D box structure*. Heat input to each segment (of width W) is q_n where n is the number of laminations. The plate material and TI are of high thermal conductivity material such that the condition, $k_p\ Ac_p << k_f\ Ac_f$ is satisfied. Since the thermal conductivity of the plate material (k_f, k_s) is much greater than that of the PCM contained in the channels (k_p), heat flow is primarily from the TI along the conductive plates, and then into the PCM.

The structure can be analyzed by considering a single lamination of a single channel segment of width, W, as shown in Fig. 2.2.9. Heat input is $q_l = q_n/n$. For simplicity in this example, we assume that the channel has a square cross section of width and height $2t_p$. Also, let $t_s = t_f$ and $k_s = k_f$. Under these conditions (Fig. 2.2.10)

$$P_o = 8t_p \qquad Ac_p = 4t_p^{\,2} \qquad Ac_f = 2W\left(t_p + t_f\right) - Ac_p \qquad \delta_{\max} = t_p \tag{2.2.33}$$

and the solid-liquid perimeter and conduction shape factor [Mills, 1999] are

$$\overline{P}(\overline{\delta}) = 1 - \overline{\delta}\,, \qquad So(\overline{\delta}) = \begin{cases} \dfrac{2\pi}{.93\ln\left[\dfrac{.947}{1-\overline{\delta}}\right]}\,, & \overline{\delta} > 0.143 \\ \dfrac{2\pi}{.785\ln\left[\dfrac{1}{1-\overline{\delta}}\right]}\,, & \overline{\delta} \le 0.143 \end{cases} \tag{2.2.34}$$

and for a "square" box section $\overline{A} = 0.5$.

Negligable TI Thermal Mass and Internal Thermal Resistence Consider the case where $F(\bar{\tau}) = 1$. Under these conditions, Eq. (2.1.27) may be integrated and $\bar{\delta}$ satisfies the following equation:

$$2\bar{\delta} - \bar{\delta}^2 = \bar{\tau} \tag{2.2.35}$$

Figure 2.2.11 compares $\bar{\delta}(\bar{\tau})$ for the 1D Laminate and 2D Box configurations. Whereas the simple Laminate exhibits uniform (in time) growth, the more complex geometric configuration shows accelerated growth as $\bar{\delta} \to 1$. Fig. 2.2.12 shows how this translates into a smaller temperature excursion during the initial transient of the 2D Box configuration, with an accelerated temperature excursion at later time.

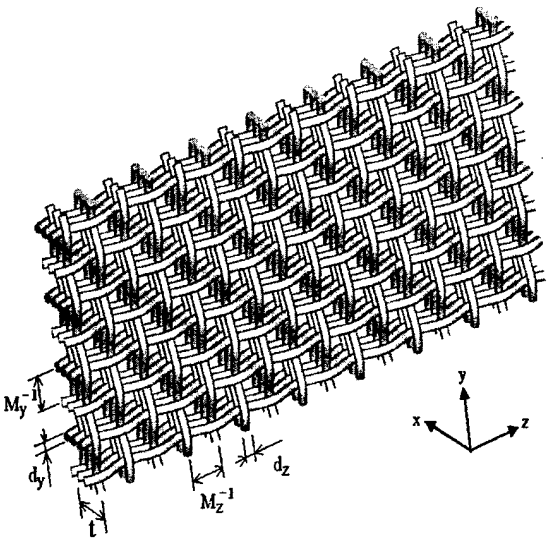

Fig. 2.2.13 Screen laminate geometry.

2.2.4. Box Structures with Screen-Laminate Structural Ribs

Xu and Wirtz [2003] have shown that laminations of plain-weave screens, such as shown in Fig. 2.2.13, can be configured to have porosity ranging to 0.47, with high specific surface area and in-plain effective thermal conductivity ranging to greater than 30% of the screen material value (60 watt/mK for aluminum screen laminates). This suggests that light weight 2D Box TES-structures (or Lattice structures to be described in the following Section) that employ this technology as structural ribs could be fabricated. The concept is shown in Fig 2.2.14. In addition to providing a lighter weight structure, the screen lamination would provide for increased contact with the PCM in the TES-volume. Unfortunately, mechanical testing described in Chapter 3 of this report showes that, due to the serpentinity of the laminate wire filaments, the screen laminates exhibit poor strength characteristics. We have not persued the idea further.

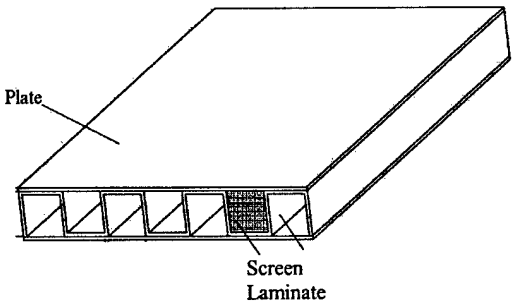

Fig. 2.2.14 2D Box employing corrigated screen-lamination as structural ribs.

2.2.5. Lattice Structures

Consider the Lattice structure shown in Fig. 2.2.15. Structural ribs of thickness t_s span the TES-volume in both longitudinal and transverse directions so that the PCM-composite is now fully compartmentalized and bounded by conductive material. The periodicity of the internal structure is L so that $Pe = n_L L$ where n_L is the number of sub-volumes in the longitudinal direction. The volume of each sub-volume is $2t_p L_p^{\,2}$ where $L_p = L - t_s$.

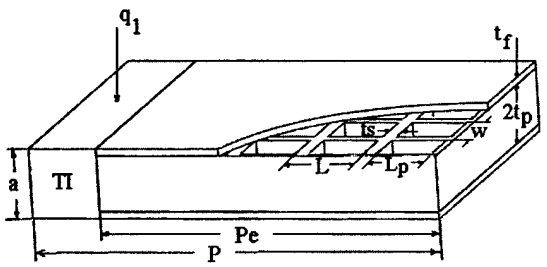

Fig. 2.2.15 Lattice structure.

We can analyze this structure by consideration of a single longitudinal row of sub-volumes of width W = L and thickness $a = 2(t_p + t_f)$ Heat input to the row is q_1. Then the volume fraction PCM, specific surface area and effective perimeter are, respectively

$$\varepsilon = \frac{2t_p L_p^{\,2}}{aWL}, \quad \beta = \frac{2L_p(4t_p + L_p)}{aWL}, \quad P_o = \frac{\beta(aWL)}{Pe} \tag{2.2.36}$$

Equivalent Concentric Tube Model

Consider the equivalent, circular cross section structure shown in Fig. 2.2.16. It consists of a TI of thermal mass (mc) attached to a hollow cylindrical heat spreader (tube) having cross sectional area Ac_f; the enclosed TES-volume has cross sectional area Ac_p; and, the two structures have the same interfacial perimeter, P_o (Fig. 2.2.17).

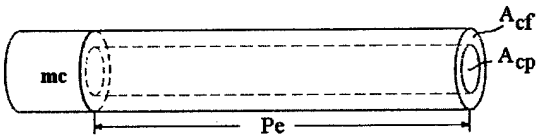

Fig. 2.2.16 Concentric tube unit cell.

$$Ac_p = \varepsilon aW, \quad Ac_f = (1-\varepsilon)aW, \quad r_p = \frac{P_o}{2\pi}, \quad \delta_{\max} = r_p \tag{2.2.37}$$

Then,

$$\overline{P}(\overline{\delta}) = 1 - \overline{\delta}, \qquad S_o(\overline{\delta}) = \frac{2\pi}{\ln\left[\frac{1}{1-\overline{\delta}}\right]}, \qquad A = \frac{\varepsilon aW}{\delta_{\max} P_o} \tag{2.2.38}$$

The perimeter and shape factor functions are very similar to those of the 2D Box structure, Eqs. (2.2.34). However, for the present case, A is not fixed at 0.5. Eqs. (2.2.24 and 25) in conjunction with Eqs. (2.2.22) describe the system response.

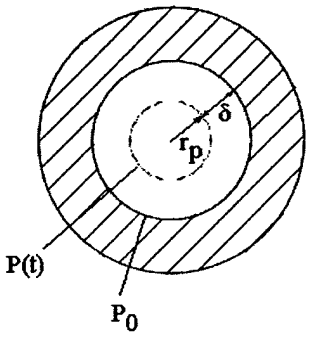

Fig. 2.2.17 Lattice "concentric tube" section end view

Negligable TI Thermal Mass and Internal Thermal Resistence

Under these conditions, $\overline{\delta}$ satisfies Eq. 2.2.35, and then the temperatures are given by Eqs. (2.2.26) and (2.2.22a). Note that the solution is independent of A. Since the shape factors for the 2D Box and Lattice are similar; and, the Solution is independent of A, the 2D Box and Lattice structures will have essentially the same response characteristics as shown in Fig.2.2.11, 12.

2.2.6. Metal/PCM Sandwich Structure Thermal Response, Comparison of Three Configurations

In order to assess the relative viability of these designs, in the following we compare the three configurations on the basis of equal storage capacity and key dimensions.

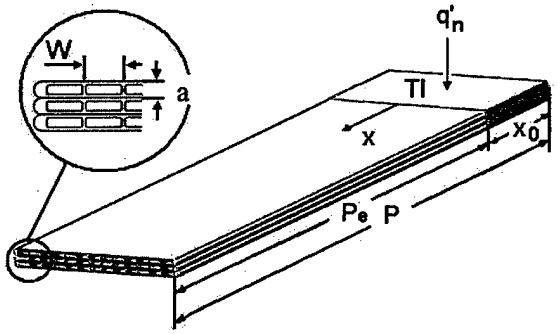

Fig. 2.18 Aluminum mesochannel TES-composite.

Consider the laminated TES-structure shown in Fig. 2.2.18. It consists of laminated PCM-impregnated micro-channel aluminum plates of thickness (a) and length Pe attached to a thermal interface. Heat input per unit width to the TI is q'_n where n is the number of laminations. Each plate of the lamination is hollow, with a number of mm-scale parallel channels of periodicity W and height t_p running in the x-direction. These plates, called micro-extrusions, are manufactured by Thermalex Inc. [Thermalex, 2003]. Since the thermal conductivity of the plate material (k_f) is much greater than that of the PCM contained in the channels (k_p), heat flow is primarily from the TI along the aluminum, and then into the PCM.

The 2D Box structure shown in Fig. 2.2.18 will be used as the basis for comparison. We assume, for convenience that the plate channels are of square cross-section. Characteristics of this structure and 1D Laminate and Lattice structures having the same storage capacity are summarized in Table 2.2.1. In each case, we consider a segment of the structure having width W,

and assume each device is charged with a PCM having the same thermophysical properties (n-docosane). Each structure is assumed to have the same face area, with storage volume of 1.6 cc.

Table 2.2.1 Summary of properties.

Common Properties: W = 5 mm, Pe = 100 mm, t_f = 0.5 mm, V_p = **1.6 cc**, Ac_p = 16 mm^2, k_f = 0.28 watt/mK, k_p = 0.28 watt/mK, h_v = 289 j/cc									
Configuration	a mm	δ_{max} mm	P_o mm	Ac_f mm^2	A	R_k	$2W/t_p$	ε	β m^{-1}
1D Laminate. t_p = 1.6mm	4.2	1.6	10	5	1.0	0.31	6.25	0.76	476
2D Box t_p = 2 mm	5	2	16	9	0.5	0.56	5.00	0.64	640
Lattice, tp = 2mm L=5mm, t_s=0.53mm	5	3.55	22.3	9	0.2	0.56	5.00	0.64	892

The table shows that at equal capacities, the 1D Laminate is thinner that the other two configurations. Therefore, it has the smallest maximum conduction length in the TES-volume (δ_{max}). However, it has the smallest spreader plate-to-PCM contact area ($P_o\beta$). It also has the smallest value of R_k, indicating that the temperature drop along the spreader plate will be largest.

Figure 2.2.19 plots the dimensionless TI temperature response for the three configurations. The figure shows that the ultimate temperature rise of the 1D Laminate is smaller than that of the other two configurations. However, the 2D Box and Lattice perform very similarly; and they outperform the 1D Laminate up to $\bar{\tau} \approx 0.8$ Apparently the greater specific surface area of the 2D Box and Lattice configurations initially dominates the solution. Eventually the shorter conduction length in the TES-volume of the Simple Laminate maintains the rate of increase of the TI-temperature at the smaller value. The difference in the performance of the three solutions is considered to be relatively insignificant.

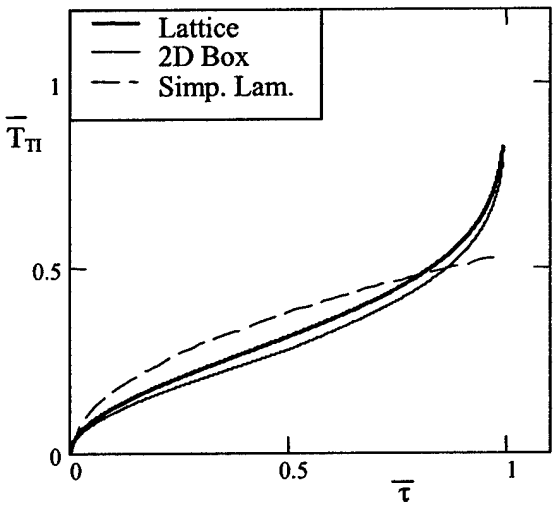

Fig. 2.2.19 Comparison, TI temperature response of three configurations having equal storage capacity.MC = Ri = Ri_p = 0

2.2.7. Thermal Conductivity Enhanced TES-Volumes

The thermal conductivity of the PCM's employed for this application is typically of the order of 0.25watt/mK. The laminate structures described in Sections 2.2.2 – 2.4.5 ameliorate this problem by introducing plate-like conductive elements adjacent to thin layers of PCM, so that conduction

to/from the PCM mass is across short lengths, giving rise to thermally responsive TES-systems. An alternative approach is to imbed the PCM in an open cell conductive foam such as aluminum foam or pitch-derived graphite foam. Aluminum foam (as produced) has a relatively low metal fraction. As a consequence, its specific surface area and effective thermal conductivity are generally low [Calmidi and Mahajian, 1999]. For example, the effective thermal conductivity of aluminum foam is typically only about 6% of the base metal value (12 watt/mK). On the other hand, woven structures can be fabricated to have effective thermal conductivity approaching 78% of the base metal value with specific surface area as high as 10^4 m^{-1} [Wirtz et al, 2002b]; and, graphitic foams are available that have effective thermal conductivities ranging to 50 watt/mK. The trade-off is a reduction in TES-volume thermal storage capacity.

The thermophysical properties of these materials are typically characterized by their density (ρ_p), porosity (ε), specific surface area (β) and effective thermal conductivity (ke_f). *Since ke_f will be much greater than k_p, assume heat flow is from the TI to the foam ligaments, and then from the ligaments to particles of PCM imbeded in the ligaments.* We can model the thermal response of any of the three geometrical configurations discussed in Sections 2.2.2 – 2.2.4. Given (ε, β, ke_f), the thermophysical properties of the PCM (ρ_p, k_p), and the overall dimensions of the PCM-impregnated foam TES-volume, key dimensional characteristics can be determined:

$$Ac_p = \varepsilon aW, \quad Ac_f = (1-\varepsilon)aW, \qquad P_o = \beta aW \tag{2.2.39}$$

At the PCM-particle in foam-cell level, heat transfer is three-dimensional. We can capture essential characteristics of this process by recourse to the Equivalent Concentric Tube model described in Section 2.2.5 (Fig. 2.2.16). Replace the TES-volume with n_{tube} micro- tubes such that Ac

$$n_{tube} = \frac{Ac_p}{\pi r_{e,p}^{\ 2}} \text{ and } n_{tube} = \frac{P_o}{2\pi r_{e,p}} \tag{2.2.40a, b}$$

where $r_{e,p}$ is the micro-tube TES-volume diameter (equivalent to the foam cell diameter).
Equating Eq. (2.2.40 a and b) gives

$$r_{e,p} = \frac{2\varepsilon}{\beta}, \qquad n_{tube} = \frac{aW\beta^2}{4\pi\varepsilon} \text{ and } Ac_{e,f} = \frac{Ac_f}{n_{tube}} \tag{2.2.41a,b,c}$$

Then

$$\delta_{\max} = r_{e,p}, \qquad \overline{P}(\overline{\delta}) = 1 - \overline{\delta}, \qquad S_o(\overline{\delta}) = \frac{2\pi}{\ln\left[\frac{1}{1-\overline{\delta}}\right]} \tag{2.2.42}$$

and

$$A_{tube} = \frac{Ac_p}{\delta_{\max} P_o}, \qquad MC_{tube} = \frac{mc \cdot q_{ref}}{n_{tube} k_p h_v Pe^2 Ac_p}, \qquad R_{k,tube} = \frac{ke_f Ac_f}{n_{tube} k_p Pe^2} \tag{2.2.43a}$$

$$Ri_{tube} = \frac{ke_f}{h_i Pe}, \qquad Ri_{p,tube} = \frac{n_{tube} ke_f}{h_{i,p} P_o} \tag{2.2.43b}$$

Eqs. (2.2.24 and 25) in conjunction with Eqs. (2.2.22) describe the system response.

Negligible TI Thermal Mass and Internal Thermal Resistance Under these conditions, $\overline{\delta}$ satisfies Eq. 2.2.35, and then the temperatures are given by Eqs. (2.2.26) and (2.2.22a).

2.3. Prototype Graphite-Epoxy/PCM Impregnated Graphite Foam 2d Box Structure Thermal Response

2.3.1. Prototype Characteristics

Figure 2.3.1 shows a 2D box structure that consists of paraffin-impregnated graphite foam (the TES-volume, Poco Graphite Inc.) reinforced with carbon/epoxy heat spreader plates and structural ribs (Hexcel Composites, W3T282-F155). The 2D Box structure is made of seven 5.6mm square cross section rods of graphite foam/paraffin. We measure the in-plane effective thermal conductivity of the graphite/paraffin/composite as ke_f = 50W/mK, so the graphite foam is a very effective thermal conductivity enhancer [Narla, 2003]. The mean cell size of the foam is 500μm; and, the porosity is approximately 0.75. The graphite foam was charged with 9.5 gm of n-docosane (T_{tr} = 43.9°C, k_p = 0.28 W/mK, hv = 189 joule/cc), so the volume fraction of n-docosane in foam is ε = 0.71.

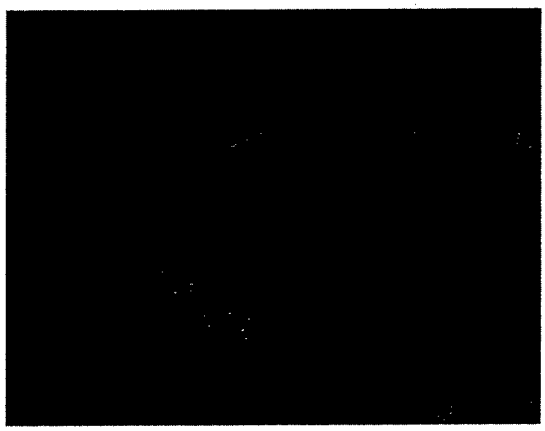

Fig.2.3.1 Graphite/Graphite Foam 2-D box composite.

Graphite-epoxy spreader plates and structural ribs are single ply, approximately 0.2mm thick. The measured in-plane, fiber axis direction effective thermal conductivity of the spreader

plates/structural ribs is 12 W/mK [Narla, 2003], so these components provide little heat spreader functionality.

A nitrogen-pressurized autoclave was used to cure the heat spreader plates/structural ribs and insure good contact to the TES volume. The cure cycle followed supplier specification. Paraffin fill was via a vacuum augmented surface tension driven process in an oven at 80°C.

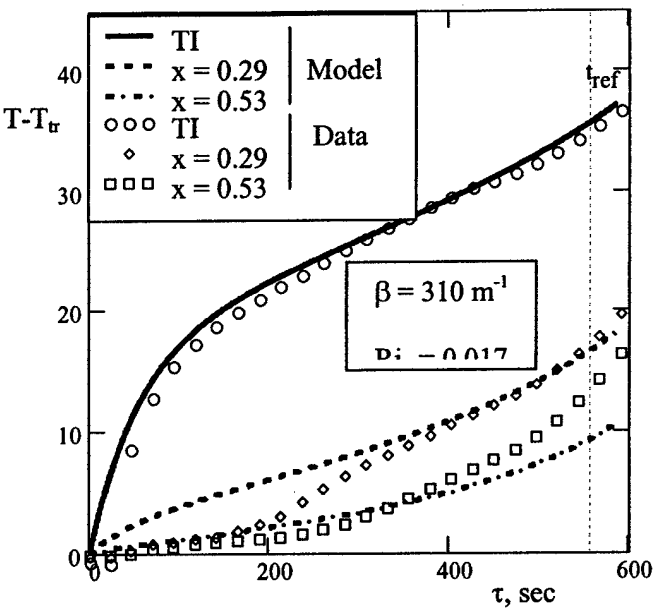

Fig. 2.3.2 Graphite foam prototype thermal response. Run 042403.

A 5.6 mm square by 39 mm long aluminum block with an imbedded cartridge heater and instrumented with 0.08 mm diameter type-T thermocouples served as the prototype's TI. This unit was clamped to the end of the Box prototype. (mc) of this unit is estimated as 0.56 joule/K.

The box structure was instrumented with a series of 0.08 mm diameter type-T thermocouples with junctions located along the centerline of the foam rods. Temperatures are monitored with a data logger having an accuracy of ±0.2°C. The voltage drop and electrical resistance across the TI cartridge heater is monitored with a DMM having a ±0.1% accuracy.

The test article is surrounded with rigid fiber insulation and placed in an oven, which is maintained at 43.5°C. When all temperatures are steady at 43.5°C, power is applied to the TI heater, and temperatures are recorded as a function of elapsed time.

2.3.2. Thermal Response Model Benchmark Experiments

Figure 2.3.2 shows the measured temperature response for a case where $q_l = 0.59$ watt (every 50-th data point is plotted). Also shown is the prediction of the model (Section 2.2.6). The figure shows that the predicted TI-temperature tracks the measurements quite well. Predicted heat spreader temperatures are generally higher than measurement since the thermocouples imbedded in the PCM/foam mass probably measure an average PCM/foam temperature, particurarly at early times when the PCM is still in solid phase. Later, these measurements converge when the PCM is in liquid phase.

Table 2.3.1 Run 042403 characteristics.

q_1, watt	ε	t_{ref}	T_{ref}, °C	$R_{k,t}$	hi Watt/mK	Ri_t
0.592	0.71	557	86.3	0.815	36000	0.017

Key characteristics of a typical experiment are summarized in Table 2.3.1.The TI-to-spreader (graphitic foam) interfacial conductance, hi is determined by extrapolating spreader temperature measurements at a particular time (say 400 sec) to x = 0, and then calculating the conductance as

$$hi = \frac{q_{tot}}{(1-\varepsilon)aW\left(T_{TI} - T_f\big|_{x=0}\right)} \tag{2.3.1}$$

We do not know a prioi the magnitudes of the specific surface area (β) or the foam-to-paraffin contact conductance. These quantities are adjusted to give the best fit of the model with data. We consistently find best fit values, $\beta \approx 300$ m^{-1} and $hi_p \approx 45{,}000$ watt/mK. This value of hi_p gives $Ri_p \approx 0.17$. The value of β obtained is roughly 30% of what would be expected. For example if the foam cell structure were a cubic array of interconnected 500 μm diameter spherical cells with about 2/3rds of each cell an open interconnect with an adjacent cell, we would expect $\beta = 1150$ m^{-1}. Apparently, the reduced effective contact area ($\beta = 310$ m^{-1}) is due to the approximate 13% specific volume change that accompanies solid-liquid phase transition of paraffin. Graphitic foam is filled with liquid-phase paraffin. Upon cooling and solidifying, particles of paraffin shrink and pull away from the graphite cell walls so that only approximately 30% of the surface of each paraffin particle is in direct contact with its containing cell wall.

2.4. Thermal Response Model – Disk TES-Volumes

2.4.1. Simple 1-D Sandwich Structures

An operable unit cell for analysis of the configuration shown in Fig. 2.1.2 (Section 2.1) consists of a square plan-form section of a single laminate, of edge length 2P with the aluminum plate (thickness t_f) bounding one side of a TES-volume (PCM-composite) of thickness t_p, as shown in Fig. 2.4.1. The TI is located at the geometric center of the plan form. All external surfaces of this unit cell, except the exposed surface of the TI, are

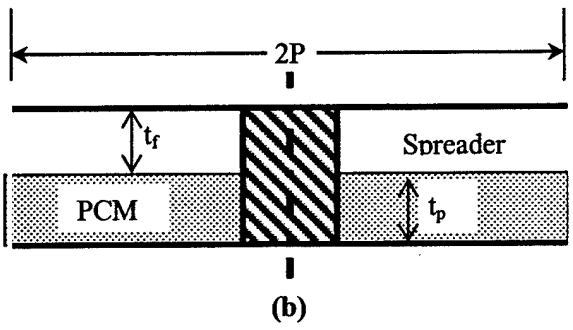

Fig. 2.4.1 Section edge viewof TI/TES volume

adiabatic. The in-plane radial conductance of the spreader plate is large, whereas that for the storage volume is small. Consequently, radial conduction from the TI is primarily via the spreader plate, into the PCM-composite.

We transform this square plan form shape into the composite cylinder shown in Fig. 2.4.2. The transformed unit cell consists of the following elements:

- A centrally located TI element of radius r_o,
- An annular disk aluminum fin of thickness t_f, and outer radius $r_e = \sqrt{\frac{4}{\pi}}P$, and thermal conductivity k_f, and
- An annular disk of PCM-composite having thickness t_p, effective thermal conductivity k_p, and volumetric latent heat h_v.

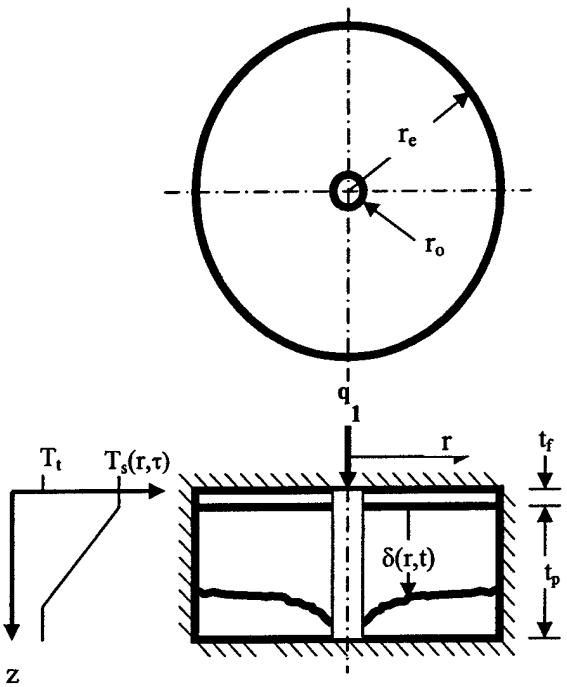

Fig. 2.4.2 Transformed unit cell.

The heat input rate to the TI is

$$q_1(\tau) = q_{ref} F(\tau) \tag{2.4.1}$$

where q_{ref} is a reference quantity. The temperature of the fin material is T_f and that of the TES-volume is T_p. Our physical model has heat conducted from the TI radially outward along the spreader plate, and then to the PCM-composite. The spreader plate has thickness t_f and that of PCM-composite is t_p. The figure shows the structure at some time, τ during the heat storage mode with a phase transition interface in the storage volume moving radially outward and downward. PCM below the phase transition boundary is in solid phase at the phase transition temperature T_t, and PCM above the phase transition boundary is in the liquid phase at $T_p > T_t$.

Make the following assumptions:

1. Heat flow in the fin is one-dimensional transient (r-direction); heat flow in the paraffin-disk is one-dimensional transient (z-direction).
2. The sensible heat capacity of the fin and PCM-disk is negligible compared to the latent heat capacity of the paraffin-disk. Note, we can incorporate the spreader plate/PCM sensible heat effect into the sensible heat of the TI.

Following the procedure outlined in Section 2.2, energy balances on the TI, TI-to-spreader plate interface, spreader plate and melt region of the PCM and liquid-solid phase transition interface give the following equations:

$$MC\frac{d\overline{\mathrm{T}}_{TI}}{d\bar{\tau}} = [F(\bar{\tau}) - \bar{q}_{f,o}] \tag{2.4.2}$$

$$\bar{q}_{f,o} = R_k(\overline{\mathrm{T}}_{TI} - \overline{\mathrm{T}}_{f,o})/Ri \tag{2.4.3}$$

$$\frac{\partial\bar{r}\dfrac{\partial\overline{T}_f}{\partial\bar{r}}}{\partial\bar{r}} - K^2(\bar{\tau})\bar{r}\overline{T}_f = 0 \qquad \overline{T}_f(\bar{r}_o,\bar{\tau}) = \overline{T}_{f,0} \qquad \left.\frac{d\overline{T}_f}{d\bar{r}}\right|_{r_e} = 0 \tag{2.4.4a,b}$$

with

$$K(\bar{\tau}) = \sqrt{\frac{1}{Rk\bar{\delta}(\bar{\tau})}} \tag{2.4.4c}$$

$$\frac{\partial\bar{\delta}}{\partial\bar{\tau}} = A\frac{\overline{T}_f}{\bar{\delta}} \tag{2.4.5}$$

where

$$\bar{q} = \frac{q}{q_{ref}} \qquad \bar{\tau} = \frac{\tau}{\tau_{ref}} \qquad \bar{\delta} = \frac{\delta}{t_p} \qquad \bar{r} = \frac{r}{r_e} \qquad \overline{T} = \frac{T}{T_{ref}} \tag{2.4.6}$$

and

$$\tau_{ref} = \frac{h_v V_p t_p}{q_{ref}} \qquad T_{ref} = \frac{q_{ref}}{k_p \cdot t_p} \tag{2.4.7}$$

The dimensionless parameters:

$$MC = \frac{(mc)_{TI}\,q_{ref}}{k_p h_v r_e V_p} \qquad Rk = \frac{k_f t_f t_p}{k_p r_e^2} \qquad Ri = \frac{k_f}{h_i r_e} \qquad A = \frac{V_p}{r_e t_p^2} \tag{2.4.8a,b,c}$$

describe the transient response of the system.

2.4.2. *Uniform Delta Solution*

Wirtz et al.[2003b] show that when $k_p << k_f$ and $t_p << r_e$, except near the TI, the phase transition interface will be a nearly horizontal plane and $\delta(r,\tau) \approx \delta(\tau)$ only. Then, Eqs. (4) may be integrated to give

$$\overline{T}_f(\bar{r},\bar{\tau}) = \overline{T}_{t,0}(\bar{\tau})\theta(\bar{r},\bar{\tau}) \tag{2.4.9}$$

$$\theta(\bar{r},\bar{\tau}) = C_1(\bar{\tau})I_O[\overline{K}(\bar{\tau})\bar{r}] + C_2(\bar{\tau})K_O[\overline{K}(\bar{\tau})\bar{r}] \tag{2.4.10}$$

$$C_1(\bar{\tau}) = \frac{K_1(\overline{K}(\bar{\tau})\cdot\bar{r}_e)}{D(\bar{\tau})} \qquad C_2(\bar{\tau}) = \frac{I_1(\overline{K}(\bar{\tau})\cdot\bar{r}_e)}{D(\bar{\tau})} \tag{2.4.11}$$

$$D(\bar{\tau}) = I_0[\overline{K}(\bar{\tau})\bar{r}_o]K_1[\overline{K}(\bar{\tau})] + I_1[\overline{K}(\bar{\tau})]K_0[\overline{K}(\bar{\tau})] \tag{2.4.12}$$

$$\overline{q}_{f,0}(\bar{\tau}) = R_k Q(\bar{\delta})\overline{T}_{f,0} \tag{2.4.13}$$

$$Q(\bar{\tau}) = -\{\overline{K}(\bar{\tau})\{C_1(\bar{\tau})I_1[\overline{K}(\bar{\tau})\bar{r}_o] - C_2(\bar{\tau})K_1[\overline{K}(\bar{\tau})\cdot\bar{r}_o\} \tag{2.4.14}$$

where I_0, K_0 and I_1, K_1 are modified Bessel functions of the first and second kind.

The average heat flux into the storage volume is $q_p'' = q_l/A_c$, so Eq (4) can be rewritten as

$\frac{d\bar{\delta}}{d\bar{\tau}} = F(\bar{\tau})$ and integrated to give the average penetration depth

$$\delta(\bar{\tau}) = \int_0^{\bar{\tau}} F(\bar{\tau})d\bar{\tau} \tag{2.4.15}$$

Equations (2, 3, and 13) can be rearranged to give

$$\overline{T}_{f,0} = \frac{\overline{T}_{TI}}{1 + RiQ(\bar{\tau})} \tag{2.4.16}$$

$$\frac{d\overline{T}_{TI}}{d\tau} = \frac{1}{MC}\left\{F(\tau) + \frac{R_k Q(\bar{\tau})\overline{T}_{TI}}{1 + RiQ(\bar{\tau})}\right\} \tag{2.4.17}$$

Equations (2.4.15 - 17) together with Eqs (2.4.7, 8) are three parameters plus time and temperature scales which describe the system.

2.4.3. *Negligible TI Mass And TI-To-Spreader Interfacial Resistance*

Metal-based systems will have the TI brazed to the spreader plate; and it is likely that the TI mass will be negligible. Under these conditions (MC = Ri = 0), $\overline{q}_{f,0} = \overline{q}_1$ and $\overline{T}_{TI} = \overline{T}_{f,0}$. Then, from Eq. (2.4.16)

$$\overline{T}_{TI} = \frac{F(\overline{\tau})}{R_k Q[\overline{K}]} \tag{2.4.18}$$

Wirtz et al [2003b] developed and benchmarked this solution in their study of metal/PCM composites. One important aspect of the solution (shown in Fig. 2.4.3) is the profound effect that the TI size has on the heat transfer to the TES-volume. The figure plots the dimensionless spreader plate temperature distribution for three TI sizes. The figure shows that the smaller TI, with small peripheral surface area, gives rise to large temperature gradients at the TI-to-spreader interface, resulting a significant radial temperature variation and reduced heat transfer of the TES-volume. Increased in r_o ameliorate this problem. However the trade off is a reduction in storage capacity.

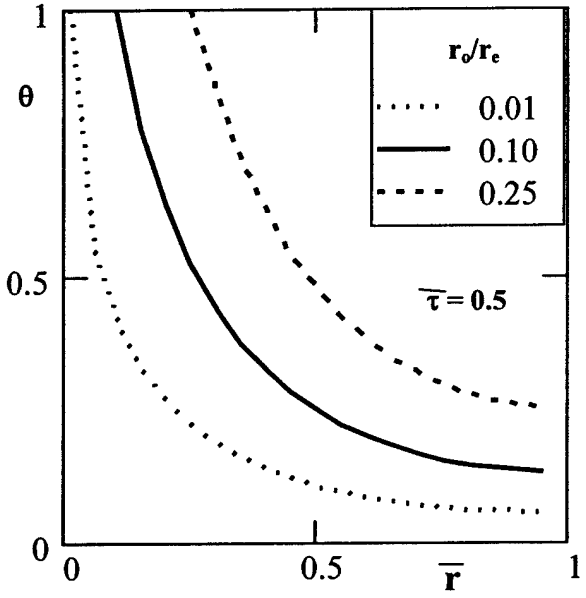

Fig 2.4.3 Effect of TI size on spreader temperature distribution

2.5. Thermal Conductivity Enhanced 1-D Structures – Sub-Laminate Response Model

The TES-volume consists of PCM imbedded in an open cell conductive foam. The foam acts as a thermal conductivity enhancer and immobilizer to inhibit liquid-phase paraffin motion. The TES-volume is contained between rigid plates, which provide structural functionality, but we assume they are thin, and have a relatively low thermal conductivity so that they do not participate in the heat transfer process.

An operable unit cell for analysis of the configuration is shown in Fig. 2.5.1a. It consists of a centrally located TI in thermal contact with a

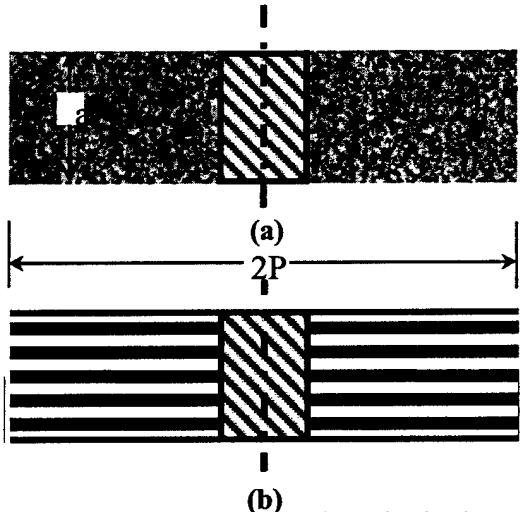

Fig 2.5.1 Section edge-view of TI/TES-volume.

PCM impregnated, conductive foam disk of radius $r_e = \sqrt{\frac{4}{\pi}}P$. In storage mode, heat flows into the thermal interface, and then radially outward from the TI through the conductive graphitic foam filaments to the paraffin particles imbedded in the foam. In the heat release mode of operation, stored energy flows back to the TI, and then to the heat sink of the system. The volume of foam is

$$V_f = A_c a\,, \tag{2.5.1}$$

while that of the paraffin embedded in the foam is

$$V_p = \varepsilon_f A_c a \tag{2.5.2}$$

where $A_c = 4P^2 - \pi r_o^{\,2}$ is the plan area of the TES-volume, and ε_f is the *effective* porosity of the porous foam (not all foam pores are filled with paraffin). In addition, the foam-to-paraffin contact area is

$$A_{fp} = \beta_f A_c a \tag{2.5.3}$$

where β_f is the effective specific surface area of the foam.

Figure 3b shows an equivalent view consisting of stacked radial graphitic fins of thickness $2t_f$ interspersed with disks of paraffin of thickness, $2t_p$. In this case, the foam-to-paraffin contact area is

$$A_{fp}(equiv.) = nA_c \tag{2.5.4}$$

where n is the number of sub-laminations (thickness t_f+t_p). For the two systems to be equivalent, $A_{fp}(equiv.) = A_{fp}$, so the number of sub-laminations is

$$n = \beta_f a \tag{2.5.5}$$

The thickness of each component of each sub-laminate is

$$t_f = \frac{a}{n} = \beta_f^{-1} \text{ and } \qquad t_p = \frac{\varepsilon_f a}{n} = \frac{\varepsilon_f}{\beta_f} \tag{2.5.6}$$

Then, the disk-laminate model of Section 2.4.1 Eqs. (2.4.15 – 2.4.17) can be used to predict system thermal response, where

$$V_{p,sub} = \frac{\varepsilon Ac}{\beta}, \tau_{ref} = \frac{\varepsilon h_v Ac}{\beta_f q_{ref}}, T_{ref} = \frac{q_{ref}}{\varepsilon k_p} \tag{2.5.7}$$

$$MC_{sub} = \frac{mc \cdot q_{ref}}{\varepsilon\beta k_p h_v a^2 r_e Ac}, \qquad R_{k,sub} = \frac{\varepsilon k e_f}{\beta^2 k_p r_e^{\,2}}, \qquad Ri_{tube} = \frac{\varepsilon}{1-\varepsilon}\frac{ke_f}{(\beta a)h_i r_e} \tag{2.5.8}$$

The magnitude of the specific surface area of the foam conductivity enhancer (β_f) has a strong effect on the temperature response of the system. This is shown in Fig. 2.5.2 where the TI-temperature excursion of a fictitious TES-system is shown to be roughly proportional to β_f^{-1}.

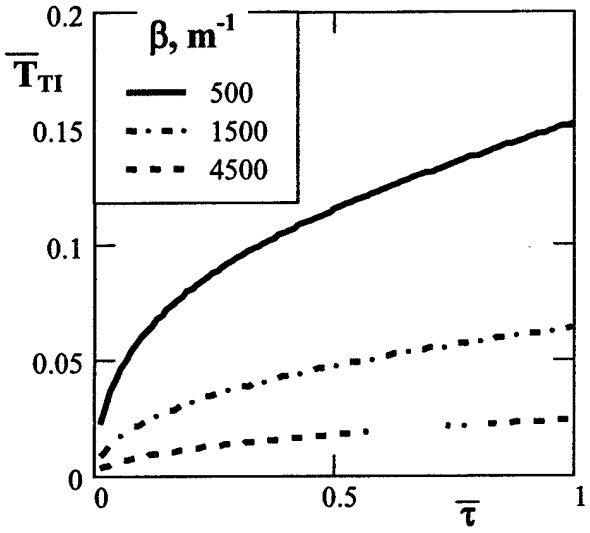

Fig 2.5.2 Effect of β-variation on TI-temperature response.

2.5.1. Graphite Foam/Parrafin Benchmark Experiments

Benchmark experiments were performed to test the accuracy of the above-described analytical model. The test article consists of a 101 mm diameter x 14.1 mm thick (r_e = 50.5 mm, a = 14.1 mm) docosane impregnated disc of graphitic foam having an average density of 0.71 gm/cm^3 and effective thermal conductivity of 50.2 watt/mK. A 28 mm diameter aluminum cylindrical TI, with small cartridge heater, was interference fit at the center of the foam disk. The disk was loaded with 38.6 gm of docosane (T_t = 43.9°C, h = 242 j/gm, ρ = 0.778 gm/cc), so that ε_f = 0.47. Type T thermocouples monitor the TI temperature and the mid-plane TES-volume temperature at r = 25.4 mm and 38.1 mm (two T.C's at each location). Temperatures are monitored with a data logger having an accuracy of ±0.2°C. The voltage drop and electrical resistance across the TI cartridge heater is monitored with a DMM having a ±0.1% accuracy.

The test article is surrounded with rigid fiber insulation and placed in an oven, which is maintained at 43.5°C. When all temperatures are steady at 43.5°C, power is applied to the TI heater, and temperatures are recorded as a function of elapsed time. Figure 2.5.3 plots the temperature response of the test article for an experiment where the heat input rate is q_n = 27 watts. Open symbols are every 40-th recording of the TI temperature (circles) and the two mid-plane TES-volume temperatures at r = 25.4 mm and 38.1 mm (squares and diamonds,

respectively). The solid line is the predicted TI temperature response (Eq. 2.4.18). The dashed lines are predicted foam temperatures at r = 25.4 mm and 38.1 mm. The measured foam temperatures are lower than the corresponding analytical prediction (dashed lines) since the thermocouples measure an average temperature of the foam and paraffin, whereas the model predicts only the foam temperature.

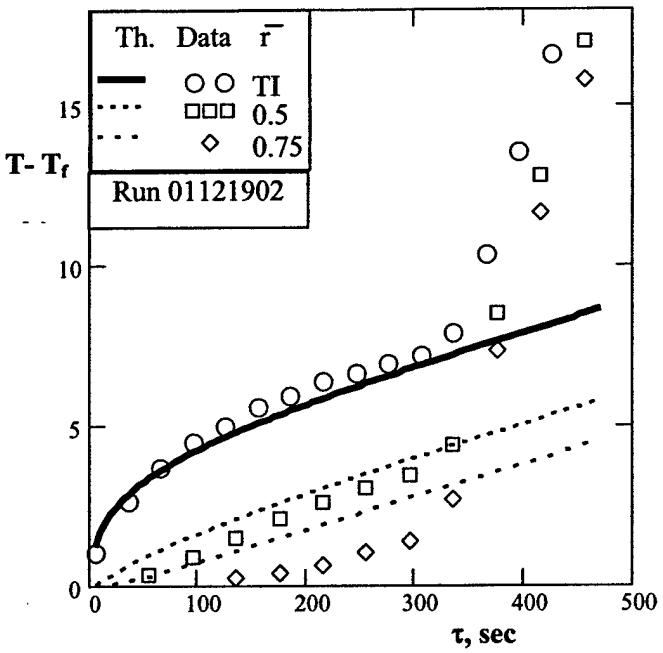

Fig 2.5.3 prototype graphite foam disk temperature response

The effective foam-to-paraffin contact area (β_f) is not known a priori. Its value is selected to give the best fit of the TI temperature response data shown in Fig 2.5.3. A value, $\beta_f = 310\ m^{-1}$ appears to work best, resulting in a final TI temperature rise of $\Delta T_{TI} = 8.6°C$ at $\tau_{ref} = 470$ sec. The "best fit" value of β_f is approximately three times smaller than expected.

As discussed in Section 2.3, we believe the reduced effective contact area ($\beta_f = 310\ m^{-1}$) is due to the approximate 13% specific volume change that accompanies solid-liquid phase transition of paraffin. Graphitic foam is filled with liquid-phase paraffin. Upon cooling and solidifying, particles of paraffin shrink and pull away from the graphite cell walls so that only approximately 10% - 15% of the surface of each paraffin particle is in direct contact with its containing cell wall. In support of this argument, it is noted that the graphitic foam used in the benchmark experiments has a nominal porosity of approximately 73% while when fully charged with docosane, weight measurements indicate the volume fraction of paraffin is $\varepsilon_f = 0.61$. The difference (0.73 – 0.61 = 0.12) accounts for this shrinkage. Therefore, while the foam graphite matrix can accommodate the specific volume change that accompanies phase transition without fracture, it does so at the cost of a reduced ability to maintain the TI at a nearly constant temperature.

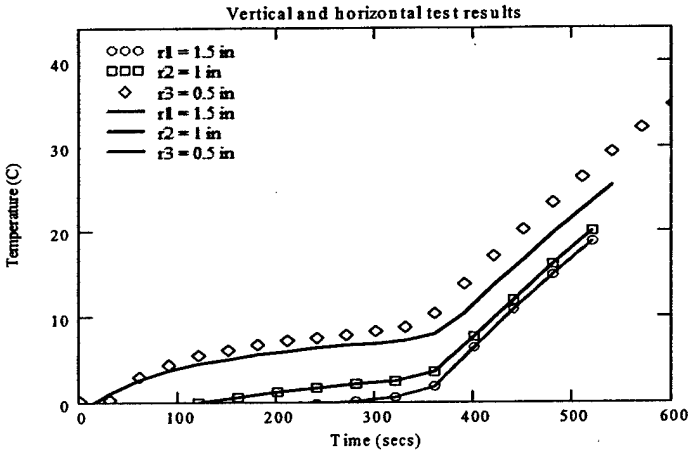

Fig 2.5.4: Liquid paraffin immobilization test results.

The test article has $t_{ref} = 435\text{sec}$ while the data of Fig 2.5.3 indicate that the heat storage process is essentially over at about 350 sec. Small spherical paraffin particles near the end of the melt process are effectively insulated from the conductive foam by a layer of immobile liquid paraffin (k_p = 0.26 watt/mK) giving rise to reduces storage effectiveness and more rapid rate of temperature increase. The present layered model apparently does not capture this effect.

2.5.2. Paraffin Immobilization

Consider a d_p = 250 μm diameter solid paraffin particle that is melting inside a d_f = 500 μm diameter cell. A 125 μm thick layer of liquid paraffin surrounds the solid particle. Assume a ΔT_{fp} = 5°C temperature difference between the cell wall and the paraffin particle. The natural convection Rayleigh number is

$$Ra = \frac{g \cdot C_{TE} \cdot \Delta T}{\nu_p \lambda_p} \left(\frac{d_f - d_p}{2} \right)^3 = 0.12g \tag{2.5.9}$$

where $\nu_p = 4x10^{-6}\ m^2/sec$, $\lambda_p = 1.4x10^{-7}\ m^2/sec$ and $C_{TE} = 0.9x10^{-3}\ K^{-1}$ are the kinematic viscosity, thermal diffusivity and coefficient of thermal expansion of paraffin, respectively. Thus, at 10g, the Rayleigh number is O(1), and convection effects are negligible. We tested this idea (at 1g) by repeating the benchmark experiments described above with the test article in different orientations with no discernable difference in the recorded temperature data. Fig. 2.5.4 shows the temperature response of the graphite disk test article which was oriented in the horizontal and vertical direction. The solid lines show the temperature response when the test article was in horizontal position. The plotted symbols show the temperature response when the article was kept vertical. The PCM temperatures near the TI for the horizontal orientation are about 1°C - 2°C

lower than those of the vertical orientation. Points further removed from the TI show no discernable difference in temperature

2.6. Conclusions

TES-System Thermal Response Simple semi-empirical models that predict the thermal response of plate-like TES-structures have been developed. The models include the three essential features of such devices: 1) the thermal interface to the heat source/sink of the electronics (TI); 2) a heat spreading component such as a conductive plate or foam, that addresses the generally poor thermal conductivity of most phase change materials; and, 3) the thermal storage volume, which includes the PCM plus ancillary materials such as a conductivity enhancer or liquid immobilizer. In addition to the latent heat component of such a system, the models capture specific design attributes such as detail component dimensions, component masses and inter-component interfacial thermal resistances. The models do not require recourse to FE/FD application packages.

A variety of TES-system configurations have been considered, ranging from simple laminations to fairly complex systems that include additional elements for improved structural performance (2D box and Lattice sub-structures). Two design philosophies have been addressed: 1) mm-scale metallic structures that encapsulate the PCM and ancillaries, and 2) carbon composite structures that encapsulate PCM impregnated graphite foam, which serves to promote heat transfer and immobilize liquid-phase PCM. In addition, two approaches to thermal interfacing the TES-system to the electronics have been considered: a) a matrix of point inputs that results in radial heat flow to/from the TES-volume, and b) line inputs that result in rectilinear heat flow.

Experiments with graphite-epoxy/paraffin impregnated graphite foam prototypes are used to assess the thermal performance models and effectiveness of the various design approaches. The models are found to capture essential characteristics of the transient response of the systems considered. One finding of particular significance is that the effective specific surface area of the graphite foam used in the benchmark experiments is approximately 3-fold smaller than originally anticipated. This leads to an approximate 3-fold increase in the ultimate temperature excursion of the system TI, so the effective specific surface area of the foam component, together with the associated foam-to-paraffin-particle contact conductance are important design attributes for effective thermal control with these non-metallic systems. Furthermore, the thin high-conductivity graphite-epoxy encapsulation does not effectively participate in the heat storage process, so more conventional non-metallic structural elements could be considered without any significant degradation in thermal performance.

A design study of alternative micro-channel aluminum plate/paraffin TES-structures finds that from a thermal perspective; simple laminations, and more complex 2D Box and Lattice substructures give essentially equivalent thermal performance. Furthermore, aluminum based systems appear to give thermal response performance that is a least equivalent to the more complex graphite foam systems.

3. TES-System Structural Response

3.1. Specimen Preparation

Tension, compression, and bending specimens were prepared for the study of the mechanical properties of the carbon/graphite TES-composites, screen laminate TES-composites, and the aluminum meso-channel structures. The specimen designs followed the ASTM standards (2001).

3.1.1. Carbon/Graphite TES-composites Specimens

The carbon/graphite TES-composites are constructed by two elements: a porous graphitic core impregnated with the PCM and the graphite/epoxy composite skins. The porous graphitic core is conductive, and it possesses a large specific surface area, which facilitates heat input to the PCM. The graphite/epoxy skin was cured from plain weave carbon prepreg marketed by Hexcel Composites (2002) and the graphitic foams were derived from the naphthalene based synthetic pitch and marketed by Poco Graphite, Inc. (2002). Depending on the locations where the sample was cut from the supplied block of material, the graphitic foam density varied from 0.25 to 0.61 g/cm3. This corresponded to a porosity ranging from 72% to 89%. The PCM used in this study is BW-422 paraffin marketed by Blended Waxes Inc. (2002). The paraffin has a density of 0.80 g/cc, a latent heat of 195 J/g, and melts at 55°C.

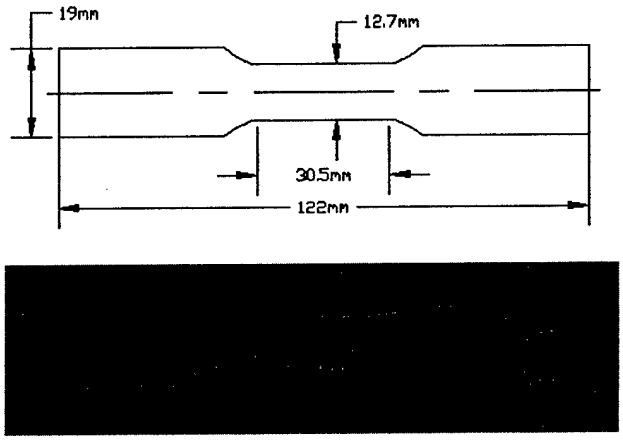

Fig. 3.1.1 Graphite TES composite tension specimen

The skin tension specimens, the tension and compression specimens of empty graphitic foam, and the tension and compression specimens of the graphitic foam filled with PCM were prepared for the corresponding experiments. Tension specimens were cut into dog-bone shape (Fig. 3.1.1). The tension specimens are 122 mm long, 19 mm wide and 6.4 mm thick. The width of the gage section is 12.7 mm, and the length of the gage section is 30.5 mm. The compression specimens have a dimension of 25.4mm×12.7 mm×12.7 mm (Fig. 3.1.2).

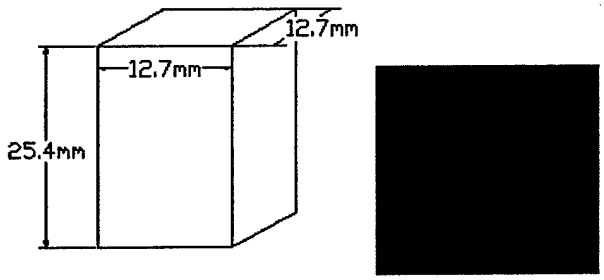

Fig. 3.1.2 Graphite TES composite compression specimen

An one-dimensional (1D) sandwich structure, as shown in Fig. 3.1.3, was fabricated and investigated first. The sandwich structure was formed by the lamination that consisted of a PCM impregnated porous graphitic core encapsulated between graphite/epoxy composite skins (Fig. 3.1. 4). The dimension of the structure is 130mm × 19mm × 6.4mm. The sandwich structure is considered one dimensional since the materials of the composite are stacked in one dimension and the heat is transferred from the skins to the core material one dimensionally.

A two-dimensional (2D) box structure (Fig. 3. 1.5) was designed as a precursor to fabrication and analysis of the three-dimensional structure. The 2D box structure used in this study is made of seven 6.5mm cross section rods of graphitic foam with epoxy skin between them, as shown in Fig 3. 1. 6. The length of the structure is 89 mm. TES volume is the graphite foam impregnated with the PCM. The plate and the ribs are made of graphite/epoxy skins. The box structure is referred to as two dimensional. As shown in Fig. 3. 1.5, both of the plates and the structural ribs spread heat into the TES volume. Heat is transferred to the TES volumes two dimensionally.

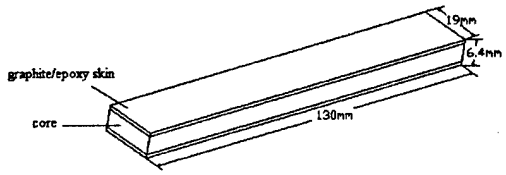

Fig. 3.1.3 1D sandwich structure

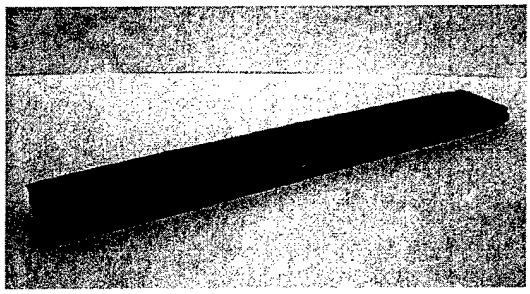

Fig. 3.1.4 Graphite TES composite 1D sandwich structure bending specimen

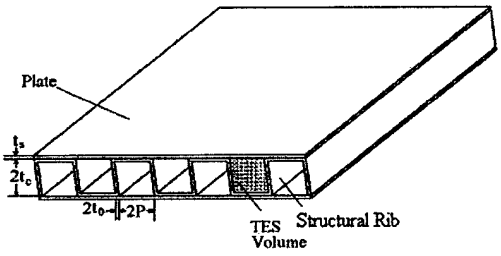

Fig. 3.1.5 2D box structure

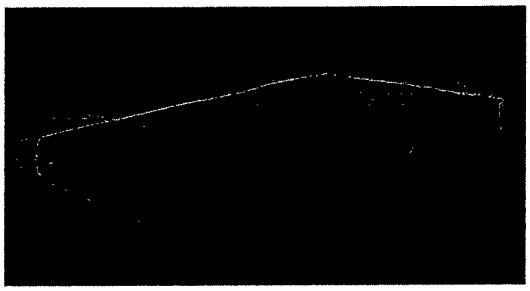

Fig. 3.1.6 2D box graphite TES composite

3.1.2. Screen Laminate TES-Composites Specimens

Copper screens served as structural components in the screen laminate TES-composites. They were plain weave copper mesh marketed by Howard Wire Cloth Co. (2002). Screens are generally specified by manufactures in terms of wire diameter and mesh number. The mesh number is defined as the number of openings per inch. The copper screen used in this work has a

wire diameter of 0.457 mm (0.018") and a mesh number of 16. The copper screen has joints contacted but not welded. Therefore, the copper screen was brazed so that the joints of the wires were brazed together to make the structure stronger and stiffer.

Brazing

Brazing is a method to permanently join a range of materials and has wide applications in fabricating components. It is distinguished from welding in that the process takes place at temperatures below the melting points of the materials being joined. Brazing is different from soldering in temperature used in the process. Processing above 450°C is classified as brazing and processing below 450°C is classified as soldering. One significant attribute of brazing is that the brazing process has the ability to join porous material.

BRAZE 720 containing 72% silver and 28% copper was chosen as the filler metal. First of all, the melting point of BRAZE 720 is 779°C, which is lower than that of copper (1083°C). Secondly, the filler metal is in a eutectic form at 779°C. Its constituents will not be separated. In addition, BRAZE 720 has a flux in it which helps to wet the surfaces of the copper screen and no constituent reacts with the copper screen during the brazing process. The paste form was chosen considering the complicated surface of the plain weave screen. BRAZE 720 paste was pasted on the screens with a brush. The flux melts at 500°C. The flux wets the surface of the copper screen first and then the brazing alloy flows into the joint by capillary action.

Several heating methods such as torch brazing, furnace brazing, induction brazing, and dip brazing are often used. In this work, furnace brazing was chosen as the heating method. In a furnace, specimens to be brazed can be preassembled in the correct position. The whole specimen can be heated uniformly in the furnace. Multiple joints of the copper screen specimen can be brazed simultaneously and identically.

Retort Design

Since silver in BRAZE 720 is easily oxidized in the air, specimens must be brazed in an inert-gas protecting environment. Nitrogen was used to protect the brazing process. After several specimen fabrication failures with a big retort coming with the furnace, a smaller retort was designed and manufactured for the current research.

Figure 3.1.7 shows the design of the inert gas protection retort. The overall dimension of the retort is 76.2 mm × 76.2 mm × 254 mm. The retort is made of stainless steel. It has an inlet, a base chamber at the bottom, a chamber, three outlets on the top, and a door. The bottom of the base chamber is tapered and there are 45 small holes distributed evenly at the bottom of the body.

During brazing, the gas comes in from the inlet into the base chamber. The tapered base chamber and small holes at the bottom of the body facilitate the distribution of the gas. The circulated gas goes out of the retort from the outlets on the top. To monitor the temperature inside the retort, thermocouples were inserted into the retort through the outlets.

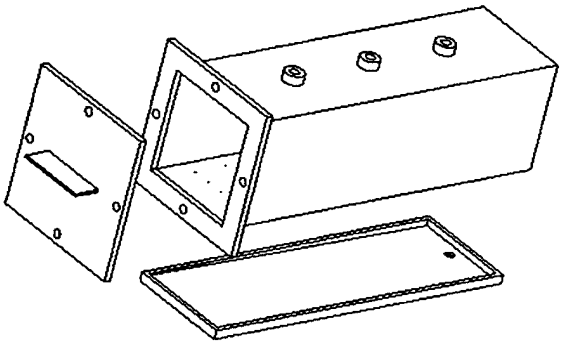

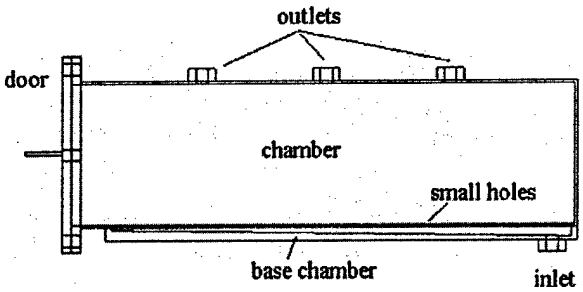

Fig. 3.1.7 Retort for copper screen brazing

Procedure to Braze Screen Specimens

The brazing procedure consists of four basic steps: cleansing, assembly, brazing, and cleaning up. Capillary action works properly only when the surfaces of the metals are clean. Oil, grease, and plain dirt should be removed. Copper screen laminates were cleaned lamina by lamina with acetone.

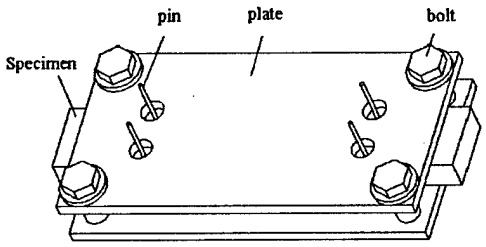

Fig. 3.1.8 Fixture for brazing screen laminates

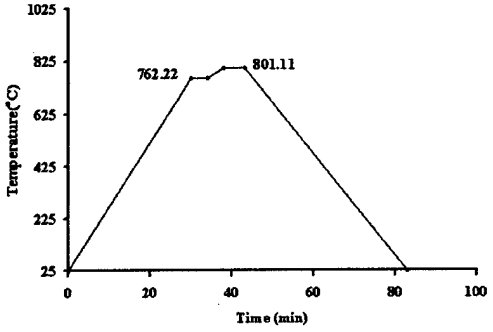

Fig. 3.1.9 Heating cycle for copper screen brazing

The lamina of the copper screen laminates were cleaned and pasted with BRAZE 720. A fixture was used to hold the lamina in position for brazing. As shown in Fig. 3.1.8, the fixture consists of two identical stainless steel plates. There are four bolts at the corners that join the two plates together. The four holes in the middle are for the pins to go through to line up the laminate. For tension specimens, pieces of copper screen were placed directly in the retort. Mold release material (Boron nitride) was sprayed between the specimens and the stainless steel plates to facilitate the release of the specimens after brazing.

The third step is the actual accomplishment of brazing the joints. The retort was installed inside the furnace. Nitrogen gas was provided at a flow rate of 2.0 LPM. Figure 3.1.9 shows the heating cycle during brazing. The temperature inside the retort was heated up to 762°C within half an hour. To make the temperature uniform, the furnace soaked at 762°C for four minutes. In the next four minutes, the temperature was raised to 801°C and stayed at this temperature for another four minutes during which the eutectic form of the filler metal was created. Once the eutectic form had been created, the temperature needed to be brought down as soon as possible so that the constituents of the alloy would not be separated at the high temperature. The valve for nitrogen gas was opened widely and the furnace door was opened to cool down the furnace temperature. After about 40 minutes, the furnace temperature would be cooled down to 400°C. Since no gas protection was needed at this temperature, the gas valve was closed. The furnace temperature went back to room temperature in approximately two hours.

Flux residues left on the specimen must be removed after brazing. Flux residues are chemically corrosive and, if not removed, could weaken certain joints and would affect the heat transfer performance of the copper screen. Since the brazing flux is water soluble, the specimen was quenched in an ultra-sonic cleaning tank filled with hot water (50°C or hotter).

Specimen Configuration

One layer of the copper screen was brazed and copper strips were brazed at both ends of the tension specimen. The copper strip ends are used for griping the specimen during the tension experiment. The size of the one-layer copper screen is 25.4mm wide and 102mm long.

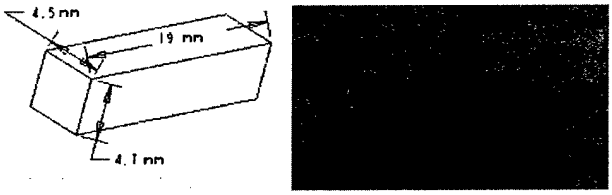

Fig. 3.1.10 Copper screen compression specimen

Figure 3.1.10 shows the specimen for compression experiment. Copper screens were lined up together and brazed to a copper mesh block. A short specimen is needed for compression experiments in order to avoid buckling under compression. The copper mesh block was cut into small blocks and the upper and lower sides of the blocks were polished to make the two sides flat and parallel. The compression specimens are 19mm long, 4.5mm wide and 4.7mm in depth.

A bending specimen is shown in Fig. 3.1.11. Copper screens were lined up and brazed to copper screen laminates. The bending specimen is 102mm long and 19mm wide. Specimens are laminates of $[0°_5]$, $[0°_7]$, $[0°_9]$, $[45°_5]$ and [0°/45°/0°/45°/0°]. The laminate $[0°_5]$, $[0°_7]$, and $[0°_9]$ are respectively five, seven, and nine layers of copper screen layered up at zero degree, and the laminate [0°/45°/0°/45°/0°] has five layers and has the stacking sequence of 0°, 45°, 0°, 45° and 0°. 0° denotes that the laminae are oriented with principal material directions at zero degree angle to the global laminate axes and the 45° denotes that the principal material directions is at 45 degree to the global laminate axes (Fig.3.1.12).

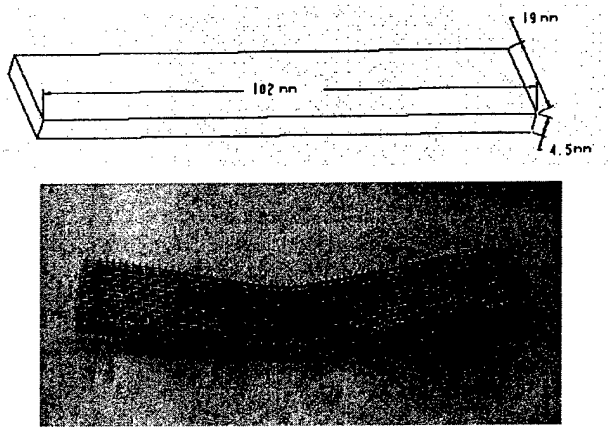

Fig. 3.1.11 Bending specimen of copper screen laminates

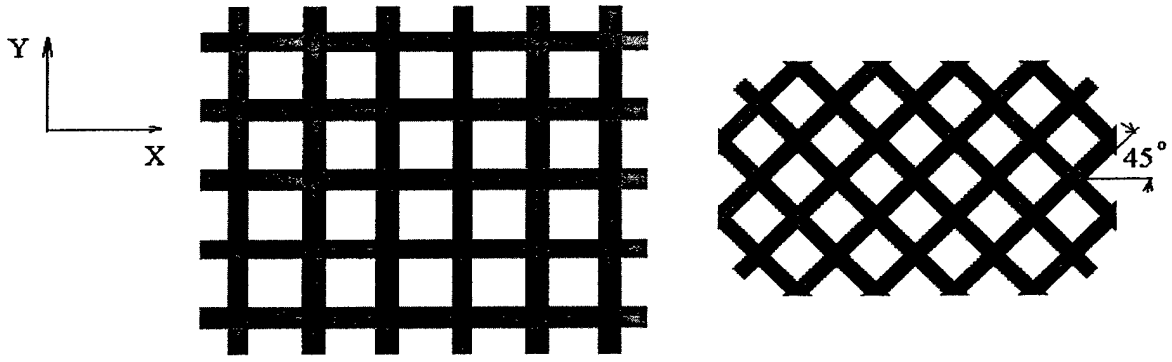

zero degree copper screen

45 degree copper screen

Fig. 3.1.12 Zero degree copper screen and 45 degree copper screen

3.1.3. Aluminum Meso-Channel Structures

Two kinds of aluminum TES-Composites as shown in Fig.3.1.13 were investigated. The cross sections of the structures were measured under microscope. Figure 3.1.14 shows the unit cell dimensions of the structures. Aluminum Structure I, provided by Hydro Alunova Inc. (2003), has a porosity of 67.0% and a surface to volume ratio of 1296.7/m. Aluminum Structure II, provided by Thermalex Inc.(2003), has a porosity of 50.22% and a surface to volume ratio of 2632.71/m.

Aluminum Structure I has a higher porosity while Aluminum Structure II has a higher surface to volume ratio.

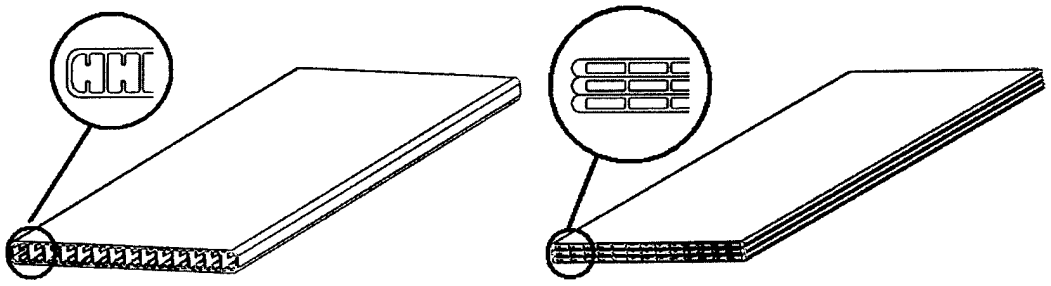

(a) Aluminum Structure I (b) Aluminum Structure II

Fig. 3.1.13 Aluminum meso-channel structures

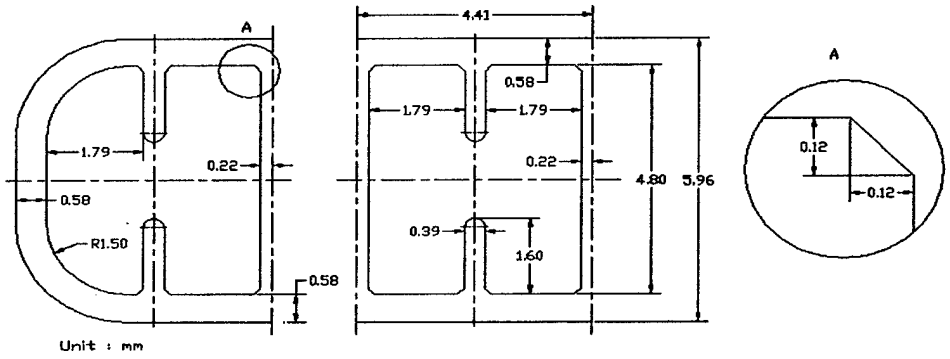

(a) Aluminum Structure I

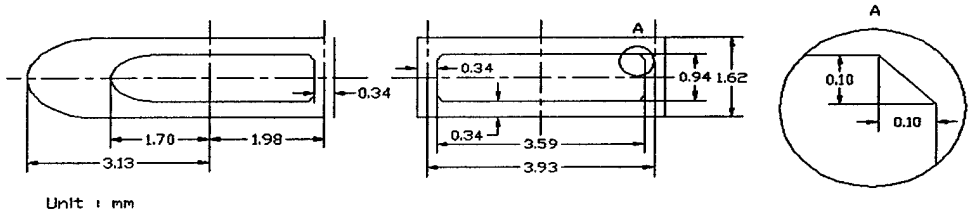

(b) Aluminum Structure II

Fig. 3.1.14 Dimensions of aluminum structures

Figure 3.1.15 shows the tension specimens of the aluminum meso-channel structures. For structure I, pieces of aluminum skin were cut from the structure and were made into a dog-bone shape. The gage length was 30.48mm and the gage width was 12.7mm. For structure II, the tension specimens were made from one layer of the aluminum structure having a gage width of 15.875mm and gage length of 35.56mm.

The bending specimens of structure I were one layer of the aluminum skin structure as shown in Fig.3.1.13 (a). The bending specimens of Aluminum Structure I are 177.8 mm long, 58.3 mm wide, and 5.96 mm thick. Three layers of Aluminum Structure II were laminated together very carefully using H3151 structural adhesive manufactured by LOCTITE to make bending specimens as shown in Fig.3.1.13 (b). The specimens of structure II are 146.05mm long, 53.43mm wide, and 2.77 mm thick.

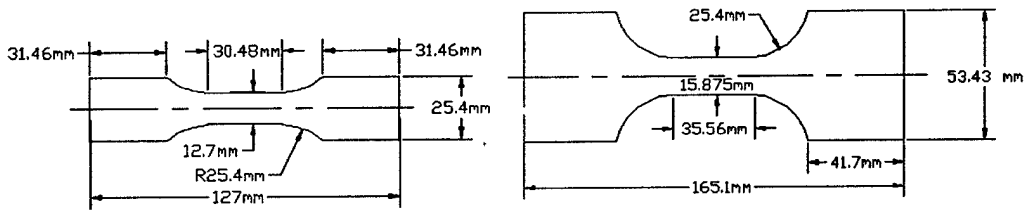

(a) Aluminum Structure I (b) Aluminum Structure II

Fig. 3.1.15 Tension specimens of aluminum meso-channel structures

3.2. Experiments

Static experiments under bending, compression, and tension were conducted at room temperature using an INSTRON 8500 servohydraulic testing system equipped with computer control and data acquisition. The system is used for static and fatigue experiments for advanced materials and the load capacity is 25 kN. The computer controller allows the experiments to be performed under a choice of either position, load or strain control.

3.2.1. Carbon/Graphite TES-Composites

Tension and compression experiments were conducted to generate the tensile and compressive properties of the material. As components of the carbon/graphite TES composites, empty graphitic foam, graphitic foam impregnated with PCM, and epoxy skin specimens were tested separately. The tension and compression specimens of graphitic foam were made of graphitic foam with different porosity. Depending on where the specimens were cut from the supplied block of the material, the graphitic foam density varied from 0.25 to 0.61 g/cm^3. This corresponded to a porosity ranging from 72% to 89%. The mean cell size of the foam is 500 μm. The relationship between the porosity of the graphitic foam and the mechanical properties of the specimens were observed experimentally. The results of tension and compression experiments are presented.

To evaluate the bending stiffness of the developed structures, bending experiments were conducted. The graphitic foam used in the 2D box bending structures was cut from the same

location from the material block, and the porosity was approximately 73%. Details of bending experiments are discussed.

Table 3.1 TES-composite mechanical properties

Property	Rigid Plate / Structural Ribs*	TES Volume** $\varepsilon_f = 0.73$	
Material	Carbon/Epoxy	Graphite foam	Foam/ Paraffin
Tensile Strength [MPa]	848	1.0	1.3
Young's Modulus (Tension) [MPa]	58000	105	464
Compression Strength [MPa]	131	1.4	4.2
Young's Modulus (Compression)[MPa]	57200	110	263

Notes: *Handbook/vendor supplied values, ** Measured values

Tension Experiments

Tension experiments were conducted for epoxy skin specimens and three types of graphitic foam specimens: empty graphitic foam specimens, graphitic foam specimens filled with PCM, and graphitic foam specimens filled with PCM and covered with graphite skins. The results of tension experiments are summarized in Table 3.1.

From the experimental observations, the ultimate strength of the skinned specimens is only marginally affected by the porosity of the graphitic foam (Fig. 3.2.1). Under tension loading the graphitic skin takes most of the tensile load since the elasticity modulus of the graphitic screen is 58000 MPa and the tensile ultimate strength of the skin is 848 MPa (Table 3.1), much higher than those of the filled graphitic foam. Due to the breakage failure mode of the cells under tension, the PCM fill does not have a significant influence on the tensile ultimate strength.

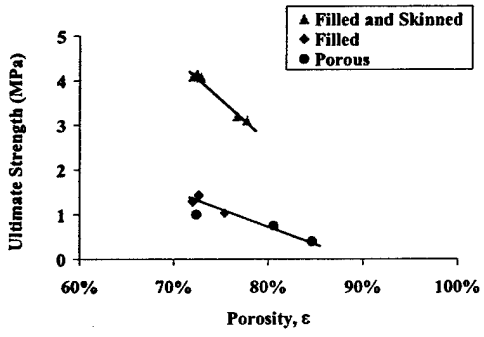

Fig. 3.2.1 Influence of graphitic foam porosity on tensile ultimate strength

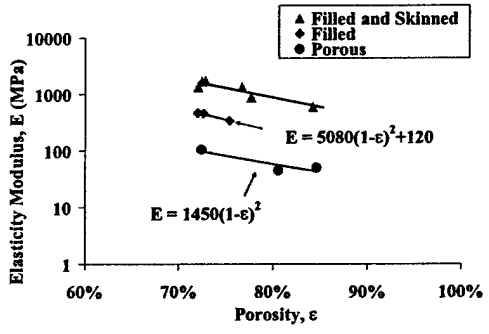

Fig. 3.2.2 Dependence of tensile elasticity modulus on porosity

Figure 3.2.2summarizes the influence of porosity of the graphitic foam on the elasticity modulus under tension load. Due to the significant difference between the elasticity moduli of the epoxy skin and the graphitic foam, a logarithmic scale was used for the vertical axis in Fig. 3.2.2. Both the graphitic skin and PCM increase the tensile elasticity modulus significantly. From the experimentally obtained formulas, the influence of porosity on the elasticity modulus for graphitic foam and filled graphitic foam follows a parabolic relationship. There is a constant (120) in the formula describing the relationship between the elasticity modulus and the porosity of the filled graphitic foam. When the porosity of the filled graphitic foam goes to 100%, there is only PCM left. The constant indicates the elasticity modulus of PCM.

Compression Experiments

Figures 3.2.3-3.2.5 show the compression experiment results for porous graphitic foam, graphitic foam filled with PCM, and graphitic sandwich structures. The graphitic foam had a very low elasticity modulus and strength. One characteristic of the graphitic foam, as shown in Fig. 3.2.3, is the wavy stress-strain curve after yielding. This property was a result of the buckling failure mode of the graphitic foam under compression which occurred layer by layer. It was experimentally observed that the wave length appeared in the load-deflection curve was equal to the cell size of the foam (500 μm).

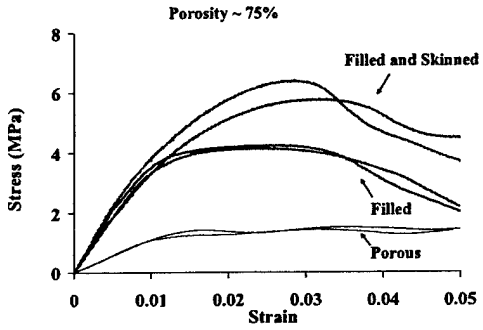

Fig. 3.2.3 Experimental stress-strain curves obtained from compression experiments

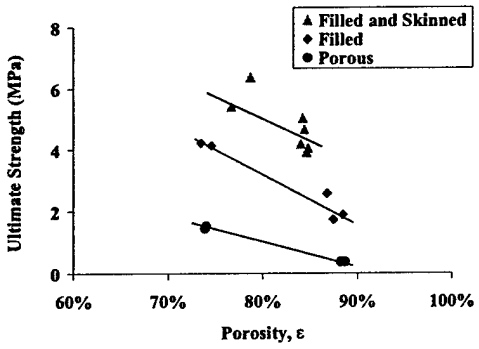

Fig. 3.2.4 Influence of Pocofoam porosity on compression ultimate strength

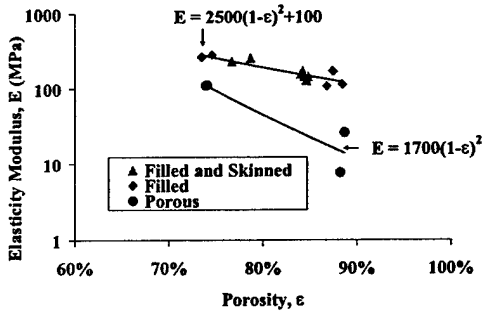

Fig. 3.2.5 Dependence of compression elasticity modulus on porosity

The results indicate that the PCM filled in graphitic foam enhances the compressive strength. The PCM fill and the graphitic skin added transverse constrains in the structure, thus retarding buckling and increasing strength. It is noticed in Fig. 3.2.5 that the addition of the graphitic skin

does not increase the elasticity modulus under compression due to the fact that the thin skin cannot carry compressive load. Tension and compression properties are different for the graphitic foam due to different failure mechanisms involved. Breakage of the cells causes the tensile failure while buckling of the cell ribs causes the compression failure. The influence of porosity on elasticity modulus for graphitic foam and filled graphitic foam follow a similar trend as that for tension. There is also a constant (100) in the formula describing the relationship between the elasticity modulus and the porosity of the filled graphitic foam. When the porosity of the filled graphitic foam goes to 100%, there is only PCM left. The constant indicates the compressive elasticity modulus of PCM.

Bending Experiments

Three-point bending experiments were conducted for Carbon/Graphite TES composites of 1D sandwich structures and 2D box structures to determine structural properties of the structures. The bending experiment results were used to evaluate the models developed in this study.

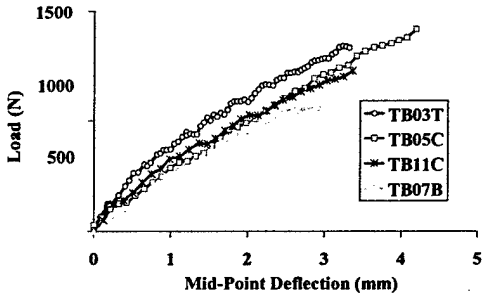

Fig. 3.2.6 Experimental observations from three-point bending experiments on graphitic sandwich structures

As shown in Fig. 3.2.6, the results for 1D sandwich structure (Fig. 3.1.3) are scattered in a certain range. This is because the porosity of the graphitic foam used in the 1D sandwich structure varied from 72% to 89% depending on the locations where the sample was cut from the supplied block of graphitic foam. Specimens cut from the top of the supplied block have the lowest porosity, specimens cut from the middle of the supplied block have the porosity higher than that of specimens cut from the top, and specimens cut from the bottom of the supplied blocks have the highest porosity. Specimen TB03T was cut from the top of the graphitic foam block and its porosity is lowest. Specimen TB05C and TB11C were cut from the center of the graphitic foam block and their porosities were higher than that of TB03T. Specimen TB07B was cut from the bottom of the graphitic foam block and its porosity is the highest. As shown in Fig. 3.2.6, the specimen made of lower porosity graphitic foam (TB03T) has a stronger bending stiffness, and the specimens made of higher porosity graphitic foam (TB05C, TB11C and TB07B) show a lower bending stiffness. The results are scattered, but they concentrate in a relatively narrow range. This shows that epoxy skins which have much higher elasticity modulus carried most of the load during bending so that the load-deflection curves of the specimens follow the same trend.

The fact that the curves are scattered shows that the core materials made of the graphitic foam do contribute to the structure during bending although the contribution is relatively small as compared to that of the epoxy skins.

For the experiments of the 2D box structure shown in Fig. 3.1.5, the porosity of the graphitic foam used was constant at 73%. For each condition, two specimens were tested. The average ultimate load for the 2-D box specimens (Fig.3.2.7) is 1090 N at room temperature. The deformation was nearly linear elastic before fracture occurred on the rigid plates. The ultimate strength was 830 N at a temperature of 70°C, an approximately 24% reduction from that of the room temperature. In addition, there existed a nonlinear load-deflection relationship before fracture failure when the temperature was 70°C. As a comparison, the results of an 1-D structure are also shown in Fig. 3.2.7. The 1-D structure was identical to that of the 2-D configuration except that there were no structural ribs and the TES composite was made of a single piece of graphitic foam. The ultimate strength of the 1-D structure at room temperature is 900 N. Clearly, the 2-D structure has a higher strength due to the existence of the structural ribs. It is noticed that the rigidity (the slope of the curves) of all the specimens are very similar. This indicates that while the temperature influences strength, it does not significantly affect the elasticity moduli of the materials used in the structure. Similar to the 1D sandwich structure, the 2D box structure displays elastic deformation during bending. From the experiment observations, the structure failed due to bulking of the upper part of the supporting ribs and the upper epoxy skin. The failure started from the upper part of the structure and the structure was finally broken into two parts.

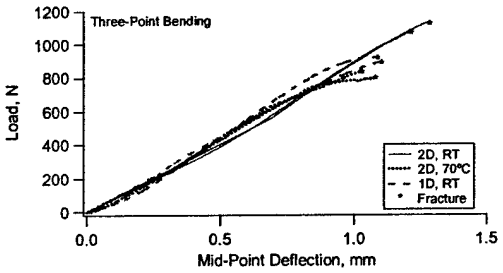

Fig. 3.2.7 Experiment results from three-point bending experiments of Carbon/Graphite 2D box structure.

Fatigue Experiments

Fatigue experiments were conducted with the 2-D structure specimens under three-point bending at room temperature and at 70°C, and the results are shown in Fig. 3.2.8. The load ratio (the minimum load versus maximum load in a loading cycle) was 0.1, and the testing frequency was 5 Hz. A higher frequency of 10 Hz was used for the two specimens having a fatigue life of more than 10^6 cycles. The fatigue life ranged from 1000 cycles to 3×10^6 cycles for the room temperature condition. At 70°C, the fatigue life ranged from 10 cycles to 1.2×10^6 cycles. From the fatigue curves shown in Fig. 3.2.8, an endurance limit can be approximately identified with a

value of 750 N for room temperature and 450 N for 70°C. Comparing to the ultimate strength of the structure, the endurance limit is approximately 70% of the ultimate strength for the room temperature condition. The ratio is 54% at 70°C. The endurance limit at 70°C is 60% of that at room temperature, a 40% reduction due to the increased temperature. Clearly, temperature has a great influence on the fatigue strength of the graphitic structure and it has a more significant influence on fatigue strength than does it on the static strength.

The influence of temperature on fatigue of the 2-D graphitic structure is also reflected in the shape of the fatigue curve. In a half-log scale used for the fatigue curve, the relationship between the maximum load and fatigue life is linear before reaching the endurance limit at room temperature (Fig. 3.2.8). As a common practice, the static ultimate strength can be viewed as the fatigue strength corresponding to a fatigue life of ¼ cycle. It is noted from Fig. 3.2.8 that at room temperature the static strength falls well into the linear extrapolation of the fatigue curve. This indicates that at room temperature the deformation of the 2-D graphitic structure is essentially elastic and the fatigue behavior resembles that of a brittle material. As a comparison, the fatigue curve shown in Fig. 3.2.8 for 70°C can be best described by a bi-linear curve in the half-log scale before reaching the endurance limit. Such a bi-linear fatigue curve is typical for a ductile material. The non-linear load-deflection curve obtained from the static experiments (Fig. 3.2.7) before fracture is an indication of material's plasticity. Therefore, it can be concluded that a temperature of 70°C alters the ductility of the 2-D structure.

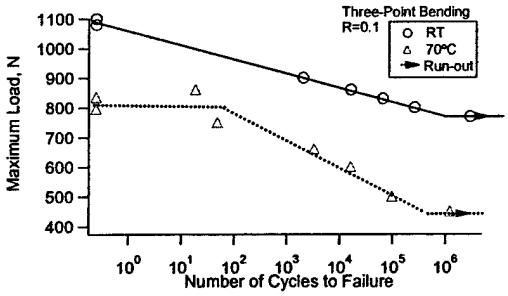

Fig. 3.2.8 Fatigue of 2-D box structure

Failure Modes

Both epoxy skin and graphitic foam display elastic deformation before fracture (Figs.3.2.9 and 3.2.10). The epoxy skin failed at a strain of 0.8%. The empty graphitic foam failed at a strain of 1%. The filled graphitic foam broke at a strain of 0.3% under tension and at a strain of 1.6% under compression. The skin and the graphitic foam broke before any plastic deformation was observed.

In the bending experiments, the upper part of the structure carries compression load and the lower part of the structure carried tension load. The epoxy skin is very strong under tension load, but the thickness of the skin is so thin (0.22mm) that it is easy to buckle. The upper part of the beam failed first from the experimental observation. Once the upper epoxy skin was buckled, the upper

part of the filled graphitic foam had to take over the compression load of the structure. The core material was weak as compared to the epoxy skin. It broke right after the upper skin failed.

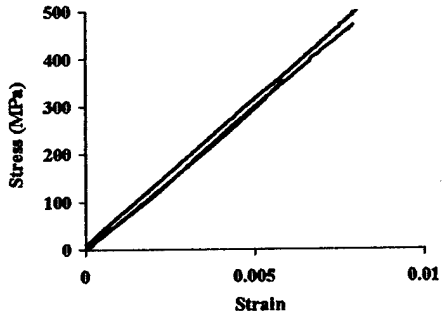

Fig.3.2.9 Elastic deformation of epoxy skin under tension

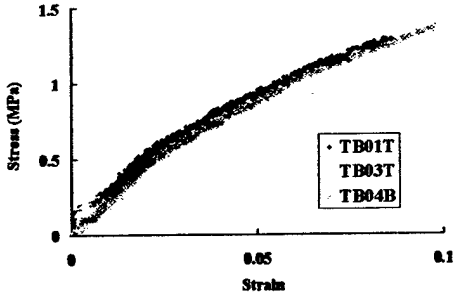

Fig. 3.2.10 Deformation of graphitic foam under tension

3.2.2. Screen Laminate TES-Composites Specimens

Tension Experiments

Copper screen specimens for tension experiments were brazed first. The cross sections of the copper wires were observed under microscope after brazing. As shown in Fig. 3.2.11 and Fig. 3.2.12, the grain size of the copper wire after brazing was much larger than that of the copper wire before brazing. Clearly, the mechanical properties of copper screen were changed by brazing.

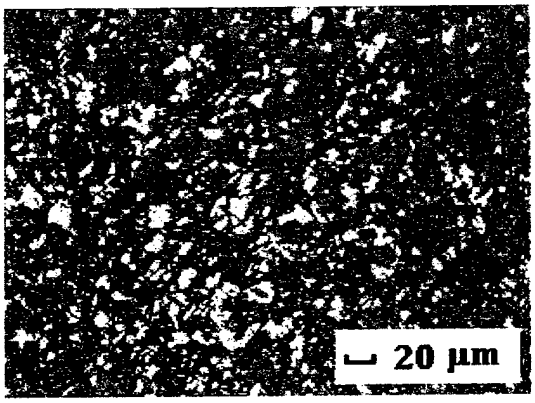

Fig. 3.2.11 Copper before brazing (x 400)

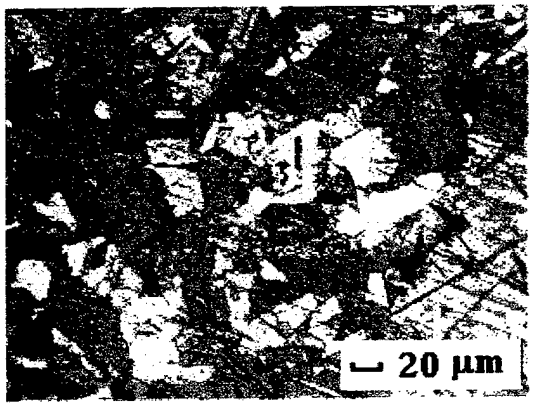

Fig. 3.2.12 Copper after brazing (x 400)

Since the brazing process apparently changed the properties of the copper wire, brazed copper wires were tested under uniaxial tension to generate the mechanical properties. As shown in Table 3.2, the yield strength obtained is 38 MPa which is much lower than that of the copper without brazing (about 300 MPa). These properties were used in the finite element modeling of the single layer copper screen.

Uniaxial static tension experiments were conducted on one-layer copper screen specimens. Table 3.2 lists the mechanical properties of the copper screens. The copper screen is a porous material. Its elasticity modulus and yield strength were much lower than those of the brazed copper wire. Mechanical properties obtained from the tension experiments of the screen were used to evaluate the finite element models for the single layer copper screen under tension. These properties were also the inputs to the finite element models for the screen laminates under bending.

Table 3.2 Mechanical Properties of Brazed Copper Wire and Copper Screen

Material	E (MPa)	Yield Strength (MPa)	Experiment Type
Copper wire	122300	37.98	Tension
	-	-	Compression
Copper screen (zero degree)	4750.2	3.9	Tension
	1361.8	3.0	Compression
Copper screen (45 degree)	893.4	1.3	Tension
	-	-	Compression

Compression Experiments

Compression experiments were conducted to produce the compression properties of the copper screen. Compression samples shown in Fig. 3.1.10 were small blocks cut from the brazed copper laminates. Results from the compression experiments revealed that the yield strength under compression was lower than that under tension (Table 3.2). Tension and compression properties are different for the copper screen due to different failure mechanisms involved. Buckling of the thin wire under compression made the yield stress under compression much smaller than the yield stress under tension. The asymmetric tension-compression properties were used in the finite element models to predict the performance of a beam under bending.

Bending Experiments

Three-point bending experiments were conducted for the screen laminate specimens shown in Fig.3.1.11. The span between the two supporting points for all bending experiments was 76.2 mm. The laminates of $[0°_5]$, $[0°_7]$, $[0°_9]$, $[45°_5]$ and [0°/45°/0°/45°/0°] (as described in section 3.1.2.6) were tested. The load versus mid-point deflection curves shown in Fig. 3.2.13 displayed the consistency in the experiment results of the screen

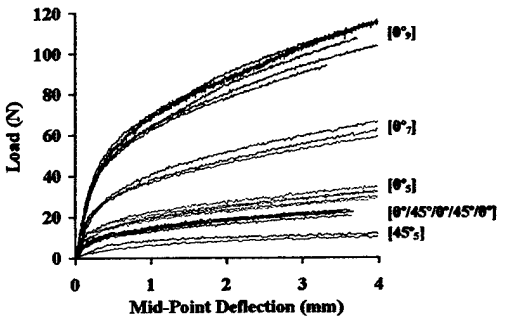

Fig. 3.2.13 Experiment results from three-point bending experiments of screen laminates

laminate specimens. This indicates that the brazing process in making the screen specimens was satisfactory.

As shown in Fig. 3.2.13, it is obvious that the mechanical behavior strongly depends on the number of layers as well as the orientation of the wire direction. The specimens having more layers of copper screen are stiffer. With the same laminae orientation, the $[0°_9]$ laminates are the strongest and the $[0°_5]$ laminated are the weakest. Having the same number of layers, the zero degree laminates are stronger than the laminate with 45 degree screens. The $[0°_5]$ laminates are stronger than the [0°/45°/0°/45°/0°] laminates, and the [0°/45°/0°/45°/0°] laminates are stronger than the $[45°_5]$ laminates.

Failure Modes

The copper screen displays elastic-plastic behavior, and the copper screen did not break during tension, compression, and bending experiments. The copper screen material was considered to fail when the plastic deformation reached to a certain degree. From the experimental observation, if the total strain of the material exceeded 0.08%, the material was deformed plastically. The copper screens do not have a distinct yielding point. Failure was defined when its plastic strain reached 0.2%.

3.2.3. Aluminum Meso-Channel Structure

Tension Experiments

The stress-strain data obtained from the tension experiments are shown in Fig.3.2.14. Table 3.3 summarized the mechanical properties of the aluminum structures. The yield stress of Aluminum Structure II is much lower than that of Aluminum Structure I.

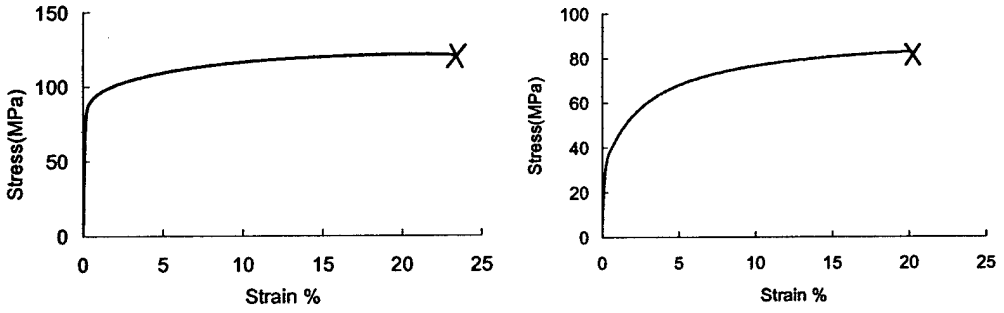

(a) Tension experiment result for Aluminum Structure I

(b) Tension experiment result for Aluminum Structure II

Fig. 3.2.14 Tension experiment results

Table 3.3 Mechanical properties of aluminum meso-channel structures

Aluminum Structure #	Elasticity Modulus (GPa)	Yield Stress (MPa)	Ultimate Stress (MPa)	Elongation (%)
I	66	71.6	120.5	23.4
II	67.5	8.9	81	20.3

Bending Experiments

One layer of the Aluminum Structure I specimens were subjected to three-point bending as shown in Fig. 3.2.15 (a). The bending specimens of Aluminum Structure I are 177.8 mm long, 58.3 mm wide, and 5.96 mm thick. The span for the three-point bending experiments is 127 mm. The three-layer specimens of Aluminum Structure II were subjected to four-point bending as shown in Fig. 3.2.15 (b). The specimens of structure II are 146.05mm long, 53.43mm wide, and 2.77 mm thick. The span between the supporting points is 124.74mm and the span between the loading points is 52.57 mm. The load versus load point deflection curves are shown in Figs. 3.2.16 and 3.2.17.

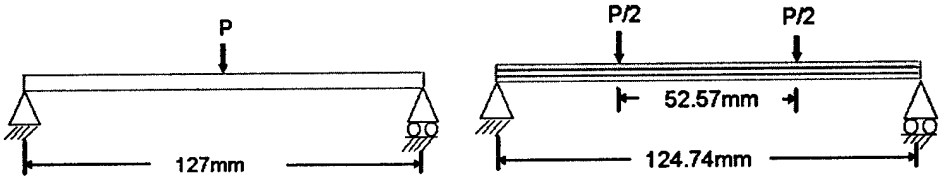

(a) Four-point bending of Aluminum Structure I

(b) Four-point bending of Aluminum Structure II

Fig. 3.2.15 Bending experiments

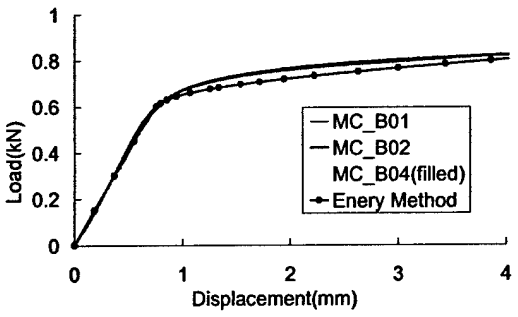

Fig. 3.2.16 Energy method results and experimental observations for three-point bending tests on one-layer specimens of Aluminum Structure I.

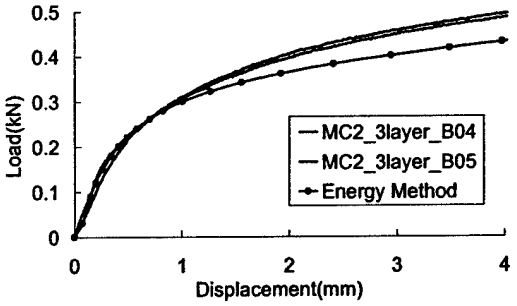

Fig. 3.2.17 Energy method results and experimental observations for four-point bending tests on three-layer specimens of Aluminum Structure II.

3.3. Modeling

A major objective of the current research was to develop models that can be used to predict the mechanical performance of the multifunctional structures. Two types of models, the energy method model and the finite element model, were developed. A multiscale methodology was developed for the finite element modeling of screen laminates. Two scales of the finite element models were developed. One is the finite element model of the screen laminate and the other is the finite model of the single layer screen.

3.3.1. Homogenization Theory

Both copper screen and graphite skins have equal wire/fiber diameter and spacing in two directions. The geometry of these two materials is regular and repetitive. Therefore, it is possible to employ the homogenization theory to determine the equivalent properties for the brazed plain weave mesh. When applying the homogenization theory, a transversally isotropic model is adequate for representing plane weave structures in structural calculations [Hübsh,2000]. Consequently, the laminae of the copper screen and the graphite/epoxy skins were considered transversally isotropic, and the material properties in X and Y directions (Fig. 3.3.1) were considered to be isotropic. Due to the isotropy, mechanical parameters needed to be characterized are E_x and σ_x. E_x is the elasticity modulus in the X direction and σ_x is the nominal stress in the X direction.

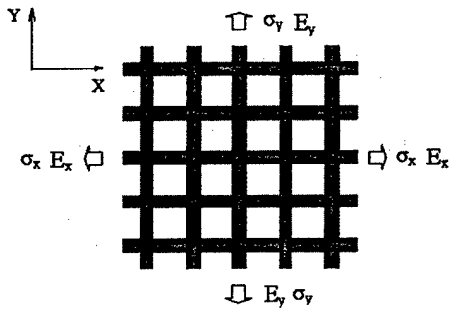

Fig. 3.3.1 Material directions of copper screen.

3.3.2. Energy Method Simulations

The energy method was used to simulate the three-point bending experiments of the composite structures. The inputs are the mechanical properties obtained from the tension and compression experiments for the materials. According to the energy conservation law, the work done by the external force should be equal to the total strain energy stored in the bending structure. Dividing the strain energy stored in the bending structure by the external force, the deflection at the load point could be obtained. A load-deflection curve can be predicted.

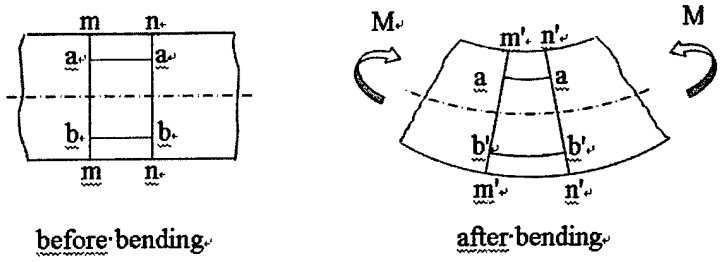

Fig. 3.3.2 Plane cross section of the beam remains plan after bending.

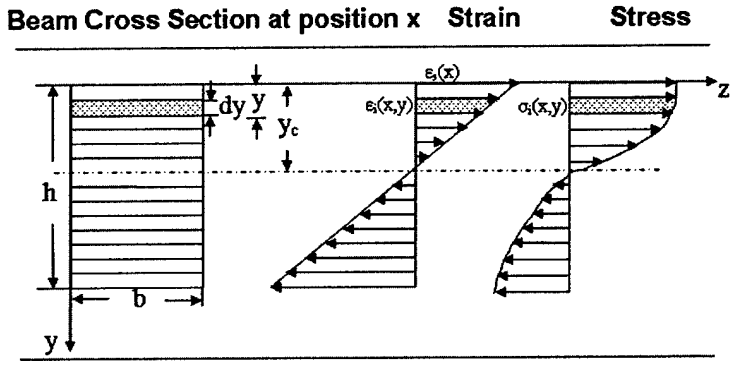

Fig. 3.3.3 Strain – stress diagram over cross section of the beam

To determine the strain energy stored in the structure, it is assumed that plane cross sections of the structure remain plane under bending, a condition that is valid for both nonlinear and linear materials. As shown in Fig. 3.3.2, before bending deformation occurs, the cross sections of the beam mm and nn are vertical to the horizontal planes aa and bb. After the deformation, the aa and bb plane deform to a curvature surfaces aa' and bb' and the cross sections mm and nn deform to cross sections mm' and nn'. mm' and nn' remain planes and are vertical to planes aa' and bb'. Based on the assumption, the normal strain over the cross section of a beam varies linearly over the cross section of the structure (Fig. 3.3.3). This means that when the surface strains of the structure are known, the strains everywhere in the structure can be obtained. The stresses can be determined according to the stress-strain relationships of the materials. The stress-strain relationships of the materials were obtained from the tension and compression experiments. When the strains and stress are known, the strain energy of the whole structure can be numerically obtained.

Procedure of Energy Method Simulation

To simulate a real bending experiment, the load applied to the structure is increased step by step. As many as 1000 increments are used to reach a maximum load. There are 1000 time moments in the simulation and time moment i ($0 \leq i \leq 999$) corresponds to an external load P_i. The

external load P_i is known and the deflection δ_i caused by the external load P_i needs to be obtained from the simulation. There are three steps in the simulation procedure. The first step of the energy method is to obtain the surface strains $\epsilon_s(x)$ at position x of the structure from the external loading force P_i. The bending moment diagram presented in Fig. 3.3.4 shows how M(x) varies with respect to position x when a load P_i is applied in the three-point bending experiment. The bending moment on a given cross section at position x is,

$$M(x) = \begin{cases} \frac{1}{2}Px & \text{when } x \le L/2 \\ \frac{1}{2}P(L-x) & \text{when } x > L/2 \end{cases} \tag{3.1}$$

where M(x) is the bending moment over the cross section of the structure, P_i is the external load applied to the structure, L is the span between the two supporting points of the beam, and x is the coordinate along the beam. With Eq. 3.1, the bending moment is known everywhere in the beam for a given external load.

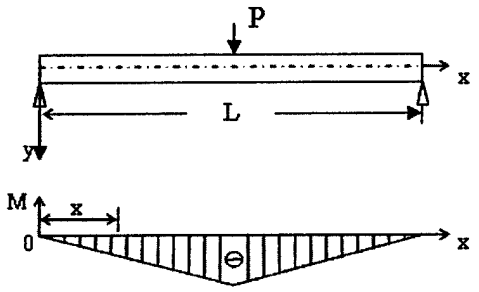

Fig. 3.3.4 Bending moment diagram for three point bending

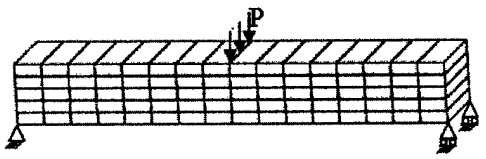

Fig. 3.3.5 Finite volumes of the beam

The surface strain on a given cross section is related to the bending moment. The beam is divided to finite volumes as shown in Fig. 3.3.5. The strain and stress in each volume are considered to be uniform. Due to symmetry in the beam, one half of the structure is considered. Figure 3.3.3 shows the linear variation of the strain over the cross section. On the cross section, there is a neutral axis where the strain is zero. The location of the neutral axis is critical for the strain distribution over the cross section. Determination of the position of the neutral axis will be discussed in detail. Here it is assumed that the neutral axis coincide with the centroid of the cross section. The shaded box represents a finite volume. The strain in every finite volume is determined according to the linear distribution of the strain over the cross section,

$$\varepsilon_i(x,y) = \frac{h-2y}{h}\varepsilon_s(x) \text{ when } 0 < y \le h \qquad (3.2)$$

where i indicates the ith time moment which corresponds to the external load P_i, $\epsilon_i(x,y)$ is the strain of the finite volume at location (x, y) at time moment i, $\epsilon_s(x)$ is the surface strain of the beam at position x, and h is the height of the beam. If the surface strain is known, the stress on the volume $\sigma_i(x,y)$ can be determined from the stress-strain relationship of the material.

$$\sigma_i(x,y) = f(\varepsilon_i(x,y)) \qquad (3.3)$$

Figure 3.3.3 also shows that stress distribution over the cross section can be nonlinear when the beam is made up of different materials and/or deformation is elastic-plastic. When the stress and strain in each finite volume are known, the moment over the cross section can be computed using the following equation,

$$M(x) = b\int_{-h/2}^{h/2}\sigma_i(x,y)y\,dy \qquad (3.4)$$

where h is the height of the beam, b is the width of the beam, and y is the coordinate along the cross section of the beam (Fig. 3.3.3). Integrating over the cross section, the relationship between bending moment M(x) and the surface strain $\epsilon_s(x)$ can be obtained. The first step of the energy method simulation is accomplished since from the external load P_i, the bending moments along the beam can be obtained. From the bending moment-surface strain relationship, the surface strains along the beam are obtained.

The second step of the energy method is to calculate the strain energy increment in the beam from time moment i-1 to time moment i. The surface strains of the beam at the time moment i are obtained from the first step. The strain in every finite volume is obtained from Eq. 3.2 and the stress in every finite volume is obtained from Eq. 3.3. From time moment i-1 to i, the strain energy increment ΔU_i of the structure is:

$$\Delta U_i = \int_V \sigma_i(x,y)\Delta\varepsilon_i(x,y)dV \qquad (3.5)$$

where V is the volume of the beam, $\sigma_i(x,y)$ is the stress in a finite volume at location (x,y) at time moment i, and $\Delta\varepsilon_i(x,y)$ is the strain increment caused by the current external load P_i.

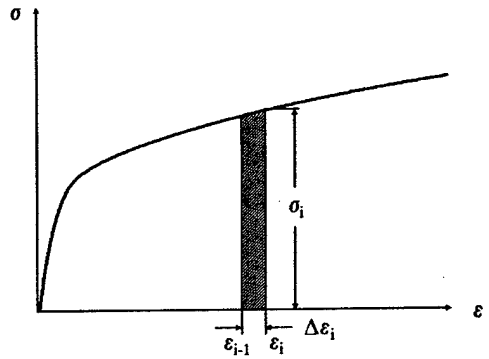

Fig. 3.3.6 Strain energy density increase

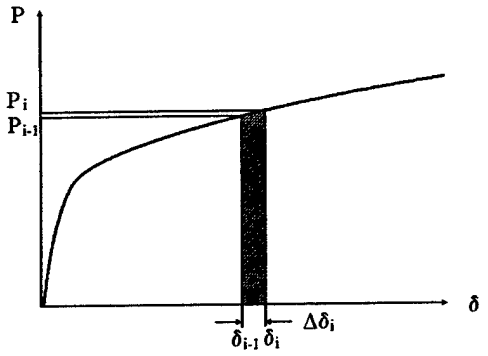

Fig. 3.3.7 Work done by the external load P

The strain increase, $\Delta\varepsilon_i(x,y)$, during one incremental step is,

$$\Delta\varepsilon_i(x,y) = \varepsilon_i(x,y) - \varepsilon_{i-1}(x,y) \tag{3.6}$$

where ϵ_i is the strain at time moment i, ϵ_{i-1} is the strain at time moment i-1, and $\Delta\varepsilon_i$ is the strain increment. Figure 3.3.6 shows the strain energy density increment schematically. The shaded area indicates the strain energy density. The strain energy increment can be obtained by integrating the strain energy density over the whole volume of the structure as shown in Eq. 3.5.

The third step is to obtain the deflection generated from time moment i-1 to i. According to the energy conservation law, the work done by the external load during a load increment should be equal to the increase in the strain energy in the structure. In Fig. 3.3.7, the shaded area is the work done by the external load.

$$\Delta W_i = P_i \Delta\delta_i \tag{3.7}$$

where ΔW_i is the work increment done by the external load, P_i is the external load at time moment i, and $\Delta\delta_i$ is the deflection increment produced by the load P_i. From the energy conservation law,

$$\Delta W_i = \Delta U_i \tag{3.8}$$

Therefore, deflection increase from time moment i-1 to i can be determined.

$$\Delta\delta_i = \frac{\Delta W_i}{P_i} = \frac{\Delta U_i}{P_i} \tag{3.9}$$

The deflection of the structure at time moment i is equal to the deflection at the previous time moment i-1 plus the deflection increase at load point i. Deflection is calculated,

$$\delta_i = \delta_{i-1} + \Delta\delta_i \tag{3.10}$$

where δ_i is the deflection at time moment i, δ_{i-1} is the deflection at time moment i-1, and $\Delta\delta_i$ is the deflection increment.

As was mentioned previously, the load applied to the structure is increased step by step. There were 1000 time increments in the program and each time moment corresponds to an external load. Deflection at each time moment is calculated with the energy method. A load-deflection curve is generated.

Determination of the Neutral Axis

As shown in Fig. 3.3.3, strain distribution has a neutral axis. The neutral axis is the axis on the cross section of beam where the strain equals to zero. For a beam that is structural symmetry and is made of materials displaying tension-compression symmetry, the neutral axis passes through the centroid of the cross section. The strain along the y direction of the cross section can be obtained according to Eq. 3.2. For a structurally asymmetric beam or for a beam that is made of materials displaying tension-compression asymmetry, the neutral axis may not coincide with the centroid of the beam cross section. The stress-strain variations of the copper screen and graphitic foam in compression are different from those in tension as described in Section 3.2. The position of neutral axis is no longer coinciding with the horizontal centroidal axis on the beam cross section and needs to be determined.

If the position of neutral axis on the cross section of the beam is y_c, the strain over the cross section can be obtained,

$$\varepsilon_i(x,y) = \frac{y_c - y}{y_c}\varepsilon_s(x) \text{ when } y \le y_c \tag{3.11}$$

where y_c is the position of neutral axis and $\epsilon_s(x)$ is the surface strain of the beam at location x. The position of neutral axis can be found according to the force equilibrium. To achieve the force equilibrium over the cross section of the beam, the force above the neutral axis should equal to the force below the neutral axis. Therefore, the neutral axis is found by solving the following equation.

$$\int_0^{y_c} \sigma_i(x,y)bdy + \int_{y_c}^{h} \sigma_i(x,y)bdy = 0 \tag{3.12}$$

where $\sigma_i(x,y)$ is the stress of finite volumes, b is the width of the beam, and h is the height of the beam. To solve the equation, a recursive method was used. The initial value of y_c is set to be h/2 and Eq. 3.12 is checked for equilibrium. If the force on the area above (the first part of the equation) is larger than that on the area below (the second part of the equation), y_c is moved upward. If the force on the area above (the first part of the equation) is smaller than that on the area below (the second part of the equation), y_c is moved downward. According to the new y_c value, the strains, stresses, and forces on the cross section are calculated again. The process continues until Eq. 3.12 is satisfied.

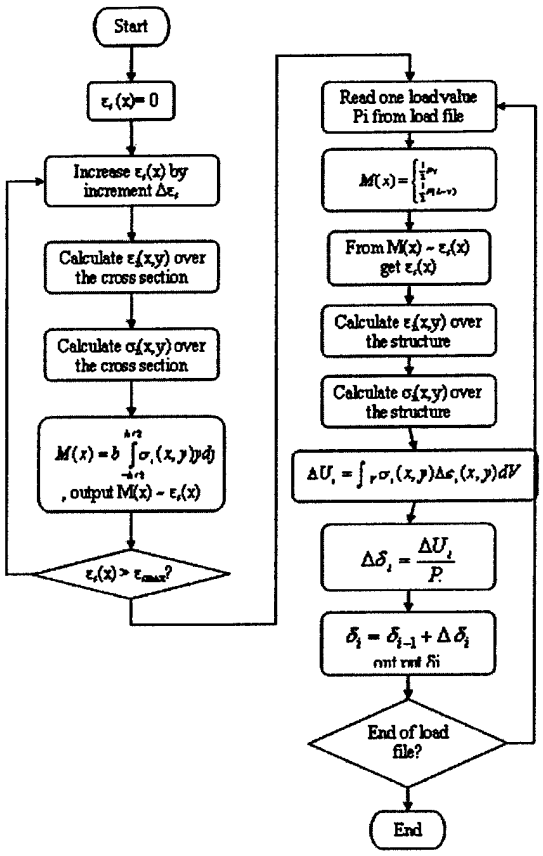

Fig. 3.3.8 Flow chart of the C++ program for the energy method

A computer code using C++ was developed to execute the energy method. A recursive subroutine was written to find the neutral center. The condition to stop the recursive call of the subroutine is that Eq. 3.9 is satisfied. Figure 3.3.8 shows the flow chart for the C++ code and Fig. 3.3.9 shows the flow chart for the subroutine to find the neutral center.

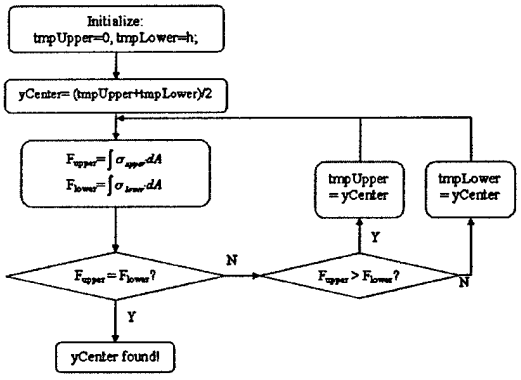

Fig. 3.3.9 Flow chart of the subroutine to find the neutral position of the cross section

Simulations for Carbon/Graphite TES-Composites

Graphite skin and graphitic foam in the Carbon/Graphite TES-composites display elastic deformation before failure. Only elastic properties are involved. The elasticity moduli of the materials can be applied directly to the calculation of stress in each finite volume. Eq. 3.3 in Section 3.3.2.1 is replaced with the following equation.

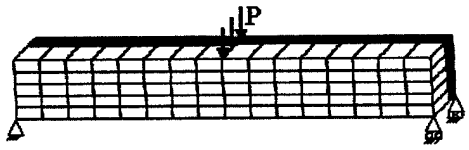

Fig. 3.3.10 Finite volume of 2D box structure of Carbon/Graphite TES composite

$$\sigma_i(x,y) = E\varepsilon_i(x,y) \tag{3.13}$$

where E is the elasticity modulus of the material obtained from tension or compression experiments, $\epsilon_i(x,y)$ is the strain of the finite volume at location (x,y), and $\sigma_i(x,y)$ is the corresponding stress.

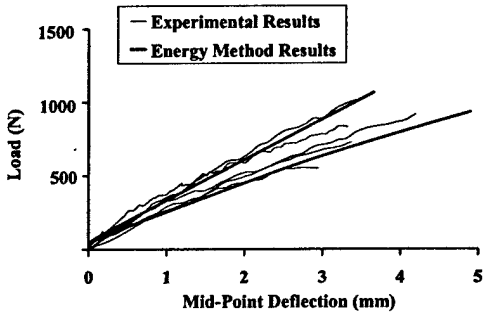

Fig. 3.3.11 Results of the energy method model and experimental observations for three-point bending experiments on 1D graphitic sandwich structures

To simulate the actual corrugated shape of the graphite skin in the carbon/graphite TES-composites of the 2D box structure (Fig. 3.1.5), every finite volume was divided into two parts (Fig. 3.3.10). The shaded part contains the graphite skin only and the other part contains the graphitic foam only. The strain energy of these volumes is calculated separately. Corresponding to the external load P_i, the strain energy increase (ΔU_i) of the structure is,

$$\Delta U_i = \int_{V1}(E_1\varepsilon_i(x,y))\Delta\varepsilon_i(x,y)dV + \int_{V2}(E_2\varepsilon_i(x,y))\Delta\varepsilon_i(x,y)dV \tag{3.14}$$

where V1 is the volume of the graphite skin material, V2 is the volume of the graphitic foam, E_1 is the elasticity modulus of the skin, and E_2 is the elasticity modulus of the graphitic foam. For the 1D sandwich structure, the core of the sandwich structure contains graphitic foam only. There is no corrugated shaped graphite skin in the middle. The value of V1 is set to be zero.

Figure 3.3.11 shows the energy method results of carbon/graphite TES composites of 1D sandwich structure compared with the experimental observations obtained from the three-point bending experiments. Since the core material of specimens, the graphitic foam, varied in porosity, the energy method model results in two curves in Fig. 3.3.11 representing the upper and lower bounds of simulation results. In the simulation, the surface strain of the material was

checked. If the surface strain of the material exceeds the ultimate strain of the epoxy skin (0.8%), the structure was considered to fail. Clearly, the energy method model can adequately predict the deformation and failure for the carbon/epoxy-paraffin/foam graphite sandwich structure.

The load versus mid-point deflection curves and the energy method simulation results of carbon/graphite TES composites of 2D box structure are shown in Fig. 3.3.12. The energy method developed can predict reasonable deformation and failure in close agreement with the experimental observations. When applying the energy method, the maximum surface strain of the structure should not exceed 0.8%, which is the ultimate strain of epoxy skin. When the surface strain exceeded 0.8%, the structure was considered to be failed.

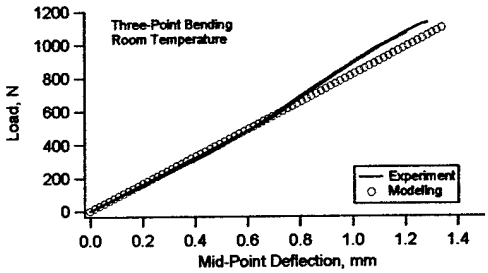

Fig. 3.3.12 Energy method results and experimental observations for three-point bending experiments on 2D box structure specimens

Simulations for Copper Screen Laminates

Since the screen laminates were made of copper screen, a ductile material, the elastic-plastic behavior of the material was considered when the screen laminate beam was loaded beyond the elastic limit of the material. Naturally, the behavior of a structure in elastic-plastic bending depends on the stress-strain relationship of the material. As was discussed in Section 3.2, the copper screen has different behaviors in tension and in compression. The yield stress under tension is different from that under compression. The neutral axis of the cross section of the beam needs to be found.

The strain-stress relationship of copper screen is described using a power law. The total strain of the elastic-plastic material equals to the sum of the elastic strain and the plastic strain. The elastic-plastic stress-strain relationship of the copper screen can be described using the following power law equation:

$$\varepsilon_T = \varepsilon_e + \varepsilon_P = \frac{\sigma}{E} + \left(\frac{\sigma}{K}\right)^{1/n} \quad (3.15)$$

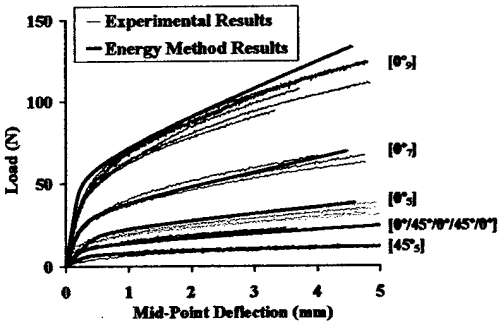

Fig. 3.3.13 Energy method results and experimental observations for three-point bending experiments on copper screen laminates

where ϵ_T is the total strain, ϵ_e is the elastic strain, ϵ_p is the plastic strain, σ is the stress, E is the elasticity modulus, K is the strength coefficient, and n is the strain hardening exponent. The values of K and n were obtained by fitting the stress-strain curve experimentally obtained with Eq. 3.15. As was described preciously, the surface strains of the beam can be determined from the bending moment-surface strain relationship (Eq. 3.4). Having found the surface strain and the neutral axis of the structure (y_c), the strain in each finite volume can be determined (Eq. 3.11). The stress is obtained by solving Eq. 3.15.

The copper screen laminates of different layers and different orientations were subjected to three-point bending. The load versus mid-point deflection curves of laminates of $[0°_5]$, $[0°_7]$, $[0°_9]$, $[45°_5]$, and [0°/45°/0°/45°/0°] are shown in Fig. 3.3.13. The results from the energy method are compared with the experimental observations. The mechanical behavior of the laminates strongly depends on the number of layers and the orientation of the wire direction. The energy method model provided deformation of the copper screen laminates comparable with the experiment observations. The method can predict the performance of the copper screen laminates under three-point bending.

Simulations for Aluminum Meso-Channel Structures

Using the stress-strain curves obtained from the tension experiments, the different types of specimens were divided into finite volumes, and the energy method described was applied to analyze the mechanical behavior of the aluminum structures. The results are compared with the experimental observations in Figs.3.2.19 and 3.2.20. The energy method can provide deformation of the aluminum skin laminates comparable with the experiments.

3.3.3. Finite Element Simulations

Three types of structures were investigated using the finite element method. They were 1D sandwich structure of carbon/graphite TES composites under bending, screen laminates under bending, and one layer woven mesh under tension. The finite element simulation results were evaluated with the experimental observations.

Simulations of One-Dimensional Sandwich Structure of Carbon/Graphite TES-Composites

A two-dimensional finite element model was built to simulate the behavior of the 1D sandwich structure of Carbon/Graphite TES composites. The finite element software package ANSYS 6.0 [2002] was used to do the simulation. Element PLANE42, a two-dimensional four-node element, was used to construct the model. The skin elements in the model have a length of 0.635 mm and a width of 0.0254 mm. The core elements are squares with each side being 0.635 mm.

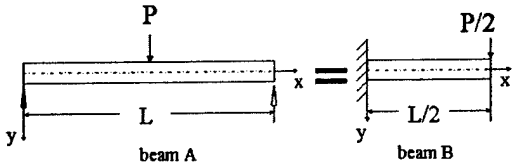

Fig. 3.3.14 Model simplification

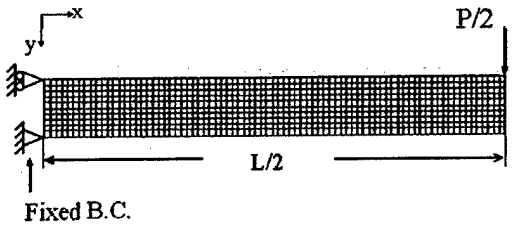

Fig.3.3.15 2D modeling of 1D sandwich structure of Carbon/Graphite TES composites with boundary conditions

Due to the symmetry of the structure, only one half of the structure was modeled. As shown in Fig. 3.3.14, beam A under three-point bending is equivalent to beam B under suspension load. The length of the beam B is one half of that of the beam A and the load applied on beam B is one half of that applied on beam A. The deflections yielded at load points of both structure are the same. Therefore beam B, instead of beam A, was modeled in the finite element simulation. Figure 3.3.15 shows the finite element modeling simulating the three-point bending experiments. One side of the beam is fixed in both x and y directions and the load applied in the model is one half of that of the actual load applied in the three-point bending experiments.

In the finite element simulations, the core of the 1D sandwich structure (Fig. 3.3) is treated as a composite beam consisting of two different materials due to the tension-compression asymmetry of the graphitic foam. One material had the tensile mechanical properties of the graphitic foam, and the other material had the compression mechanical properties of the foam. In the model, the graphitic skin displays elastic deformation. The nonlinear elastic-plastic material properties of the graphitic foam filled with PCM are considered. Figure 3.3.16 shows the y direction deflection simulation result contour when the structure shown in Fig. 3.3 was applied a load of 80 N.

The graphitic foam used in specimens of 1D sandwich structure of the carbon/graphite TES composites varied in porosity. The finite element model generates two curves in Fig. 3.3.17 representing the upper and lower bounds of simulation results respectively. In the finite element simulation, when the results of simulation displayed relatively large deformation as compared to the previous step, the structure was considered failed. The finite element model can predict the deformation and failure for the carbon/epoxy-paraffin/foam graphite sandwich structure.

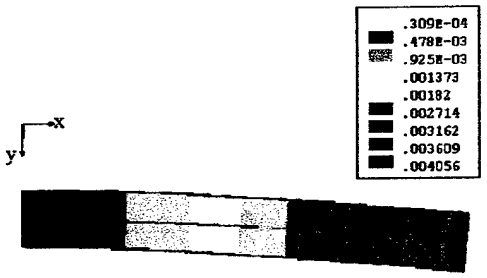

Fig.3.3.16 Y direction deflection simulation result contour of 2D modeling of 1D sandwich structure of carbon/graphite TES composites (unit: m, load applied: 80N in y direction)

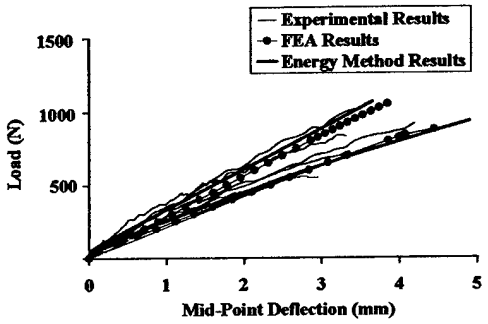

Fig. 3.3.17 Model results and experimental observations for three-point bending experiments on 1D graphitic sandwich structures

Simulation of Screen Laminates

The finite element simulations were conducted for screen laminates (Fig. 3.1.13) of $[0°_5]$, $[0°_7]$, $[0°_9]$, $[45°_5]$, and [0°/45°/0°/45°/0°] (described in section 3.1.2.6). Hyper Mesh marketed by Altair Engineering [2002] was chosen to build the mesh model, while ABAQUS [2002] was used to conduct the finite element calculation of screen laminates. Element C3D8, a three-dimensional eight-node solid element, was used to construct the model. The elements in the model have a length and width of 1.587 mm and a thickness of 0.457 mm. Due to the symmetry of the problem, one half of the structure was built in the model.

Figure 3.3.18 shows the mesh model. One side of the model had a fixed boundary. All the three translations of nodal x, y and z directions on this side were set to zero. Load was applied on the middle line of the structure on the top surface.

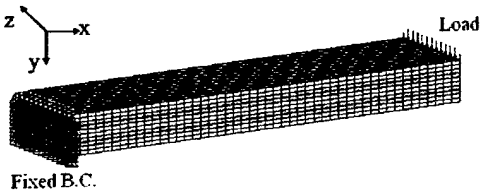

Fig. 3.3.18 Finite element model of screen laminates

There were 13 nodes on the middle line, and load was distributed uniformly over the elements. In total, 50 N were applied to the screen laminates that had less than seven layers. Nine-layer screen laminate was loaded with 100 N. An output file in HyperMesh was generated for the model built. The output file is the input file for ABAQUS calculation.

An existing material model for gray cast iron plasticity was used to simulate the stress-strain relationship of the copper screen laminate. Cast iron plasticity is one of the inelastic models included in the material library in ABAQUS. The cast iron plasticity model provides elastic-plastic behavior with different yield strengths and hardening in tension and compression which can be used to simulate the tension-compression asymmetry of the copper screen. According to

The size of the model is 11.1 mm × 11.1 mm. ANSYS provides a sweep method to build a 3D model from 2D. A circular area was created first and was meshed with 2D elements. A trace line was built following the shape wires of the plain weave copper screen. The area was swept along the trace line to create the 3D model of a copper wire. At the same time, the 2D elements were swept to form 3D elements. To simulate the brazed copper screen specimen, the joints of the copper wire needed to be "welded" together. The displacements of all nodes on each joint need to be identical so that nodes on the joints will move together. CP is an ANSYS command to couple ("weld") the degree of freedoms (DOF) of nodes together. The DOFs that are coupled generate a couple set. Figure 3.3.21 shows the details of the couple sets. A set of coupled DOFs contains a prime DOF, and 64 other DOFs. Coupling causes only the prime DOF to be retained in the analysis' matrix equations, and will result in all the other DOFs in a coupled set to be eliminated. The value calculated for the prime DOF will then be assigned to all the other DOFs in a coupled set.

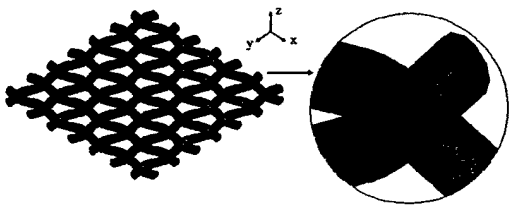

Fig. 3.3.21 Finite element model of single layer copper screen with coupled DOF sets

As being described in Section 3.2.1.1, tension experiments of single copper wires were conducted. Tension properties of copper wire after brazing were obtained and were used as the input for the finite element simulation for the copper screen. Figure 3.3.22 shows the piecewise linear model for the stress-strain relationship of the copper wire which was input to the ANSYS program. There are 3-linear segments in the model.

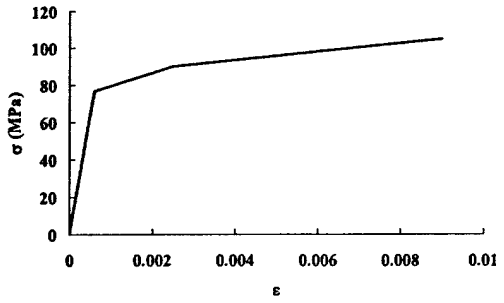

Fig. 3.3.22 Multi-linear model for the stress-strain relationship of copper wire

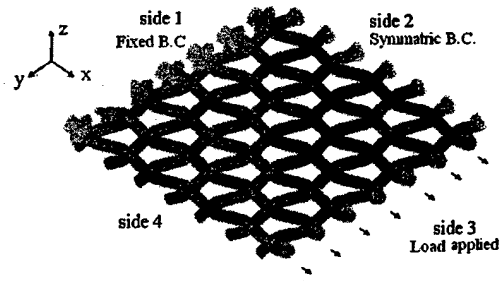

Fig. 3.3.23 Load and boundary conditions of copper wire mesh

Figure 3.3.23 shows the boundary condition and load applied on the zero-degree model. There are four sides in the model. All the DOFs of the nodes on side one were set to zero (fixed boundary condition). Side two was applied with a symmetric boundary condition, and side three

was applied with displacement which was equivalent to a 0.2% strain deformation. Side 4 was set to be free. Since the model is symmetry in the y direction, the symmetric boundary condition sets all the y direction DOFs of the nodes on side two to zero. A total of 1000 incremental steps were used in the simulation. Figure 3.3.24 shows the contour of the displacement in the x direction of the deformed copper screen under tension. The total displacement applied in the x direction was 0.023mm. The model for the 45-degree copper screen was the same as that of zero-degree except that the load was applied in the 45 degree direction.

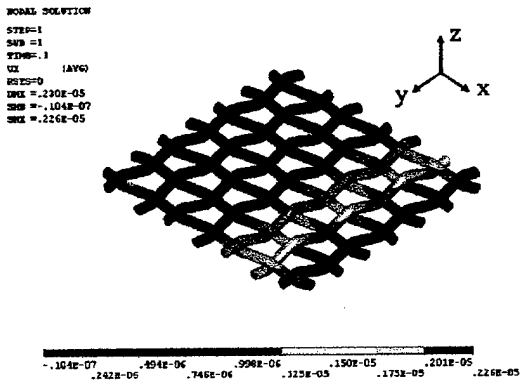

Fig. 3.3.24 X direction displacement contour of deformed copper screen under tension (displacement applied: 0.023mm in x direction)

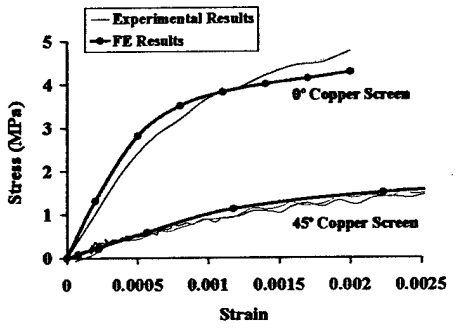

Fig. 3.3.25 Finite element simulation results and experimental observations for single layer copper screen under tension

The finite element simulation results are compared with experiment results in Fig. 3.3.25. The finite element models of one-layer brazed copper screen in both orientations well simulated the mechanical performance of the brazed copper screen material and the models can be used to predict the homogenized mechanical properties of the copper screen. The mechanical properties predicted by this model can be used to model the screen laminates. This method can replace the single layer mechanical experiments.

Meso-Channel and Lattice Aluminum Structures

Aluminum alloys are light-weighted with high thermal conductivity, attractive strength, and great manufacturability. Effective thermal performance and desirable mechanical properties can be achieved through a careful design of the detailed structures. Since most aluminum alloys have similar thermal conductivity, a high strength aluminum alloy will be desirable. 7075-T6 meets the high strength requirement with a desirable ductility. The material has been well studied for its material properties. The elasticity modulus of the material is 71.7 GPa and the Poisson's ratio is 0.34. A typical yield strength of 450 MPa was used for 7075-T6 in this study. The two structures under consideration are shown in Figs 3.3.26 and 3.3.27, respectively. The two structures have an

identical porosity of 64%. The channel structure has a channel dimension of 4mmx4mm. For the 3D lattice structure, each hollow chamber has a dimension of 4.472mmx4.472mmx4mm.

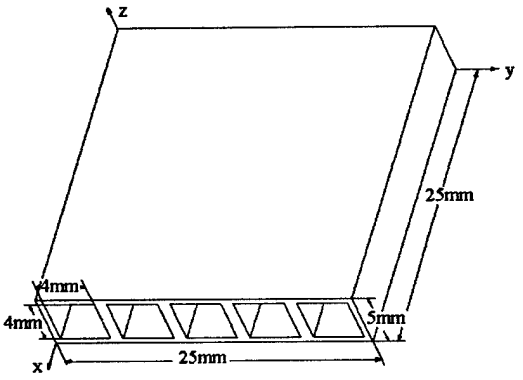

Fig. 3.3.26 Meso-channel structure

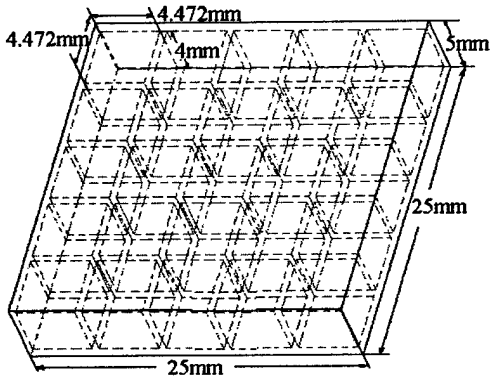

Fig. 3.3.27 3D lattice

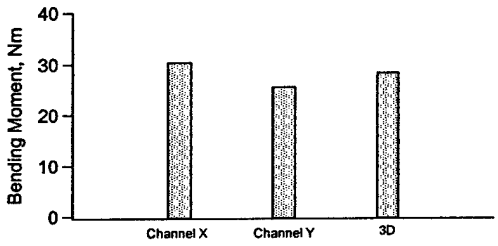

Fig. 3.3.28 Strength comparison of the two aluminum structures

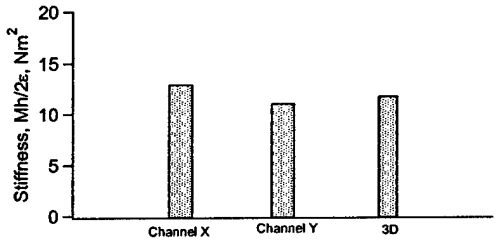

Fig. 3.3.29 Stiffness comparison of the two aluminum structures

The strength and stiffness of the two structures were evaluated by using the finite element method. The strength of the structure is measured by the maximum bending moment at which material yielding is to occur on the surface of the structure. The stiffness is the resistance of the structure against deformation. $Mh/2\varepsilon$ is used for the structural stiffness for a plate structure, where M is the applied bending moment, h is the height of the plate structure, and ε is the strain on the plate surface in the direction corresponding to the bending moment. The results are shown in Figs 3.3.28 and 3.3.29 for strength and stiffness, respectively. Channel x represents the case for the channel structure when the bending moment is applied on the x-cross section (yz plane), and Channel y in the figures denotes the case when the bending moment is applied on the xz plane. The channel structure has a maximum strength and stiffness when the bending moment is applied on the yz plane (Channel x) and the properties are the lowest when the bending moment is applied on the xz plane (Channel y). The mechanical properties of the 3D lattice structure are identical in both x and y directions. The strength and stiffness of the 3D lattice structure fall in

between those of Channel x and Channel y, with approximately 7% lower in strength and stiffness than that of Channel x.

3.4. Discussion

3.4.1. Comparison of Modeling Methods

In this work, two types of methods were used to characterize mechanical behavior of materials. They were the energy method and the finite element method. Both models were simplified by the homogenization theory in such a way that the composite materials were considered isotropic and the mechanical properties in the x and y material directions were considered uniform. The modeling of the sophisticate woven geometry of graphite/epoxy skin and copper screen was reduced to the modeling of a solid beam. Not only the size of the models was reduced significantly but also computation time was much less. The study shows that the simplified models are capable of predicting the performance of the materials.

The energy method was derived from the energy conservation law and was easy to implement. The main effort in the implementation of the method lies in programming. The size of the finite volumes of the structure was limited by the computer memory capacity. The smaller size of the finite volumes of the structure was, the more finite volumes were needed in the structure, and the more memory capacity of the computer was required. Compared with the finite element method, the energy method is easier to implement, the computation time is much less, and it does not need the support of high performance computers.

The finite element method was implemented with commercial software. A higher performance computer is required compared with the energy method. The finite element software provides graphic user interface for the user to build the model. Generally no programming was needed except those for post-processing. For nonlinear calculations, the finite element method takes significant computation time. Result files of the finite element method are much larger and more hard disk space is needed as compared with the energy method.

3.4.2. Multiscale Modeling Methodology

A broad range of scientific and engineering problems involve multiple scales. Traditional monoscale approaches have proven to be inadequate, even with the largest supercomputers, because of the range of scales and the prohibitively large number of variables involved. Therefore, there is a growing need to develop systematic modeling and simulation approaches for multiscale problems. The main idea of the multiscale modeling is to capture the large scale solutions of multiscale problems on a coarse mesh.

Multiscale modeling developed in this work simplifies the modeling of screen laminates composites. Two scales of models, a large scale model and a small scale model, were built for the modeling of screen laminate composites. The large scale of model is the modeling of the screen laminate based on the homogenization theory and the small scale of model is the modeling of a single layer copper screen based on the material properties of copper. The large scale model uses the results generated by the small scale model which is built with refined meshes.

The small scale model is a detailed model whose geometry is exactly the same as that of the woven copper screen. The model uses copper mechanical properties as input and outputs the basic mechanical properties of copper screen. If one wants to build a finite element model of the copper screen laminate in the small scale using the copper material properties, layers of sophisticated woven shaped copper screen need to be generated and stacked together to form the laminate. This laminate model may need 673,920 elements. 16,174,080 degrees of freedoms need to be calculated. Generally, a computer's computing ability required in a finite element simulation is the element number to the power of three. The performance of computer needed is so high that it is unrealistic to build such a model. With multiscale methodology, the modeling work is simplified. Since the copper screen material has regular and repetitive geometry, the homogenization theory is applied. Regardless the detail shape of the copper screen, the screen laminate could be treated as an isotropic material with the mechanical properties of the copper screen. The large scale model of screen laminate is built as a uniform and solid material having the mechanical properties of copper screen predicted by the small scale model – the single layer copper screen model. In this way, the size of the screen laminate model is reduced and the computational cost is lowered tremendously.

The modeling of the screen laminate is simplified by the homogenization theory. Tension and compression experiments of copper screens were conducted to obtain the basic mechanical properties of copper screen. With the multiscale methodology, the experiment for obtaining basic mechanical properties is not a necessity. The purpose of the small scale model is to provide the required information for the large scale model - the screen laminate model. The basic mechanical properties predicted by the single layer model could be used as the input by the screen laminate model to predict the performance of the copper screen laminate. The experiment work for copper screen could be saved.

3.5. Summary

Mechanical performance of the TES-systems was investigated experimentally and characterized with theoretical models. Experiments were conducted with graphitic TES composites, aluminum channel structures, screen laminate composites, as well as the materials used in the structures. Basic material properties were obtained by testing the materials under tension and compression loading. The structures were tested under bending. Fatigue experiments were conducted for graphitic TES composites at both room and high temperature. The graphite/epoxy skin displays elastic deformation before fracture. Failure occurs in the interface of the graphitic skins and the porous graphitic core. The porous graphitic core and the PCM fill have an insignificant influence on the strength and stiffness of the graphitic TES composites. Temperature greatly affects the fatigue strength of the graphitic TES composites. The copper screen material was found to display tension-compression asymmetry. The strength of the copper screen laminate composites is dependent on the orientation of the laminates. Failure is due to excessive plastic deformation of the material. The aluminum structures were found to possess excellent strength and stiffness. Failure of the aluminum structures is due to plastic deformation of the material.

An energy method was developed to predict the mechanical behavior of a structure under bending. The method was based on the energy conservation law and can be applied to structures as simple as screen laminates and to structures as complicated as 2D box structures. In addition, finite element models were developed to simulate the deformation and failure of the carbon/graphite TES composites and the screen laminate composites. Both the energy method and the finite element models can provide accurate deformation and failure predictions for the structures under investigation. The method is simple and practical for structures under bending loading. The finite element models are suitable for complex structures under the general loading conditions.

A multiscale methodology was developed for the modeling for the screen laminates. With the model of single layer copper screen, basic mechanical properties of copper screen can be predicted, and the predicted properties can be used as the input to the screen laminate model to simulate the performance of the screen laminates. With the multiscale methodology the sophisticate geometry of copper screen can be studied and the experimental work to obtain the mechanical properties of a single layer copper screen can be saved.

4. Phase Change Material Issues

4.1. Distributed Bellows Mechanism

As PCM has a 13% of volume expansion upon phase transition, micro balloons may be used to compensate the volume change. When subjected to external pressure, the wall of a micro balloon deflects. The deformation recovers upon the release of the external pressure. When the system is heated to the transition temperature of PCM, PCM expands, and the pressure in the system increases that makes the micro balloon collapse. When the system is cooled below the transition temperature of PCM, PCM goes back to its original volume, and the micro balloons may recover to its original shape. In this way, the total volume of the system could remain constant.

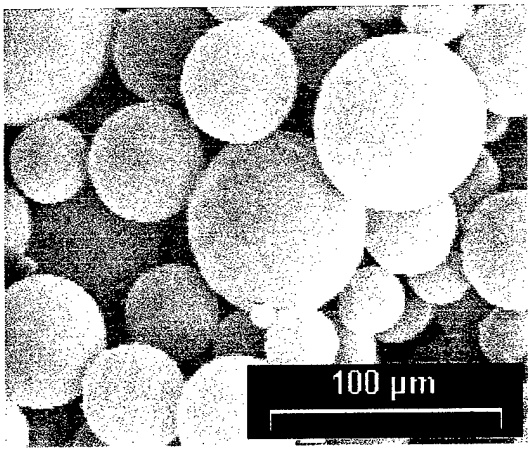

Figure 4.1.1 PM6550 micro balloons

The behavior of PM6550 micro balloons was studied. PM6550 micro balloons are manufactured by Potter Industries Inc. The size of the micro balloons varies in the range between 15 and 200 micron with an average size of 100 micron (Fig. 4.1.1). The mean thickness of the balloon shell is 5 micron. The density of micro balloons is 0.022g/cc.

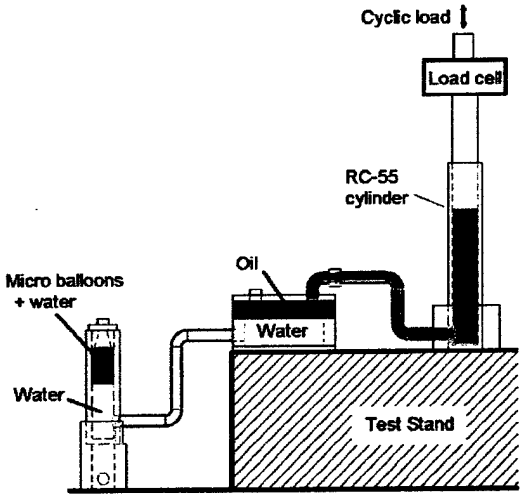

Fig. 4. 1.2 Experimental setup for testing

An apparatus was designed to experimentally determine the mechanical properties of the micro balloons at room temperature (Fig. 4.1.2). A bag of micro balloons is placed inside a cylinder which was connected to a pressurizing unit. A load is applied using the material testing frame on a pressurizing cylinder. Hydraulic oil is used for the pressurizing cylinder while water is used for the pressurized cylinder containing the micro balloons. A stainless steel chamber is placed in between the two cylinders to separate the water and oil. The pressure in the system is determined by measuring the load applied in the pressurizing cylinder.

In the experiments, cyclic load was applied to the system with an INSTRON testing machine. The load ratio (the minimum load versus maximum load in a loading cycle) was 0.1, and the

testing frequency was 0.1 Hz. Each experiment lasted 200 loading cycles. In the experiments, the maximum applied load, thus maximum pressure, in a loading cycle was controlled. The maximum pressure in the current study ranges from 10 to 50 atm.

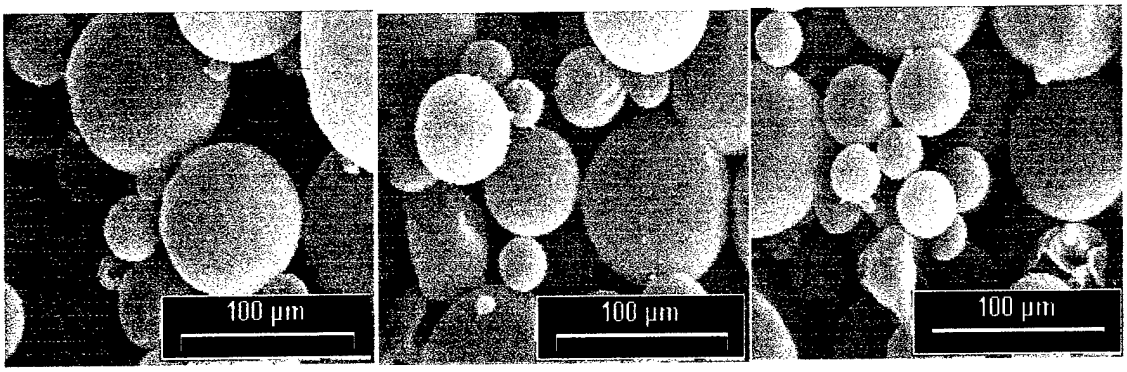

Maximum load: 10 atm Maximum load: 20 atm Maximum load: 30 atm

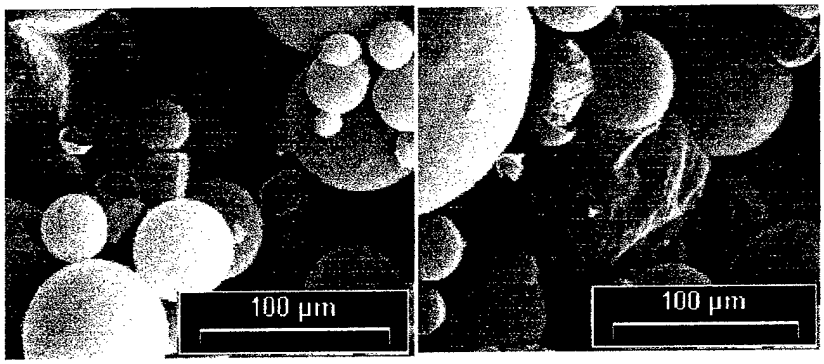

Maximum load: 40 atm Maximum load:50 atm

Fig. 4. 1.3 Micro balloons after 200 cycles of cyclic loading

Dependent on the maximum pressure applied, a certain percentage of the balloons were broken due to the cyclic loading. Photos were taken under a microscope after each experiment (Fig.4. 1.3). Unbroken and broken balloons were counted to come up with a relationship between the applied pressure and the percentage of the broken balloons. A higher pressure resulted in a higher percentage of broken micro balloons. Figure 4.1.4 summarizes a statistic of the broken balloons after the repeated pressurization for 200 times. For the balloons under investigation, 10% of the balloons break at a maximum pressure of 10 atm after 200 loading cycles. The rate goes up to 60% when the maximum pressure is 50 atm.

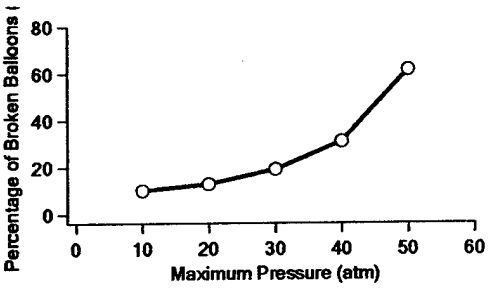

Fig. 4. 1.4 Damage statistics of micro balloons

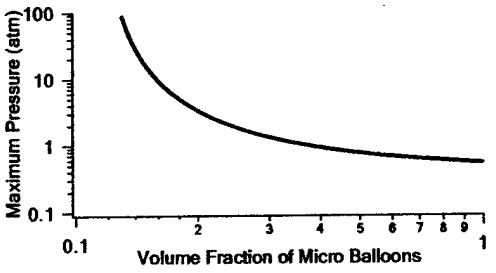

Fig. 4. 1.5 Relationship between pressure and volume fraction of micro balloons in the system

The compressibility of the micro balloon was found to be similar to that of air. Assuming no breakage of the balloons during operation, a relationship between the maximum pressure allowed in the TES system and the volume percentage of the micro balloons needed to compensate the 13% expansion can be obtained as shown in Fig.4. 1.5. If the maximum operational pressure is 20 atm (2MPa), the amount of micro balloons is 14.5% of the volume PCM.

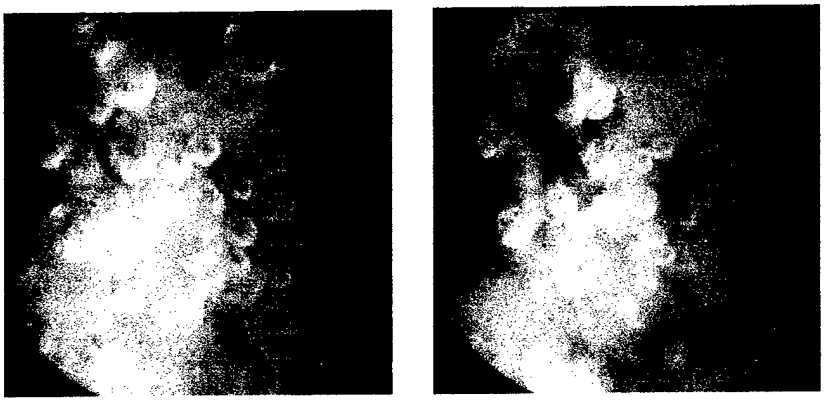

(a) Uncompressed (b) Compressed

Fig.4. 1.6 Compression of micro balloons

Figure 4.1.6a shows a microscopic image of micro-balloons in liquid paraffin (approx 70°C) at 1 atmosphere. The right hand image (Fig. 4.1.6b) shows the same collection of micro-balloons when they are compressed at approximately 17 atm. The volume change of the balloons is evident. It is interesting to observe that while most of the balloons appear to collapse uniformly, the walls of some balloons (candidates for failure?) buckle as they collapse.

Micro balloons may provide a practical means to compensate the expansion of the PCM due to phase transformation. Different types of micro balloons should be experimentally studied for their thermal and mechanical behavior. Performance at a temperature above the transition temperature of the PCM should also be explored. Finally, polymer micro-balloons have a specific gravity of approximately 0.2, which makes them quite buoyant in liquid paraffin in a 1g

environment. Lacking a suitable balloon immobilization mechanism, this would restrict this approach to zero-g environments

4.2. Liquid Paraffin Immobilization

Paraffins are immobilized using block copolymers for encapsulation of the high temperature liquid wax. Polymeric shape stabilized thermal storage materials are prepared using several polymers as matrix materials. SEBS, SEEPS and other polymers are investigated [Agari et al, 1993]. SEBS (polystyrene-ethylene-butylene-styrene, Kraton G1651, G1657 and G1726, Kraton Inc., Kraton Polymers) block copolymers contain a polystyrene block and hydrogenated polybutadiene block. Two different molecular weights of SEBS have been investigated.:

1. SEBS1651 is identified as high molecular weight SEBS (HMWSEBS). SEBS1657 is identified as low molecular weight SEBS (LMWSEBS).

2. SEEPS block copolymer (polystyrene-poly (ethylene/ethylene/isoprene)- polystyrene, Septon S4030, S4033 and S4044, Kuraray Co. Ltd) is a high performance thermoplastic rubber. SEEPS4044 is identified as high molecular weight SEEPS (HMWSEEPS). SEEPS4033 is identified as low molecular weight SEEPS (LMWSEEPS).

Compared with SEBS of the same molecular weight, SEEPS has better mechanical properties and superior heat resistance shown in Table 4.1. The chemical structures and molecular structures of SEBS and SEEPS are shown in Figure 4.2.1 and Figure 4.2.2:

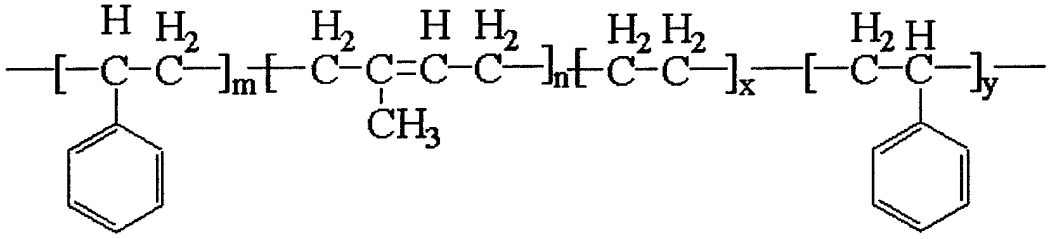

Fig. 4.2.1 Chemical structure of SEBS.

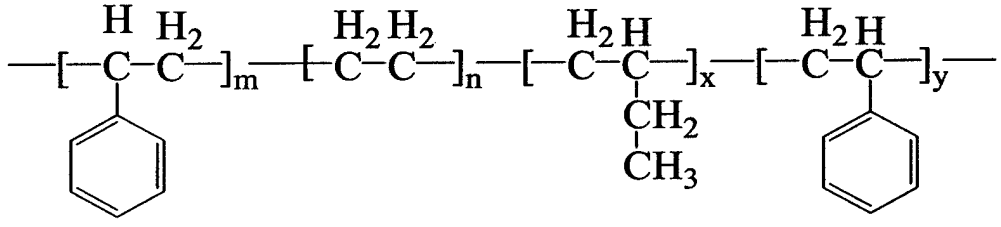

Fig.4.2.2 Chemical structure of SEEPS.

Table 4.2 Physical and chemical properties of SEBS and SEEPS.

Materials	SEBS (Kraton™)			SEEPS(Septon™)		
	G1651	G1657	G1726	S4030	S4033	S4044
Appearance	WP	DP	DP	WP	WP	WP
Polystyrene Content (%)	31.2-34.6	12.3-14.3	29.2-31.6	20	30	32
Tensile Strength (psi)	5500	3400	350	3930	5120	-
Hardness * Shore A	61	47	70	71	76	-
Elongation (%)	700	750	200	540	500	-
Specific Gravity (g/cc)	0.91	0.90	0.91	0.91	0.91	0.91
Solution Viscosity (mPa•S)	>50000**	1600**	140-220**	1.5***	<0.1***	No flow

WP: White Powder DP: Dust Powder

* Typical values on polymer compression molded at 300°F

** 25% wt toluene solution at 25°C. *** 10% wt toluene solution at 25°C

Table 4.3 List of polymer candidates for shape stable PCM.

Materials	Manufacturer	Chemical Structure	*Melt Point (°C)*	Specific Gravity	Appearance
a. Polyethylene naphthalate	Kaladex® Goodfellow	$-(C_2H_4)_m-(OCOC_{10}H_9)_n-$	> 160 °C	1.36	Crystalline pellets
b. Polyethylene terephthalate	Arnite® v Goodfellow	$-(C_2H_4)_m-(OCOC_6H_5)_n-$	> 170 °C	1.3	Crystalline pellets
c. Cyclic olefin copolymer	Topas® Ticona Inc.	$-(C_2H_4)_m-(CH-C_5H_8-CH)_n-$	> 180 °C	1.02	White granule
d. Ethylene vinyl silane copolymer	Aqua-link® Equistar Chemical, LP	$-(C_2H_4)_m-(C_2H_4SiH_3)_n-$	-	-	White powder
e. Ethylene/propylene copolymer	Peterolite ® Baker- Petrolite polymers	$-(C_2H_4)_m-(C_3H_6)_n-$	~95	~0.94	White solid

In addition to SEBS and SEEPS several other polymers were investigated for their ability to immobilize paraffin PCMs. Table 4.2 lists the polymers investigated. Among the polymer candidates, c) is a polymer which has been recently introduced commercially.

PCM-composites were prepared by melting 20% wt. of the co-polymer into stirred liquid paraffin (80% wt.) at 140°C. The process was performed under a nitrogen gas blanket. The polymer and paraffin are mixed for approximately 1hr until the solution reaches a very high viscosity. The mixture was then cast in a preheated Teflon mold, Thermocouples are placed at the center of the surface of the composite, and then the mold is allowed to cool. Some of the samples are subsequently dipped into a solution of toluene and copolymer to form a thin copolymer coating. The samples are prepared for thermal cycling by attaching the composite to an aluminum surface using conductive paste. A thermocouple is inserted between the sample and the aluminum plate.

Thermal cycling tests are performed on a thermal platform that cycles between 75°C and 35°C. Periodical observations are made and the test is concluded when there is visible evidence of distortion of the sample (sagging) or paraffin leakage from the sample. Gravimetric test are done in an oven that is maintained at 75°C. Samples are placed on an absorbent surface (a paper towel), and the samples are periodically weighed to determine mass loss.

Several copolymers listed in Table 4.2 and SEBS, SEEPS (Table 4.1) were tested for their compatibility with paraffin. Since paraffin contains only hydrogen and carbon, it is of low polarity. The chemical structure of the copolymers indicates that they contain polar and non-polar structure. The copolymers that contain portions of relatively low polarity are compatible with paraffin and able to dissolve the paraffin without phase separating. Copolymers that do not contain non-polar portions are not able to make shape stable PCMs. Results show that copolymer **a** and **b** in Table 4.2 cannot dissolve in the melted paraffin. The copolymers that completely dissolve in the melted paraffin are good candidates for shape stable composites. The initial gravimetric tests show that only a few of the copolymers form shape stable composites when they are exposed to 75°C overnight. The copolymers listed in Table 4.2 failed in the following order from highest to lowest immobilization: **c>e>d**. Among all of the copolymers SEBS and SEEPS demonstrated the best immobilization behavior, and these were subsequently subjected to further analysis.

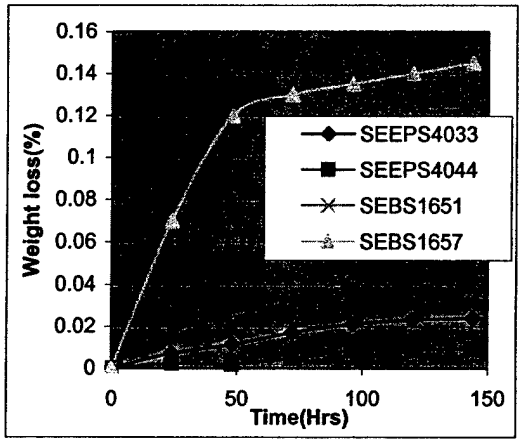

Fig. 4.2.3 Leakage rate of paraffin/polymer

Figure 4.2.3 shows the long term mass loss results of these copolymers, where the lowest molecular weight components exhibited the

greatest mass loss. Less than 0.01% weight loss is experienced by HMWSEEPS / paraffin The molecular weight of HMWSEBS is higher than LMWSEBS and the molecular weight of HMWSEEPS is higher than LMWSEEPS. For similar molecular weights, the leakage rate of the SEEPS/paraffin composite is much less than the SEBS/paraffin composite. Comparing the chemical structures of SEEPS and SEBS, the SEEPS contains isoprene which is more linear than the isobutylenes contained in SEBS. These linear segments appear to associate with the linear carbon chains of paraffin.

Surface characterization is done using optical microscopy and AFM. Samples of paraffin, SEEPS / paraffin, HMWSEBS / paraffin, pure paraffin and pure SEEPS are prepared by two methods. Each paraffin/copolymer composite consists of 80%wt paraffin and 20% wt paraffin.

The paraffin is distributed in the composite as particles of paraffin surrounded by copolymer. This phenomenon is confirmed by dissolving the SEEPS/paraffin composite in toluene. Since the SEEPS has high solubility in toluene and the paraffin has relative low solubility the paraffin will remain behind.

The optical microscope images show the surface structure of the polymer / paraffin PCM composites. Figure 4.2.4 shows the surface images of SEBS and SEEPS / PCM composites. These images show that the paraffin particles are encapsulated in the matrix of SEEPS or SEBS polymer structure. This is demonstrated by regions which exhibit variation in lightness / darkness of the images. The regions of darkness represent the depth variation of the surface. This indicates that the particle size of the SEBS composite is much larger than the SEEPS composite.

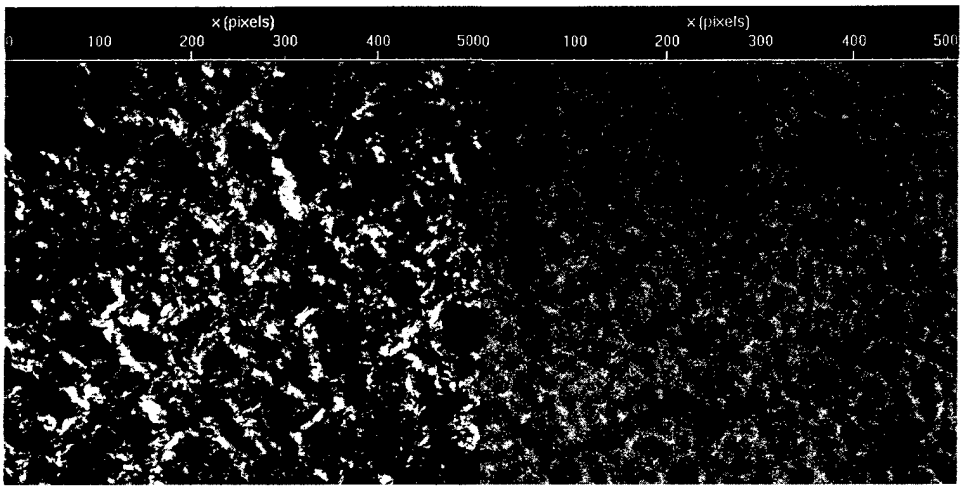

Fig. 4.2.4 Microscope image of Paraffin/SEBS and paraffin/SEEPS (method a)(X400).

It is important to understand whether the particle size and/or shape relates to the leakage behavior of the paraffin/copolymer composite. To investigate the microstructure of the composite surface it is necessary to use AFM. The top left images are 2-dimensional (2D) height images and the top right are 2-D phase images. The bottom images are 3D height and phase images, respectively.

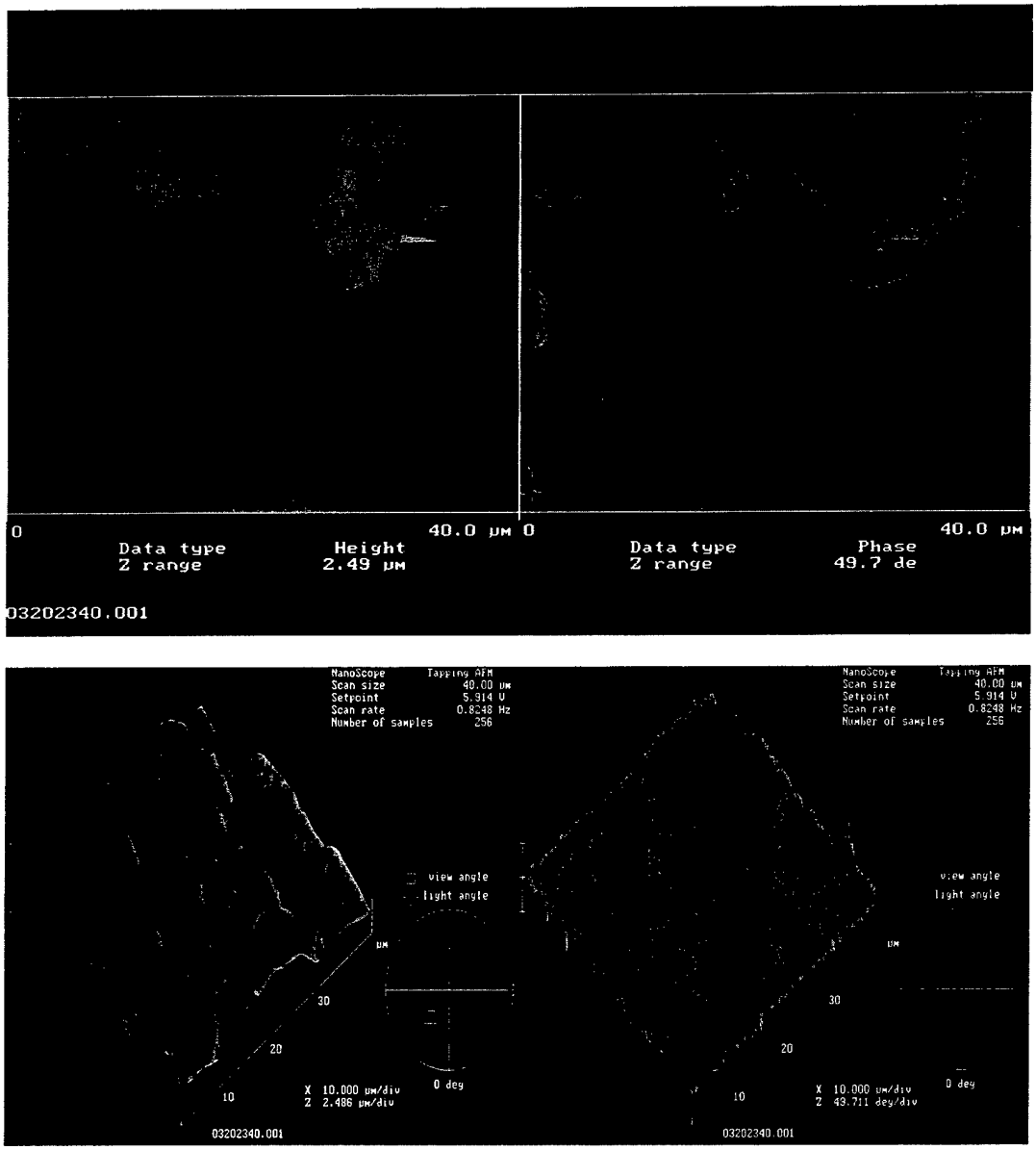

Fig. 4.2.5 Paraffin/SEEPS composite (method a).

Figure 4.2.5 shows AFM images of paraffin / SEEPS. The scan ranges are 40 *u*m. Small particles clearly protrude out of the matrix. The particle diameter appears to be ~5 *u*m.

An investigation of the SEBS/paraffin composite, using the same scan range as before, results in a structure which appears quite different. The particles are larger and appear to be more loosely

separated. For LMWSEBS/paraffin, the structure is poorly organized and there does not appear to be segregation of the paraffin from the SEBS.

It is useful to compare the structure of polymer / paraffin composites with pure paraffin and pure copolymer prepared using the same method. Figure 4.2.6 shows an optical microscopy image. There is no obvious particle/matrix structure at the pure paraffin and pure SEEPS surfaces.

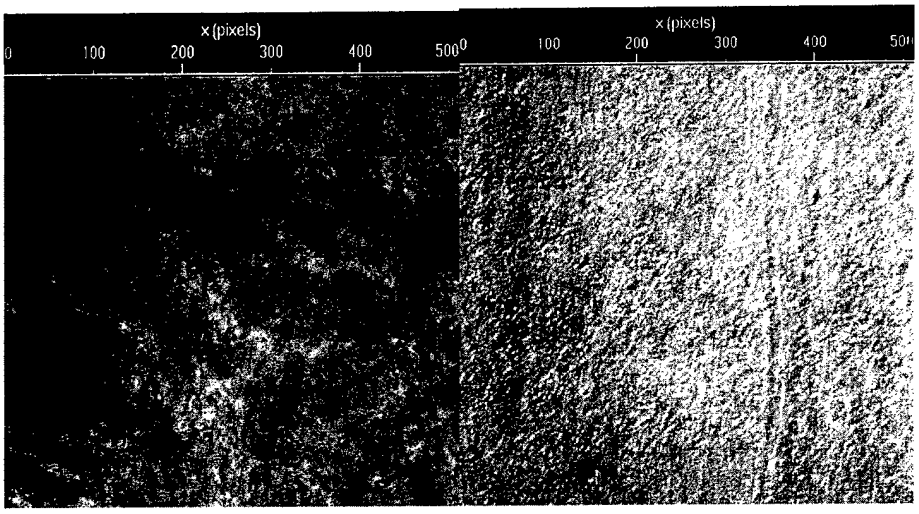

Fig. 4.2.6 Microscope image for pure paraffin and pure SEEPS (method a)(X400).

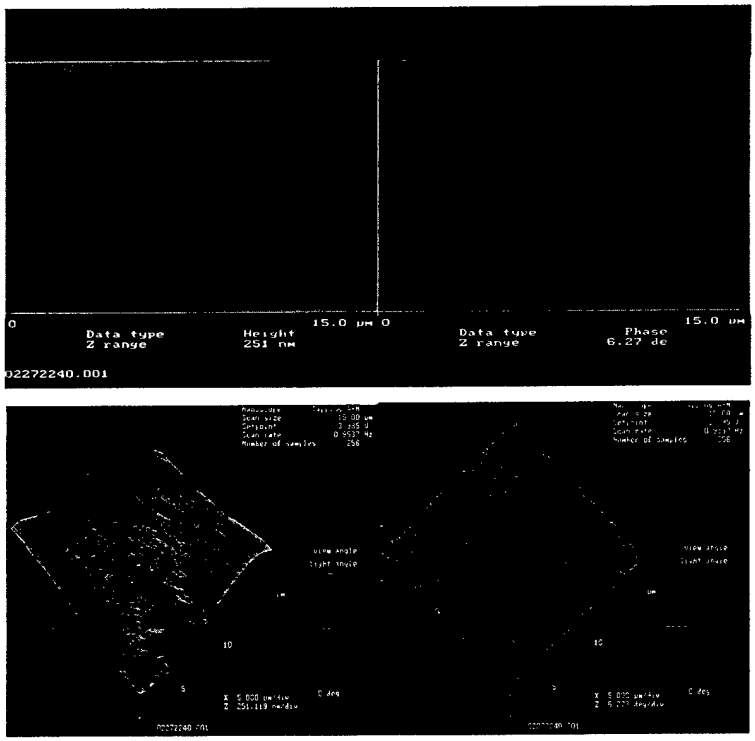

Fig. 4.2.7 AFM of pure paraffin (Method a).

Focusing on a small area of the surface, the 3D height image of pure paraffin looks like a mat, the surface is continuously smooth and no particle formation is observable. (Figure 4.2.7) This demonstrates that when paraffin is melted to form a film, it does not form the same structure as the paraffin/polymer composite.

Dissolving the polymer with organic solvent and later drying out the solvent, the polymer forms a thin film on the microscope slides. Figure 4.2.8 shows that a very smooth surface of polymer film is formed. This demonstrates that the polymer by itself does not exhibit phase segregation.

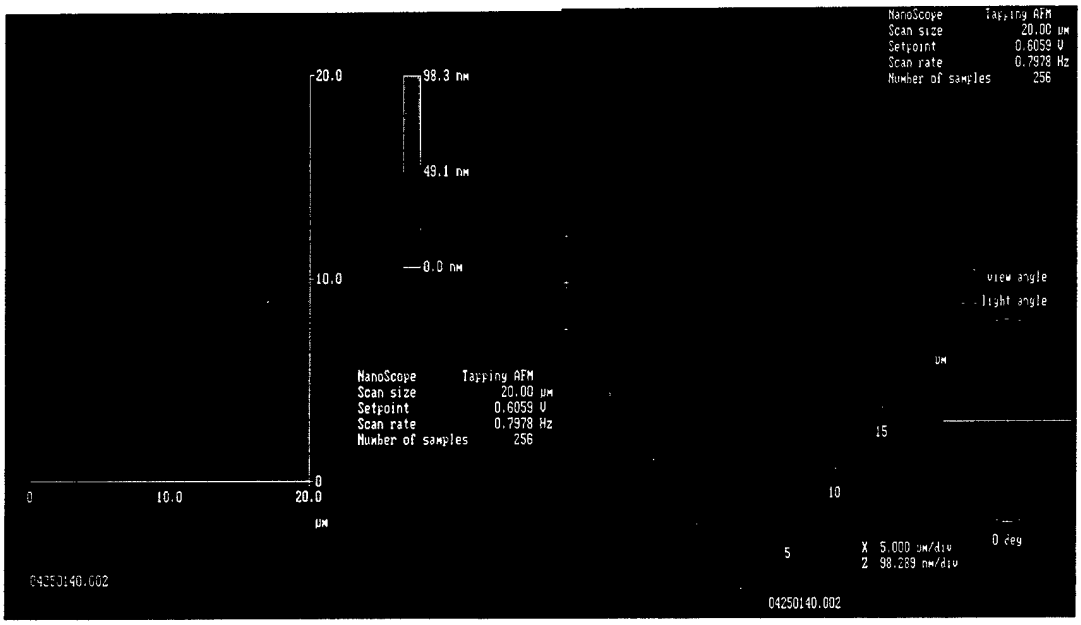

Fig. 4.2.11 Pure SEEPS-height (Method b).

AFM and optical microscopy show that paraffin particles are surrounded by a copolymer matrix and that the copolymer encapsulates the paraffin and immobilizes it. Figure 4.2.9 is a schematic of a possible mechanism for the paraffin immobilization. The paraffin is clustered around the linear chain part of the copolymer. The copolymer also contains the rigid polystyrene block. When the paraffin melts it is speculated that the polystyrene regions prevent the movement of the paraffin linear chain that is held with the copolymer ethylene chain. As a result, the paraffin is encapsulated in the matrix of copolymers and does not leak. Figure 4.2.12 and Figure 4.2.13 show the proposed mechanism of the possible chemical structure of paraffin/SEBS and paraffin/SEEPS. As proposed in Figure 4.2.9, the long chain of SEBS is likely to form a linear structure instead of clusters. Compared with the chemical structure of SEBS, the long chain of SEEPS is more likely to form clusters and these clusters enclose the paraffin linear chain

absorbed by the polyisoprene/ethylene regions. This phenomenon is confirmed by the imaging studies using optical microscopy and AFM.

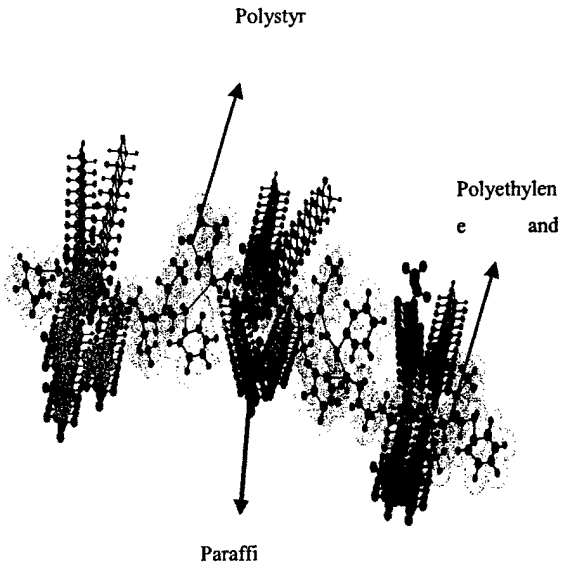

Fig. 4.2.9 Possible chemical structures of paraffin/SEBS composite.

As mentioned previously, the higher the molecular weight, the less leakage observed. This is because high molecular weight polymer has longer chains that form clusters and thus have better segregate the paraffin molecules. For the same weight ratio of paraffin/copolymer in the composite, high molecular weight copolymer will provide better immobilization of the liquid-solid PCMs.

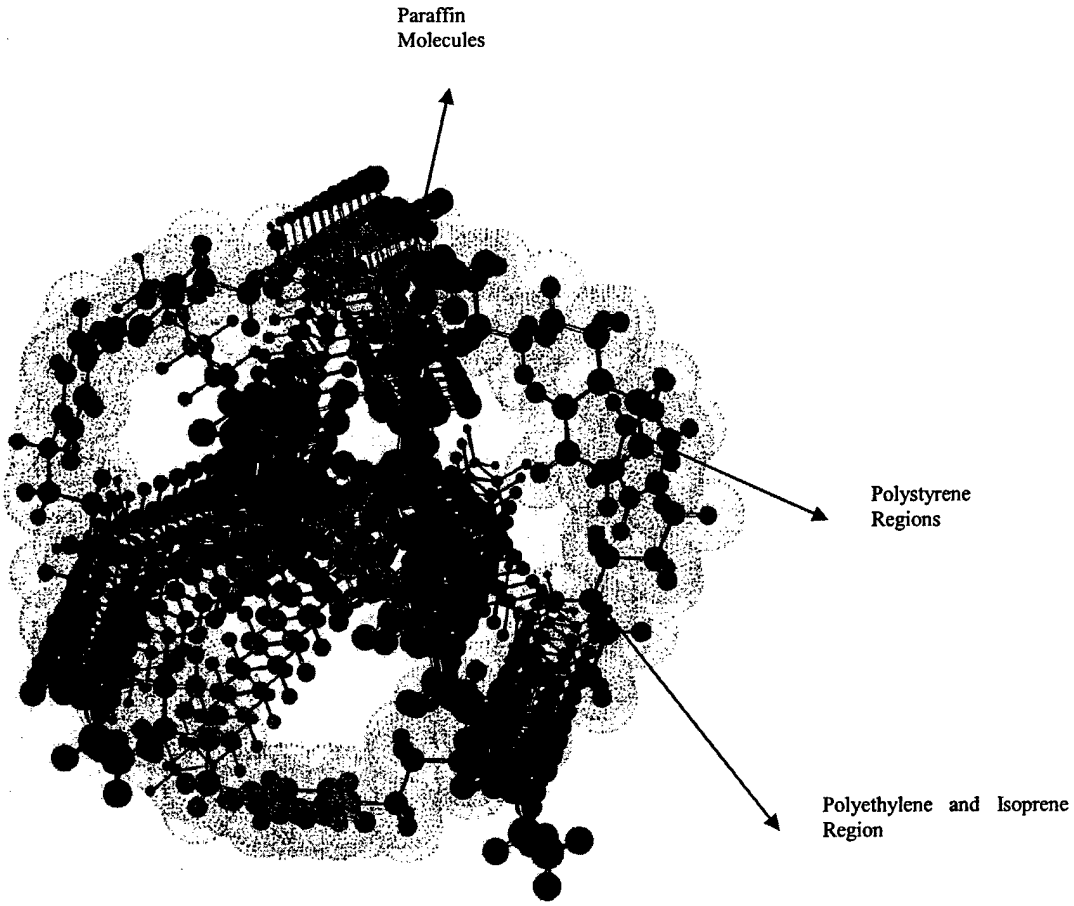

Fig. 4.2.13 Possible chemical structures of paraffin/SEEPS composite.

4.3. Aqueous Solution Formulation of PG/NPG Solid Solutions

The polyalcohol combination Pentaglycerine/ Neopentaglycol (PG/NPG) is an attractive PCM for electronics thermal control because: 1) It can be formulated to undergo solid-state phase transition over the 24°C - 85°C temperature interval, and 2) the latent heat is competitive with other popular PCM's. However, formulation of solid solutions has been a cumbersome operation involving the following steps [Chandra, 2000]:

1. mixing melted PG and NPG components (at temperatures above 140°C),followed by
2. chilling the solidified mixture to approximately 0°C with storage for 24 hours, followed by
3. grinding the material to a fine powder, followed by
4. stressing the powder in a laboratory press.

The final compressed material is a solid solution of the PG/NPG mixture. Since the material is volatile and flammable when at 140°C, this process is not only time consuming, but also somewhat hazardous.

As an alternative, we have proposed the following process:

1. Prepare appropriate fractions of PG and NPG
2. Dissolve these in water at 90°C
3. Dry the material in an oven at 90 °C

Figures 4.3.1 and 4.3.2 are Differential Scanning Calorimetry (DSC) results for pure PG and NPG, the first peak represents the solid-solid phase transition, and the second peak represents the solid-liquid (melting) phase transition of the materials. The solid-solid transition of PG and NPG are 88°C and 40°C, and the melting point of PG and NPG are 202°C and 130°C.

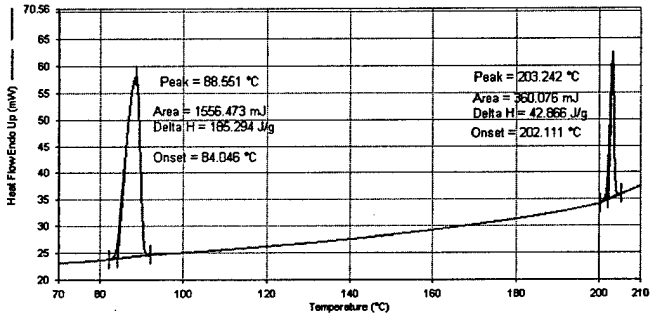

Fig. 4.3.1 DSC for pure PG

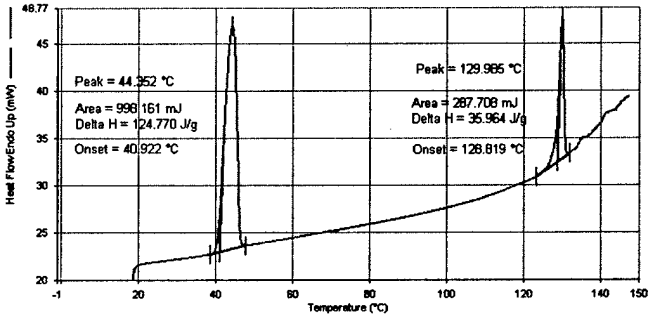

Fig. 4.3.2 DSC for pure NPG

Once PG and NPG form the solid solution, a new crystalline structure consisting of bimolecular chains of molecules with hydrogen bonds between every molecular are produced. The solid-solid phase transition of the new materials depends on the component ratio of the PG to NPG. Figures 4.3.3 and 4.3.4 show the DSC results of 70/30 mole ratio PG and NPG by two methods, the

melting method and the aqueous solution method. The phase transition temperatures are both at approximately 60°C and the measured latent heats (105 joule/gm) are within 5% of each other.

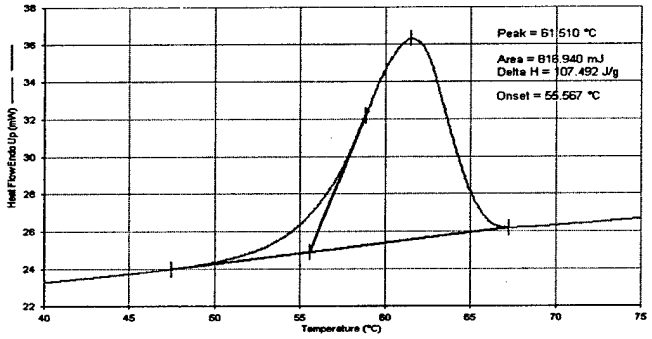

Fig. 4.3.3 DSC for PG/NPG solid solution (melting method)

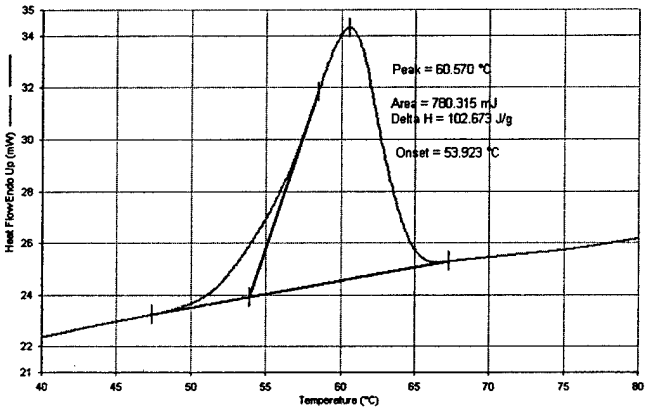

Fig. 4.3.4 DSC for PG/NPG solid solution (aqueous solution method)

4.4. Conclusions

Distributed Bellows Mechanism The feasibility of incorporating polymer micro-balloons in paraffin as a distributed bellows mechanism to address the volume expansion that accompanies phase transition is studied. Balloons are found to be adequately durable when exposed to cyclic pressure loading (200 cycles) that simulates expansion and contraction of a contained paraffin mass. Furthermore, pressure loading of approximately 17 atm is sufficient to accommodate phase transition associated expansion of paraffin. From a structural perspective, this is relatively minor loading condition. However, polymer micro-balloons have a specific gravity of approximately 0.2, which makes them quite buoyant in liquid paraffin in a 1g environment. Lacking a suitable balloon immobilization mechanism, this would restrict this approach to zero-g environments.

Paraffin Immobilization Immobilization of the liquid phase of solid-liquid PCM may be necessary so that TES-system thermal performance is g-load/orientation insensitive. Imbedding the PCM in a foam that has a small cell size (< 500 μm) will lead to short-time immobilization of

the liquid because the natural convection Rayleigh number is so small. In situations where the paraffin is contained in a meso-scale encapsulation, embedding paraffin in a suitable thermoplastic matrix could be a desirable design alternative. Gravimetric testing at elevated temperatures, coupled with thermal cyclic testing of a series of co-polymers shows that the co-polymer SEEPS is the most effective immobilizer.

Polyalcohol Solid Solution Formulation The polyalcohol combination Pentaglycerine/ Neopentaglycol (PG/NPG) is an attractive PCM for electronics thermal control because: 1) It can be formulated to undergo solid-state phase transition over the 24°C - 85°C temperature interval, and 2) the latent heat is competitive with other popular PCM's. However, formulation of solid solutions has been a cumbersome operation. DSC measurements confirm that forming an aqueous solution of the desired mole-fraction followed by drying results in acceptable solid solutions.

5. References

ASTM, 2001, "Standard Test Method for Tensile Properties of Polymer Matrix Composite Materials," ASTM D3039/D3039M-95a, American Society for Testing and Materials, Philadelphia, PA.

ASTM, 2001, "Standard Test Method for Tensile Strength of Sandwich Structures," ASTM C297-94, American Society for Testing and Materials, Philadelphia, PA.

ASTM, 2001, "Standard Test Method for Compressive Properties of Rigid Cellular Plastics," ASTM D1621-00, American Society for Testing and Materials, Philadelphia, PA.

ASTM, 2001, "Standard Test Method for Flexural Properties of Sandwich Constructions," ASTM C393-00, ASTM D3039/D3039M-95a, American Society for Testing and Materials, Philadelphia, PA.

Adams, D. F., November 1989, "Micromechanical Analysis of Composite Materials: Applications to Practical Problems," Technomic Publishing AG, Basel, Switzerland

ABAQUS, 2002, ABAQUS User's Manual, V 5.8, Hibbitt, Karlsson & Sorensen, Inc.

Altair Engineering, 2002, Hyper Works Help Documents, Altair Engineering, Inc.

ANSYS, 2002, ANSYS Electronic Help Documents, ANSYS, Inc.

Bauer, C.A. and Wirtz, R.A., Nov. 6, 2000, "Thermal Characteristics of a Compact, Passive Thermal Energy Storage Device", Paper 2-e-2-1, ASME International Mechanical Engineering Conference and Exposition, Orlando.

Beginn, 2003, " Applicability of Frozen Gels From Ultra High Molecular Weight Polyethylene and Paraffin Waxed as Shape Persistant Solid/Liquid Phase Change Materials," Macromol, Mater.Eng., Vol. 288, pp. 245-251.

Blended Waxes, Inc., 1512 South Main Street, P.O. Box 3044, Oshkosh, Wisconsin 54903, USA.

Brown, R.C., Rasberry, J.D., and Overmann, S.P., 1998, "Microencapsulated Phase-change Materials as Heat Transfer Media in Gas-fluidized Beds," Powder Technology, Vol. 98, pp. 217-222.

Buckley, 2001, "Flexible Composite Material with Phase Change Thermal Storage," US Patent 6183855.

Calmidi, V.V. and Mahajan, R.L. (1999) "The Effective Thermal Conductivity of High Porosity Fibrous Metal Foams", *J Heat Transfer*, Vol. 121, pp. 466 - 471

Chandra, D., Barrett, C.S., and Benson, D.K., 1989, " X-Ray Diffraction Studies of Solid Solutions of Pentaglycerine-Neopnetylglycol," Advanced in X-ray Analysis, Vol. 32, pp. 609-616.

Chandra, D., Chien, W., Gandikotta, V., and Lindle, D.W., 2002a, "Heat Capacities of " Plastic Crystal" Solid State Thermal Energy Storage Materials," Zeitschrift Fuer Physikalische Chemie, Vol. 216(12), pp. 1433-1444.

Chandra, D., Ding, W., and Lynch, R.A., 1991, "Phase Transitions in "Plastic Crystals," Journal of the Less-Common Metals, Vol. 168, pp. 159-167.

Chandra, D. and Lynch, R.A., 1990, "Phase Diagram Studies on Neopentylglycol and Pentaerythritol- Thermal Energy Storage Materials," Advances in X-Ray Analysis, Vol. 33, pp. 445-452,.

Chandra, D., Mandalia, H., Chien, W., Gandikotta, V., Lindle, D.W., and Rudman, R., 2002b, "Solid-solid Phase Transition in Trimethylolpropane (TRMP)," Zeitschrift Fuer Physikalische Chemie, Vol. 216(12), pp. 1389-1400.

Chandra, D. (1999) Personal Communication, Makay School of Mines, University of Nevada, Reno, Nv, 89557

Fosset, A.J., Maguire, M.T., Kudirka, A.A., Mills, F.E., and Brown, D.A., 1998, "Avionics Passive Cooling with Microencapsulated Phase Change Materials," Journal of Electronic Packaging, Transactions of ASME, Vol. 120(3), pp. 238-242.

Frohlich, et al, 2000, "Food Warning Device Containing a Rechargeable Phase Change Material," US Patent 6108489.

Ganesh, V. K. and Naik, N. K., 1996, "Failure Behavior of Plain Weave Fabric Laminates under on-axis Uniaxial Tensile Loading: I – Laminate Geometry," Journal of Composite Materials, Vol. 30, pp. 1748-1778.

Graies, D. and Faber, K.T., "The Thermal Properties of Pitch-Derived Graphite Foam," Carbon, Vol. 40(7), pp. 1137-1140.

Greiner, M., Fischer, P.F., Tufo, H., and Wirtz, R.A., 2002, "Three-Dimensional Simulations of Enhanced Heat Transfer in a Flat Passage Downstream from a Grooved Channel," ASME J. Heat Transfrer, Vol. 124, pp. 169 – 176.

Hatfield, 1987, "Encapsulation of Phase Change Materials," US Patent 4708812

Hawlader, M.N.A., Uddin., M.S., and Khin, M.M. , 2003, " Microencapsulated PCM Thermal-Energy Storage System," Applied Energy, Vol. 74, pp. 195-202.

Hayes, L.J., Spieker, M.A., Wissler, E.H., and Colvin, D.P., 1999, "A Simplified Model for Encapsulated Phase Change Material," HTD (ASME), Vol. 363(7), pp. 163-166.

Hexcel Corporation, F155TM Product Data of Hexcel Composites Corporation, Hexcel Composites Carbon Fibers, UT 6400 West 5400 South Salt Lake City, UT84118, USA.

Hong, Y. and Xin-shi, G., 2000, "Preparation of Polyethylene-Paraffin Compound as a Form-stable Solid-Solid Phase Change Material," Solar Energy Materials & Solar Cells, Vol. 64, pp. 37-44.

Howard Wire cloth Co., 28976 Hopkins Street, Hayward, California 94545, USA

Hübsh, P.F., Middleton, J., and Knox, J., 2000, "Computation of the Elastic Properties of a Resin Impregnated Wire Mesh by the Means of a Homogenization Procedure," Medical Engineering Physics, Vol. 22, pp. 521-524

Hydro Alunova Inc., Aavedvej 7, 6240 Logumkloster, Denmark, Tel: + 45 73 74 59 00

Inaba, H. and Tu, P., 1997, "Evaluation of Thermophysical Characteristics on Shape-Stabilized Paraffin as a Solid-Solid Phase Change Materials," Heat and Mass Transfer, Vol. 32, pp. 307-312.

Ishikawa, T. and Chou, T. W., 1982, "Elastic Behavior of Woven Hybrid Composites," Journal of Composite Materials", Vol. 16, pp. 2-19

Iwamato, Y. and Ikai, S., "New Polymeric Material for Latent Heat Thermal Energy Storage," lab report, Polymer Research Labortory, Ube Industries, Ltd. Japan.

Jiang, Y., Ding, E., Li, G., 2000a, "Contrast studies on Phase Change Materials of PEG/CDA Prepared by Chemical Reaction or Blendings-Relationship between Heat Storage Properties and Structures," Xianweisu Kexue Yu Jishu, Vol. 8(1), pp. 17-25.

Jiang, Y., Ding, E., and Li, G., 2000b, "Reticular Solid-solid Phase Change Materials and Their Manufacture," Faming Zhuanli Shenqing Gongkai Shuomingshu, pp. 7.

Jiang, Y., Ding, E., and Li, G., 2002, "Study on Transition Characteristics of PEG/CDA Solid-Solid Phase Change Materials," Polymer Vol. 43, pp. 117-122.

Kawabata, 1998, "Textile Structural Composites," Composite Materials Series, Vol. 3, pp. 73-84

Klett, J.,1998, "High Thermal Conductivity, Mesophase Pitch-Derived Carbon Foam," International SAMPE Symposium and Exhibition (Materials and Process Affordability-keys to the future, Book 1), Vol. 43, pp. 745-755.

Klett, J., Hardy, R., Romine, E.,Walls, C., and Burchell, T. , 2000a, "High-thermal-conductivity, Mesophase-pitch-derived Carbon Foams: Effect of Precursor on Structure and Porperties," Cabon, Vol. 38, pp. 953-973.

Klett, J., Klett, L., Burchell, T., and Walls, C., 2000b, " Graphite Foam Thermal Management Materials for Electronic Packaging', Lab report, Oak Ridge National Laboratory.

Klett, J. , 2000c, Lab report for Sample A3-3 SEM images, Oak Ridge National Laboratory.

Klett, et al, 2000d, "Gelcasting Polymeric Precursors for Producing Net-shaped Graphites," US Patent 6491891.

Klett, et al, 2000e, "Pitch-based Carbon Foam Heat Sink with Phase Change Materials," US Patent 6037032.

Klett, J. and Conway, B., 2000f, "Thermal Management of Solutions Utilizing High Thermal Conductivity Graphite Foams," International SAMPE Symposium and Exhibition, Vol. 45(2), pp. 1933-1943.

Klett, J., 2002a, "Method for Extruding Pitch Based Foam," US Patent 6344159.

Klett, J., 2002b, "Pitch-based Carbon Foam and Composites," US Patent 6387343.

Klett, et al, 2002c, "Pitch-based Carbon Foam Heat Sink with Phase Change Materials," US Patent 6399149.

Lu, T.J., Stone, H.A., and Ashby, M.F., 1998, "Heat Transfer in Open-cell Metal Foams," Acta Mater., Vol. 46(10), pp. 3619-3655.

Mills, A.F. (1999) Heat Transfer, 2nd ed, Prentice Hall.

McManus, H.L., Dunn, C.T., and Socha, M., 1996, "Design and Construction of a One-Piece Multifunctional Small Satellite Bus Structure," Tenth Annual AIAA/USU Small Satellite Conference, Logan, UT

Momose, et al, 1998, "Heat Transfer Composition," US Patent 5718835.

Mulligan, J.C., Colvin, D.P., and Bryant, Y.G., 1996, "Microencapsulated Phase-Change Materials Suspensions for Heat Transfer in Spacecraft Thermal Systems," Journal of Spacecraft and Rockets, Vol. 33(2), pp. 278-284.

Naik, N. K. and Ganesh, V. K., 1996, "Failure Behavior of Plain Weave Fabric Laminates under on-axis Uniaxial Tensile Loading: II – Analytical Predictions," Journal of Composite Materials, Vol. 30, pp. 1779-1822.

Noor, A. K., Venneri, S. L., Paul, D. B., and Hopkins, M. A., 2000, "Structures Technology for Future Aerospace Systems," Computers and Structures, Vol. 74, pp. 507-519.

Oliveira, I., Prud'homme, C., Veroy, K., and Patera, A. T., 2002, "Thermo-structural Analysis of Multifunctional Prismatic Cellular (Triangular) Metals," Online SimTeX Documents of A.T. Patera Research Group of MIT.

Park, J., Ruch, D., and Wirtz, R.A., 2002, "Thermal/Fluid Characteristics Of Isotropic Plain-Weave Screen Laminates As Heat Exchanger Surfaces," AIAA paper 2002-0208, AIAA Aerospcae Sciences Meeting, Reno, January 2002.

Poco Graphite, Inc., 300 Old Greenwood RdDecatur, Texas 76234, USA

Py, R., Olives, S., and Mauran, A., 2001, "Paraffin/Porous-graphite-matrix Composite As a High and Constant Power Thermal Storage Material," International Journal of Heat and Mass Transfer, Vol. 44, pp. 2727-2737.

Rachedi, R., S., and Chikh, S., 2001, "Enhancement of Electronic Cooling by Insertion of Foam Materials," Heat and Mass Transfer, Vol. 3, pp. 371-378.

Renton, W. J., Aerospace and Structures, 2001, "Where are Ee Headed?" International Journal of Solids and Structures, Vol. 38, pp. 3309-3319.

Sayler, et al, 1992, "Dry Powder Mixes Comprising Phase Change Materials," US Patent 5106520.

Sayler, et al, 1996, "Thermoplastic, Moldable, Non-exuding Phase Change Materials," US Patent 5565132.

Salyer, et al , 2000, "Article for Thermal Energy Storage," US Patent 6079404.

Thermalex Inc., 2758 Gunter Park Dr. West Montgomery, AL 36109, Tel : (334) 272 8270

Vandeurzen, P., Ivens, J. and Verpoest, I., 1995, "Structure-performance Analysis of Two-dimensional Woven Fabric Composites," In The Tenth International Conference on Composite Materials, Whistler, British Columbia, Canada, Vol. IV, pp.261-268.

Wang, X., Lu, E., Lin, W., Liu, T., Shi, Z., Tang, R., and Wang, C., 2000a, " Heat Storage Performance of the Binary Systems Neopentyl Glycol/Pentaerythritol and Neopentyl Glycol/Trihydroxy, Methyl-aminomethane As Solid-Solid Phase Change Materials," Energy Conversion & Management, Vol. 41, pp. 129-134.

Wang, X., Lu, E., Lin, W., and Wang, C., 2000b, "Micromechanism of Heat Storage In a Binary System of Two Kinds of polyalcohols as a Solid-solid Phase Change Material," Energy Conversion & Management, Vol. 41, pp. 135-144.

Wirtz, R. A., Fuchs, A., Narla, V., Shen, Y., Zhao, T., and Y. Jiang, 2003, "A Multi-Functional Graphite/Epoxy-Based Thermal Energy Storage Composite For Temperature Control Of Sensors And Electronics, " Paper AIAA-2002-0513, AIAA Aerospace Sciences Meeting, Reno, 2003.

Wirtz, R., Fuchs, A., and Jiang, Y., 2001, "Multifunctional Materials for Thermal Control of Sensors and Electronics," DOD Annually Report.

Wirtz, R.A., Li, C., Park, J., and Xu, J., 2002a "High Performance Woven Mesh Heat Exchangers," Eleventh AIAA/MDA Technology Conference and Exhibit, Monterey CA, July 29–Aug 2, 2002.

Wirtz, R.A., Peng, S., and Fuchs, A., 2003, "A Polymer-Based Thermal Energy Storage Composite For Temperature Control of Sensors and Electronics", Paper TED-AJ03-359, 6-th ASME-JSME Thermal Engineering Joint Conference, Hawaii, March 16 - 20, 2003.

Wirtz, R. A., Xu, J., Park, J., and Ruch, D., 2002b, "Thermal/Fluid Characteristics Of 3_D Woven Mesh Structures As Heat Exchanger Surfaces," paper no. 1372, Itherm 2002, San Diego, May 2002; also IEEE Trans. Components and Packaging Technology, 2003, Vol. 26, pp. 40–47.

Wirtz, R.A., Zheng, N., and Chandra, D., 1999, "Thermal Management Using Dry Phase Change Materials," Proceedings IEEE Semiconductor Thermal Measurement and Management Symposium, pp. 74-82

Xiao, M, Feng, B., and Gong, K. , 2001, "Thermal Performance of a High Conductive Shape-Stabilized Thermal Storage Material," Solar Energy Materials &Solar Cells, Vol. 69, pp. 293-296.

Xiao, M., Feng, B., and Gong, K., 2002, "Preparation and Performance of Shape Stabilized Phase Change Thermal Storage Materials with High Thermal Conductivity," Energy Conversion and Management, Vol. 43, pp. 103-108

Xu, J. and Wirtz, R.A., 2002, "In-Plane Effective Thermal Conductivity Of Plane-Weave Screen Laminates," Proc. Thermes 2002, pp. 231–242, Millpress, Rotterdam, also IEEE Trans, Components and Packaging Technology, Vol. 25, pp. 615–620.

Yamaguchi, 2001, "Heat Sink," US Patent 6212073.

Yang, J. M., Ma, C. L. and Chou, T.W., 1986, "Fiber Inclination Model of Three-dimensional Textile Structural Composites," Journal of Composite Materials, Vol. 20, pp. 472-483.

Zhang, Y.C. and Harding, J., 1990, "A Numerical Micromechanics Analysis of the Mechanical Properties of a Plain Weave Composite," Computer and Structures, Vol. 36, pp. 839-844

Zheng, N. and Wirtz, R.A., 2000, "Methodology for Designing a Hybrid Thermal Energy Storage Heat Sink," Paper 2-16-2-10, ASME International Mechanical Engineering Conference and Exposition, Orlando, Nov. 6, 2000.

Zheng, N., and Wirtz, R.A., 2001 , "Figures of Merit for Hybrid Thermal Energy Storage Units," Paper T3-20027, Proc. ASME National Heat Transfer Conference, Anaheim, June 10 - 13, 2001.

Zheng, N., and Wirtz, R.A., 2002, "Cylindrical Pin-Fin Fan-Sink Heat Transfer and Pressure Drop Correlations", IEEE Trans. On Components & Packaging Technology, Vol. 25, pp. 15 – 22.

Zuckerman, J.L., et al, 2001, " Fabric Coating Containing Energy Absorbing Phase Change Material and Method of Manufacturing same," US Patent 20010000517.

6. Ancillary Information

6.1. Research Personnel

R.A. Wirtz (Principal Investigator), Alan Fuchs (Co-PI) and Yanyao Jiang (Co-PI) Students: Yuyi Shen (MS), Venkat Narla (MS), Tianwen Zhao (MS).

6.2. Publications/ Theses

Publications

Wirtz, R.A, A. Fuchs, V. Narla, Y. Shen, T. Zhao and Y. Jiang, "A Multi-Functional Graphite/Epoxy-Based Thermal Energy Storage Composite For Temperature Control Of Sensors And Electronics," paper # 2002-0513, AIAA Aerospace Sciences Meeting, Reno, January 2003.

Wirtz, R.A, "Conformable Heat Storage Device", patent disclosure to Univ. Nevada, Reno, June 22, 2001

Thesis

Narla, V. (2003) "Multifunctional Materials for thermal Control of Sensors and Electronics: Thermal Characterization", MS Thesis, Mechanical Engineering Department, University of Nevada, Reno, NV 89557

Shen, Y. (2003) "Multifunctional Materials for thermal Control of Sensors and Electronics: Materials Characterization", MS Thesis, Chemical and Metallorigical Engineering, University of Nevada, Reno, NV 89557

Zhao, T. (2003) "Mechanical Characterization of Multifunctional Composites" MS Thesis, Mechanical Engineering Department, University of Nevada, Reno, NV 89557

Papers Pending

Narla, V, R. Wirtz, Y. Shen, A. Fuchs, T. Zhao and Y. Jiang, "Non-Metallic And Structurally Efficient Thermal Energy Storage Composites For Avionics Temperature Control, Part I: Thermal Characterization", AIAA Thermsciences meeting, Reno, NV January 2004.

T. Zhao, Y. Jiang, Y. Shen, A. Fuchs, V. Narla, and R. Wirtz, "Non-Metallic And Structurally Efficient Thermal Energy Storage Composites For Avionics Temperature Control, Part II: Structural Characterization", AIAA Thermsciences meeting, Reno, NV January 2004.

6.3. Acknowledgement/Dissclaimer

The Missile Defense Agency through the Air Force Office of Scientific Research, USAF, sponsors this work under contract number F49620-00-1-305. The views and conclusions contained herein are those of the authors and should not be interpreted as necessarily representing the official policies or endorsements, either expressed or implied, of the Missile Defense Agency, the Air Force Office of Scientific Research, or the U.S. Government